

Core-Shell Nanostructures: Modeling, Fabrication, Properties, and Applications

Guest Editors: Weihong Qi, Linbao Luo, Hai-Sheng Qian,
Gang Ouyang, Karuna Kar Nanda, and Sherine O. Obare





Core-Shell Nanostructures: Modeling, Fabrication, Properties, and Applications

Core-Shell Nanostructures: Modeling, Fabrication, Properties, and Applications

Guest Editors: Weihong Qi, Linbao Luo, Hai-Sheng Qian,
Gang Ouyang, Karuna Kar Nanda, and Sherine O. Obare



Copyright © 2012 Hindawi Publishing Corporation. All rights reserved.

This is a special issue published in "Journal of Nanomaterials." All articles are open access articles distributed under the Creative Commons Attribution License, which permits unrestricted use, distribution, and reproduction in any medium, provided the original work is properly cited.

Editorial Board

Katerina Aifantis, Greece
Nageh K. Allam, USA
Margarida Amaral, Portugal
Xuedong Bai, China
L. Balan, France
Enrico Bergamaschi, Italy
Theodorian Borca-Tasciuc, USA
C. Jeffrey Brinker, USA
Christian Brosseau, France
Xuebo Cao, China
Shafiul Chowdhury, USA
Kwang-Leong Choy, UK
Cui ChunXiang, China
Miguel A. Correa-Duarte, Spain
Shadi A. Dayeh, USA
Ali Eftekhari, USA
Claude Estournes, France
Alan Fuchs, USA
Lian Gao, China
Russell E. Gorga, USA
Hongchen Chen Gu, China
Mustafa O. Guler, Turkey
John Zhanhu Guo, USA
Smrati Gupta, Germany
Michael Harris, USA
Zhongkui Hong, USA
Michael Z. Hu, USA
David Hui, USA
Y.-K. Jeong, Republic of Korea
Sheng-Rui Jian, Taiwan
Wanqin Jin, China
Rakesh K. Joshi, India
Zhenhui Kang, China

Fathallah Karimzadeh, Iran
Do Kyung Kim, Republic of Korea
Kin Tak Lau, Australia
Burtrand Lee, USA
Benxia Li, China
Jun Li, Singapore
Shijun Liao, China
Gong Ru Lin, Taiwan
J.-Y. Liu, USA
Jun Liu, USA
Tianxi Liu, China
Songwei Lu, USA
Daniel Lu, China
Jue Lu, USA
Ed Ma, USA
Gaurav Mago, USA
Santanu K. Maiti, Israel
Sanjay R. Mathur, Germany
A. McCormick, USA
Vikas Mittal, UAE
Weihai Ni, Germany
Sherine Obare, USA
Edward Andrew Payzant, USA
Kui-Qing Peng, China
Anukorn Phuruangrat, Thailand
Ugur Serincan, Turkey
Huaiyu Shao, Japan
Donglu Shi, USA
Suprakas Sinha Ray, South Africa
Vladimir Sivakov, Germany
Marinella Striccoli, Italy
Bohua Sun, South Africa
Saikat Talapatra, USA

Nairong Tao, China
Titipun Thongtem, Thailand
Somchai Thongtem, Thailand
Valeri P. Tolstoy, Russia
Tsung-Yen Tsai, Taiwan
Takuya Tsuzuki, Australia
Raquel Verdejo, Spain
Mat U. Wahit, Malaysia
Shiren Wang, USA
Yong Wang, USA
Ruibing Wang, Canada
Cheng Wang, China
Zhenbo Wang, China
Jinquan Wei, China
Ching Ping Wong, USA
Xingcai Wu, China
Guodong Xia, Hong Kong
Zhi Li Xiao, USA
Ping Xiao, UK
Shuangxi Xing, China
Yangchuan Xing, USA
N. Xu, China
Doron Yadlovker, Israel
Ying-Kui Yang, China
Khaled Youssef, USA
Kui Yu, Canada
William W. Yu, USA
Haibo Zeng, China
Tianyou Zhai, Japan
Renyun Zhang, Sweden
Yanbao Zhao, China
Lianxi Zheng, Singapore
Chunyi Zhi, Japan

Contents

Core-Shell Nanostructures: Modeling, Fabrication, Properties, and Applications, Weihong Qi, Linbao Luo, Hai-Sheng Qian, Gang Ouyang, Karuna Kar Nanda, and Sherine O. Obare
Volume 2012, Article ID 526923, 2 pages

Preparation, Properties, and Self-Assembly Behavior of PTFE-Based Core-Shell Nanospheres, Katia Sparnacci, Diego Antonioli, Simone Deregibus, Michele Laus, Giampaolo Zuccheri, Luca Boarino, Natascia De Leo, and Davide Comoretto
Volume 2012, Article ID 980541, 15 pages

Preparation of a Novel Nanocomposite of Polyaniline Core Decorated with Anatase-TiO₂ Nanoparticles in Ionic Liquid/Water Microemulsion, Yanni Guo, Deliang He, Sanbao Xia, Xin Xie, Xiang Gao, and Quan Zhang
Volume 2012, Article ID 202794, 7 pages

Core-Shell Structure of a Silicon Nanorod/Carbon Nanotube Field Emission Cathode, Bohr-Ran Huang, Ying-Kan Yang, Tzu-Ching Lin, and Wen-Luh Yang
Volume 2012, Article ID 369763, 6 pages

Freestanding Ge/GeO₂ Core-Shell Nanocrystals with Varying Sizes and Shell Thicknesses: Microstructure and Photoluminescence Studies, P. K. Giri and Soumen Dhara
Volume 2012, Article ID 905178, 5 pages

Synchrotron X-Ray Absorption Spectroscopy Study of Self-Assembled Nanoparticles Synthesized from Fe(acac)₃ and Pt(acac)₂, K. Chokprasombat, C. Sirisathitkul, P. Harding, S. Chandarak, and R. Yimnirun
Volume 2012, Article ID 758429, 4 pages

In Situ Synthesis of Poly(methyl methacrylate)/SiO₂ Hybrid Nanocomposites via “Grafting Onto” Strategy Based on UV Irradiation in the Presence of Iron Aqueous Solution, Hong Zhang, Chao Li, Jinshan Guo, Limin Zang, and Jiahe Luo
Volume 2012, Article ID 217412, 9 pages

Reinforcement of Natural Rubber with Core-Shell Structure Silica-Poly(Methyl Methacrylate) Nanoparticles, Qinghuang Wang, Yongyue Luo, Chunfang Feng, Zhifeng Yi, Quanfang Qiu, L. X. Kong, and Zheng Peng
Volume 2012, Article ID 782986, 9 pages

Improvement in Comprehensive Properties of Poly(Methyl Methacrylate)-Based Gel Polymer Electrolyte by a Core-Shell Poly(Methyl Methacrylate)-Grafted Ordered Mesoporous Silica, Lixin Xu, Feng Xu, Feng Chen, Jintao Yang, and Mingqiang Zhong
Volume 2012, Article ID 457967, 10 pages

Comparative Study of the Photocatalytic Activity of Semiconductor Nanostructures and Their Hybrid Metal Nanocomposites on the Photodegradation of Malathion, Dina Mamdouh Fouad and Mona Bakr Mohamed
Volume 2012, Article ID 524123, 8 pages

Editorial

Core-Shell Nanostructures: Modeling, Fabrication, Properties, and Applications

**Weihong Qi,¹ Linbao Luo,² Hai-Sheng Qian,³ Gang Ouyang,⁴
Karuna Kar Nanda,⁵ and Sherine O. Obare⁶**

¹ School of Materials Science and Engineering, Central South University, Changsha, Hunan 410083, China

² School of Electronic Science and Applied Physics, Hefei University of Technology, Hefei, Anhui 230009, China

³ College of Chemistry and Life Sciences, Zhejiang Normal University, Jinhua, Zhejiang 321004, China

⁴ Key Laboratory of Low-Dimensional Quantum Structures and Quantum Control of the Ministry of Education, Department of Physics, Hunan Normal University, Hunan Changsha 410081, China

⁵ Materials Research Centre, Indian Institute of Science, Bangalore 560012, India

⁶ Department of Chemistry, Western Michigan University, Kalamazoo, MI 49008, USA

Correspondence should be addressed to Weihong Qi, qiwh216@mail.csu.edu.cn

Received 4 December 2011; Accepted 4 December 2011

Copyright © 2012 Weihong Qi et al. This is an open access article distributed under the Creative Commons Attribution License, which permits unrestricted use, distribution, and reproduction in any medium, provided the original work is properly cited.

Core-shell nanostructures, a family of nanomaterials, have attracted increasing research interest due to their unique structural features that consist of an inner core and an external shell of different chemical compositions. These structural features allow the possibility of combining distinctive properties of varied materials. Comparatively, core-shell nanostructures have exhibited improved physical and chemical properties relative to their single-component counterparts. The inherent emergent chemical and physical properties of core-shell nanostructures are of great importance to a potentially broader range of applications including electronics, magnetism, optics, and catalysis. So far a large number of core-shell nanostructures have been successfully fabricated using approaches ranging from laser ablation and high-temperature evaporation to carbothermal reduction and hydrothermal methods. Structural characterization of these nanostructures and determination of their unique properties for various applications have been well documented. This special issue is devoted to describing a number of unique properties and applications of core-shell nanostructures by introducing a few research papers in this field.

The paper describes a simple emulsifier-free seed emulsion polymerization technique for the synthesis of perfluoropolyether-based core-shell nanoparticles. The shell consists of relatively high T_g polystyrene and polymethylmethacrylate that have a high glass transition temperature (T_g) as well as polyacrylic copolymers that have a low T_g.

The paper deals with the fabrication of polyaniline- (PANI-) TiO₂ core-shell nanostructures that were prepared via a novel ionic liquid/water microemulsion method in the presence of anatase TiO₂ nanoparticles. The paper reports the preparation of poly (methyl methacrylate)/SiO₂ (PMMA/SiO₂) hybrid composites using a “grafting onto” strategy, with assistance of UV light irradiation in an iron aqueous solution. The functionalization of PMMA was achieved by anchoring 3-(methacryloxy) propyl trimethoxysilane onto the nanosilica surface, followed by grafting PMMA onto the nanosilica layer with FeCl₃ as a photoinitiator. The paper presents a synthesis procedure of free standing Ge/GeO₂ core-shell nanocrystals with tunable sizes and shell thickness. High-resolution transmission electron microscope images reveal the presence of strain in the nanocrystals and lattice distortion/dislocations in the Ge core near the interface of Ge core and GeO₂ shell.

The paper of this special issue presents the preparation of silica-poly (methyl methacrylate) nanoparticles. Compared with pure natural rubber, the thermal resistance and tensile properties of such nanostructures are significantly improved. The paper is on the synchrotron X-ray absorption analysis of Fe₂O₃-Pt core-shell nanoparticles, obtained from the coreduction of iron acetylacetonate and platinum acetylacetonate. The paper reports the synthesis of a core-shell PMMA-grafted-ordered mesoporous silica by surface-initiated atom transfer radical polymerization of methyl methacrylate from

the exterior surface of ordered mesoporous silica particle. It was found that the as-prepared OMS(ordered mesoporous silica)-g-PMMA exhibited improved properties including ionic conductivity, thermal stability, and mechanical properties.

The paper explores the potential application of core-shell nanostructures. The paper proposes a new solution-based method for the synthesis of metal-hybrid nanocomposites including TiO_2 , Au/TiO_2 , ZnO , and Au/ZnO . These semiconductor-metal hybrid composites serve as a better catalytic system for photodegradation of malathion, one of the most commonly used pesticides in developing countries. The paper reports on silicon nanorods/carbon nanotubes (SiNRs/CNTs) for field emission cathodes. These novel nanostructures demonstrated improved field emission properties including a lower turn-on electric field, a lower threshold electric field, and a higher enhancement factor β , suggesting that such core-shell structures have good potential for field emission applications.

Weihong Qi
Linbao Luo
Hai-Sheng Qian
Gang Ouyang
Karuna Kar Nanda
Sherine O. Obare

Research Article

Preparation, Properties, and Self-Assembly Behavior of PTFE-Based Core-Shell Nanospheres

Katia Sparnacci,¹ Diego Antonioli,¹ Simone Deregibus,¹ Michele Laus,¹ Giampaolo Zuccheri,² Luca Boarino,³ Natascia De Leo,³ and Davide Comoretto⁴

¹*Dipartimento di Scienze dell' Ambiente e della Vita, Università del Piemonte Orientale "A. Avogadro", INSTM, UdR Alessandria, Via G. Bellini 25 g, 15100 Alessandria, Italy*

²*Dipartimento di Biochimica "G. Moruzzi", Università di Bologna, INSTM, CNRNANO-S3, Via Irnerio 48, 40126 Bologna, Italy*

³*NanoFacility Piemonte, Electromagnetism Division, Istituto Nazionale di Ricerca Metrologica Strada delle Cacce 91, 10135 Torino, Italy*

⁴*Dipartimento di Chimica e Chimica Industriale, Università degli Studi di Genova, Via Dodecaneso 31, 16146 Genova, Italy*

Correspondence should be addressed to Michele Laus, michele.laus@mfn.unipmn.it

Received 2 August 2011; Revised 17 October 2011; Accepted 24 October 2011

Academic Editor: Hai-Sheng Qian

Copyright © 2012 Katia Sparnacci et al. This is an open access article distributed under the Creative Commons Attribution License, which permits unrestricted use, distribution, and reproduction in any medium, provided the original work is properly cited.

Nanosized PTFE-based core-shell particles can be prepared by emulsifier-free seed emulsion polymerization technique starting from spherical or rod-like PTFE seeds of different size. The shell can be constituted by the relatively high T_g polystyrene and polymethylmethacrylate as well as by low T_g polyacrylic copolymers. Peculiar thermal behavior of the PTFE component is observed due to the high degree of PTFE compartmentalization. A very precise control over the particle size can be exerted by properly adjusting the ratio between the monomers and the PTFE seed. In addition, the particle size distribution self-sharpens as the ratio monomer/PTFE increases. Samples with uniformity ratios suited to build 2D and 3D colloidal crystals are easily prepared. In particular, 2D colloidal crystal of spheres leads to very small 2D nanostructuring, useful for the preparation of masks with a combination of nanosphere lithography and reactive ion etching. 3D colloidal crystals were also obtained featuring excellent opal quality, which is a direct consequence of the monodispersity of colloids used for their growth.

1. Introduction

A milestone in the tetrafluoroethylene (TFE) polymerization is represented by the development of the homo- and copolymerization microemulsion technology, on industrial scale, based on the use of perfluoropolyethers (PFPE) in oil/water microemulsion. A great deal of interest was focused on the resulting polytetrafluoroethylene (PTFE) nano- and microparticle latexes [1, 2]. PTFE aqueous dispersions featuring particle size as small as 10 nm can be produced, with particle concentration number as high as 10^{18} – 10^{19} (particles/liter). Moreover, by varying the amount and structure of PFPE as well as the quantity and nature of the comonomers, PTFE nanoparticles can be designed with highly differentiated architectures, including size, shape, and chemical composition.

Many interesting applications were disclosed for these PTFE nanoparticles including components in PTFE bimodal mixtures, ultralow-K dielectric materials, nanofillers for fluoroelastomers and fire-retardant additives with the reported purpose to inhibiting the dripping of molten particles from the burning polymer [3–6].

However, the compatibility and adhesion characteristics of PTFE and the various polymeric matrices are inadequate thus resulting in low dispersion degrees within the matrix and poor mechanical coupling among the various blend components. Moreover, the resulting compositions exhibit a pearl scent opaque appearance that prevents their use in applications where transparency is required. Finally, the poor dispersion of PTFE material adversely affects the efficiency in reducing the heat release.

To enhance wettability and compatibility, several PTFE surface modification strategies were developed based on either high power chemical and reactive processing procedures [7, 8] or high energy treatments [9, 10]. Reactive extrusion of electron-beam irradiated PTFE and polyamides was demonstrated [11–13] to be effective in the preparation of well-dispersed compounds due to the occurrence of transamidation reactions accompanied by the breakdown of the PTFE agglomerates. However, consistent degradation of the basic PTFE structure upon irradiation is unavoidable.

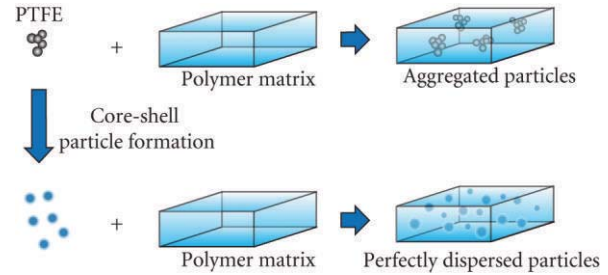
An alternative and promising nondestructive approach to produce compounds with a perfect dispersion of PTFE particles is based on the preparation of core-shell particles in which the core is constituted by PTFE and the shell by a conventional polymer. In the early studies, several composite particles consisting of PTFE core and crosslinked polybutadiene shell were described by Okaniwa [14] whereas the preparation of one sample only of core-shell particles in which the core is made up of PTFE and the shell of crosslinked PS was reported by Othegraven [15]. More recently, extensive studies were reported for core-shell nanoparticle systems composed of PTFE core and polyacrylic shell [16, 17] with various compositions.

Two-stage seeded emulsion polymerization is the general method [18, 19] to prepare latex particles featuring a core-shell morphology. The first stage, the core preparation, can be carried out either separately or *in situ* and the polymerization process of the second stage is a seeded process in which the second monomer is added continuously or batchwise to the reaction vessel. In most cases, some miscibility between the core polymer and the shell-forming monomer produces a partial swelling thus ultimately leading to an intermixing diffuse region. However, in the present case, the shell-forming monomer is always insoluble in the PTFE and the polymerization occurs exclusively in the shell region of the latex.

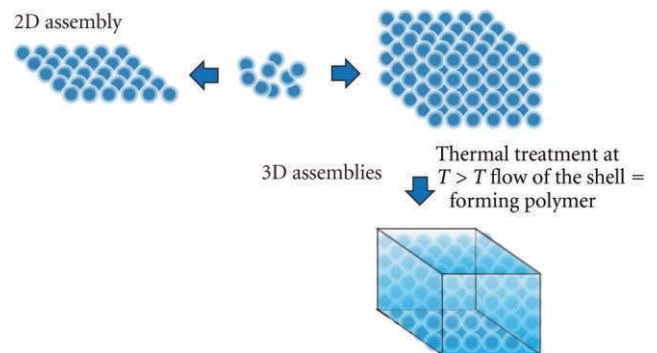
A perfect degree of dispersion of the PTFE particles within a polymer matrix could be obtained if the shell is constituted by the same polymeric material with which the polymer matrix is made up. The application of this concept leads to a novel class of specific and very efficient PTFE-based additives (Scheme 1).

An additional reason of interest for these core-shell nanoparticles is also related to their potential use as building blocks for colloidal crystals and other nanostructured materials [20–23]. They can self-assemble to generate 2D and 3D ordered structures which represent promising candidates in applications such as catalysis, sensing, optics, molecular separation, molecular reaction dynamics, single-molecule detection, and optoelectronics.

Two-dimensional structuration leads to 2D colloidal crystals which are extensively employed in nanosphere lithography [24] (NSL), among others. NSL is based on the self-assembly of nanospheres into close-packed monolayers or bilayers, which are then employed as lithographic masks to fabricate nanoparticle arrays. Consequently, NSL is an efficient, inexpensive, inherently parallel, material-specific, and high-output process for nanostructure fabrication process which can systematically produce a 2D array of periodic structures.



SCHEME 1: PTFE dispersion improvement through the use of core-shell particles.



SCHEME 2: 2D and 3D colloidal crystals from PTFE based core-shell particles.

The use of spherical colloids to obtain highly ordered periodic 3D structures, that is, photonic crystals, opens novel perspectives in organic photonics since the periodic modulation in structure and composition allows to control light propagation and emission [25].

In addition to the building up of conventional opals, once a well-ordered assembly of core-shell particles is obtained, annealing at a temperature higher than the flow transition temperature of the shell-forming polymer allows the shell-forming polymer to soften and form a matrix surrounding 3D periodic array of in which the PTFE particles are arranged in regular registry. Since the characteristic size of the different domains is on the nanometer range, nanoscale thin films and three-dimensional materials can be prepared (Scheme 2).

For these applications, the particle size control represents the key to produce successful nanostructures. As monodispersed particles in the 30 nm to 1 micron size range are involved in the preparation of nanostructured materials, emulsion polymerization [26] is the most suitable particle forming technique. In this process, the most important parameter, that controls the particle nucleation, is the surfactant concentration. A narrow particle size distribution can be achieved when a low surfactant concentration is employed [27, 28]. The “surfactant-free emulsion polymerization” (SFEP) represents an efficient technique to prepare monodisperse latexes because the time for nucleation is extremely short. However, SFEP approach affords particles with size generally comprised between 300 and 800 nm whose monodispersity is not always guaranteed. In addition,

TABLE 1: PTFE latex characteristics.

PTFE latex	Shape	d (nm)	Solid content (g/L)	No. of particles (L^{-1})	Conductivity ($\mu S/cm$)	Zeta potential (mV)
BPM	Sphere	20	150.8	1.7×10^{19}	850	-56
BP44	Sphere	26	350.4	1.8×10^{19}	520	-50
DV2	Sphere	33	358.3	6.8×10^{18}	460	-38
MD	Sphere	41	347.6	3.1×10^{18}	280	-51
DV3	Rod-like	62	294.5	1.2×10^{18}	415	-41
D60	Sphere	130	280.2	1.7×10^{17}	560	-35
D60G	Sphere	240	296.8	1.9×10^{16}	430	-38

a certain variability in the final average particle size is observed.

A related approach to prepare such nanosized particles [29, 30] relies on the seeded emulsion technique starting from seeds of a few nanometers. These can be prepared *in situ* by a self-seeding technique or can derive from a distinct preparation. Considering the latter approach, polytetrafluoroethylene (PTFE) latexes with particles in the submicrometer size range can be successfully employed as seeds in the emulsifier-free emulsion polymerization of various monomers including styrene [31, 32], acrylic mixtures [33], or methyl methacrylate [34–36] or thus leading to a wide variety of core-shell nanosphere architectures featuring a relatively narrow size distribution. In this paper, we review our most recent results concerning preparation, properties and self-assembly behavior of PTFE-based core-shell particles using polytetrafluoroethylene (PTFE) latexes with particles in the submicrometer size range, as seeds in the emulsifier-free emulsion polymerization of various monomers thus leading to a wide variety of core-shell nanosphere architectures in which the shell-forming polymers can be designed with glass transition or flow transition temperatures above or below room temperature.

2. Experimental Part

2.1. Materials. The PTFE latexes employed in this study and provided by Solvay Solexis were marked BPM, BP44, DV2, DV3, D60, D60G, and MD. Their characteristics, including particle radius and particle shape, the solid content, the particle number concentration, and the conductivity are collected in Table 1. The monomers styrene (99% Aldrich), butylacrylate ($\geq 99\%$, Aldrich), methylacrylate ($\geq 99\%$, Fluka), ethylacrylate ($\geq 99\%$, Fluka), and methyl methacrylate (99% Fluka) were distilled under reduced pressure in nitrogen atmosphere and stored at $-18^\circ C$ until use. Methacrylic acid ($\geq 98.0\%$, Fluka) and potassium persulfate (98%, Carlo Erba) were used without further purification. The C1 mixture is constituted by methylacrylate, ethylacrylate, and methacrylic acid with weight percent of 39, 57, and 4%, respectively. The C2 mixture is constituted by butylacrylate and methacrylic acid with weight percent of 96 and 4%, respectively.

2.2. General Preparation of PTFE-Based Core-Shell Nanospheres. The PTFE-based core-shell colloids were syn-

TABLE 2: Already published core-shell series and corresponding references.

Series	Reference
MDS, DV2S, DV3S	[31]
BPMS	[32]
MDC1, MDC2	[33]
MDM, DV2M, DV3M	[34]
BPM, D60M	[35]
MM	[36]

thesized in a 1 L five-neck jacketed reactor equipped with a condenser, a mechanical stirrer, a thermometer, and inlets for nitrogen and monomer(s). First, the appropriate amount of PTFE latex was introduced into the reactor containing 500 mL of deionized water at room temperature with a stirring rate of 300 rpm. The mixture was purged with nitrogen for 20 min and nitrogen was flushed during the entire polymerization procedure. Next, the mixture was heated to $75^\circ C$ and the monomer(s) was added. Then, after additional 15 min of equilibration time, the potassium persulfate aqueous solution (10 mL, 0.74 mmol) was added and the mixture was reacted for 24 h. The obtained latex was purified from the unreacted monomer by repeated dialyses using a membrane with MWCO of 12.4 KDa. All the latexes were obtained following the above general procedure by varying the initial PTFE latex amount. Starting from the various PTFE seeds and changing the ratio between the PTFE and the monomer(s), several sample series were obtained. The series were marked with an acronym comprising the PTFE seed, the type of monomer or comonomeric mixture, and a number which relates to the initial PTFE weight percent with respect to the monomer or comonomeric mixture. As an example, the MDMn series is obtained from the MD latex and methylmethacrylate (M) whereas styrene and the two acrylic mixtures are indicated as S, C1, and C2, respectively. The experimental details of the already published sample series are described in the corresponding papers as summarized in Table 2. The experimental details of series MDS and D60GS are reported in Tables 3 and 4.

2.3. Preparation of 2D and 3D Colloidal Crystals. 2D colloidal crystals were prepared by the floating technique [37–39], on the air liquid interface and then lifted on the surface of a solid substrate. With this method, the original dispersion

TABLE 3: Synthesis details, yield, and solid content of the various samples.

Sample	Volume of water (mL)	Volume of Styrene (mL)	Volume of PTFE latex (mL)	Yield (%)	Solid content (g/mL)
MDS1	500.0	70.0	0.46	89.6	0.1078
MDS2	500.0	70.0	0.92	98.4	0.1104
MDS3	500.0	70.0	1.85	100.0	0.1140
MDS4	500.0	70.0	5.67	100.0	0.1210
MDS5*	500.0	70.0	10.00	76.4	0.1121
MDS6	500.0	70.0	18.10	100.0	0.1241
MDS7*	500.0	70.0	19.90	77.0	0.1128
MDS8*	500.0	70.0	39.90	83.0	0.0650
MDS9*	500.0	70.0	59.40	81.7	0.1247
D60GS1	500.0	70.0	30.65	85.3	0.1106
D60GS2	500.0	70.0	50.30	83.6	0.1087

* Published in [31].

TABLE 4: Sample composition derived from TGA and DSC, glass transition temperature, diameter estimated, PCS Size, SEM size, and uniformity ratio of the various samples.

Sample	% PTFE Theoretical (W/W)	% PTFE (TGA)	% PTFE (DSC)	d estimated (nm)	d PCS (nm)	d SEM (nm)	Uniformity Ratio U
MDS1	0.25	0.21	0.11	383	417	380	1.003
MDS2	0.50	0.47	0.33	304	309	301	1.004
MDS3	1.00	0.85	0.67	241	245	237	1.005
MDS4	3.00	2.91	2.08	167	166	163	1.007
MDS5*	5.20	5.20	4.30	138	139	133	1.012
MDS6	9.00	8.70	7.67	114	115	111	1.028
MDS7*	9.80	6.70	7.9	111	113	107	1.030
MDS8*	17.90	19.4	16.8	89	92	84	1.050
MDS9*	24.50	22.7	22.7	80	89	75	1.100
D60GS1	12.5	12.0	12.4	596	604	593	1.004
D60GS2	19.0	18.0	19.3	511	525	500	1.004

* Published in [31].

(eventually diluted to reach typical concentrations ranging from 5 to 10% in water) is mixed with ethanol (1 : 1 V/V). This gives an accurate control of the floating level of the monolayers on the water surface thus allowing the formation of large 2D crystals screening the surface charge on the sphere by water molecules. The final addition of a surfactant in the water further compacts the 2D crystalline islands. In this phase, parameters like sphere surface charge, ethanol content, and dispersion method are rather critical in the formation of large crystal assemblies. Silicon substrates have been used to lift the floating crystals.

3D colloidal crystals were grown by using the vertical deposition technique [40] starting from core-shell latexes properly diluted with deionized water. Growth occurred on glass substrates at $45 \pm 1^\circ\text{C}$ inside a BF53 Binder incubator. Opals were composed of flat domains with the [111] direction of the face-centered cubic lattice of spheres perpendicular to the substrate. In the best samples, domain sizes are 50–100 microns. However, defects inside these domains, in particular stacking faults, cannot be excluded. Opals are marked with the prefix O before the name of the sample employed to build up the corresponding opal.

2.4. Characterization. Scanning electron microscope (SEM) analysis was performed using an Inspect F SEM-FEG (Field Emission Gun) from FEI company, with a beam diameter of 3 nm. The SEM micrographs were elaborated by the Scion Image processing program. Photon correlation spectroscopy (PCS) analysis at 25°C was performed with a Malvern Zetasizer 3000 HS at a fixed scattering angle of 90° , using a 10 mV He-Ne laser and PCS software for Windows (version 1.34, Malvern, UK). Each value is the average of five measurements. The instrument was checked with a standard polystyrene latex with a diameter of 200 nm. Electrophoretic mobility was measured with a Malvern Zetasizer 3000 HS. Each value is the average of five measurements.

SFM analysis was performed with Tapping-Mode Atomic Force Microscopy in air on a Multimode Nanoscope IIIa instrument (Veeco, S. Barbara, CA, USA) operated in constant amplitude mode. A multilayer of nanoparticle is obtained by drop casting and aliquot of water suspension on a disc of freshly cleaved muscovite mica (Electron Microscopy Sciences, Hatfield, PA, USA) and the solvent is allowed to slowly evaporate. Images are then subjected to flattening using the microscope constructor software.

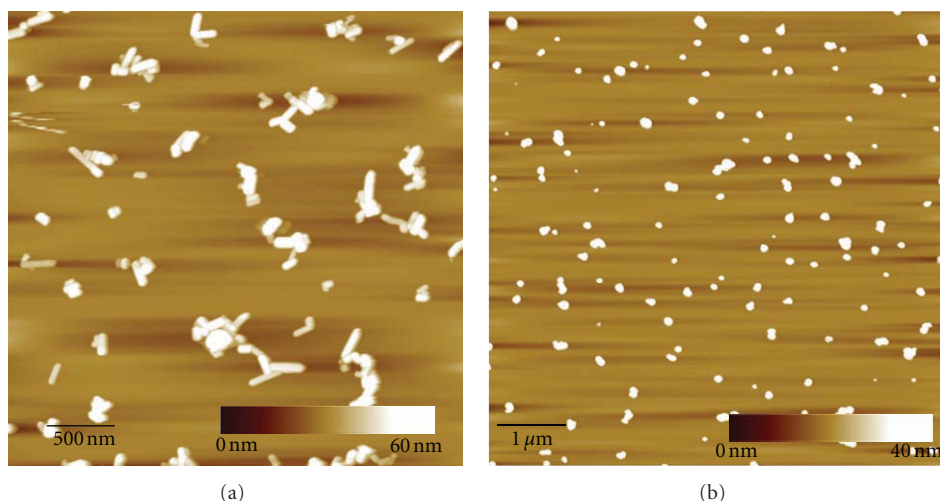


FIGURE 1: AFM images of sample DV3 (a) and MD particles (b) [34].

Thermogravimetric analysis (TGA) was performed with a Mettler-Toledo TGA/SDTA851^e at a scanning rate of 10°C/min from room temperature up to 1100°C under nitrogen flow. The solid content of latex dispersions was determined by TGA. Differential scanning calorimetry (DSC) was carried out using a Mettler-Toledo DSC 821 apparatus. Samples of about 5 mg were employed. The instrument was calibrated with high purity standards at 10°C·min⁻¹. Dry nitrogen was used as purge gas.

Reactive Ion Etching (RIE) was performed in oxygen plasma, at an operative pressure of 3.0E-1 mbar, flux of 80 sccm, 80 W RF power, with etching time ranging from 20 to 120 seconds.

Transmittance (T) and reflectance (R) spectra were recorded with Avantes Avaspec-2048 compact spectrometers (230–1100 nm spectral range, ~1.4 nm spectral resolution). Light from a combined deuterium/tungsten-halogen lamp was guided by an optical fiber to a proper collimating optics (spot diameter variable in the range 0.5–5 mm) on the sample, which is mounted on a goniometer. Transmitted light was collected and driven by another optical fibers to the spectrometer. Normal incidence reflectance was measured on six different 2 mm diameter spots by a Y reflection probe bundle fiber. Light was linearly polarized by using a Glenn-Thompson Halbo Optics polarizer. All details on the optical set-up are reported in [41].

3. Results and Discussion

3.1. Synthesis. PTFE latexes with different size and shape were prepared by microemulsion polymerization and employed as seeds in the successive emulsifier-free seeded emulsion polymerizations. In particular, BPM, BP44, DV2, MD, D60, and D60G latexes consist of spherical particles with average diameters of 20, 26, 33, 41, 130, and 240 nm whereas DV3 consists of rod-like particles with an equivalent radius of 62 nm and an axial ratio of 3.2 (Table 1). As typical examples, Figure 1 reports the AFM images of samples MD

and DV3. As the presence of the residual surfactant deriving from the TFE microemulsion polymerization could interfere with the successive emulsifier-free seeded emulsion polymerization, all the PTFE latexes were thoroughly dialyzed. At the end of the purification process, the conductivity of all the PTFE latexes was lower than 150 μ S/cm.

The emulsifier-free seeded emulsion polymerizations of the various monomers including styrene, methylmethacrylate, and the acrylic mixtures C1 and C2 were performed by adding appropriate amounts of the PTFE latex and monomers into deionized water and running the reactions at 75°C for 24 hrs using potassium persulfate as the free radical source. At the end of the reaction, the latexes were purified by repeated dialyses. In all the polymerization reactions, monomer(s) and potassium persulfate as well as the water content were kept constant, whereas variations were allowed in the amount of PTFE. Under these conditions, the initial PTFE weight percent with respect to monomer(s), and PTFE was varied from 0.25 to 90%. No gel trace or polymeric gross aggregates were found in all cases. Nearly quantitative monomer conversion and nanosphere yield were obtained. The final latexes are very stable (up to two years).

3.2. Size and Size Distribution of the Core-Shell Particles. Figure 2 reports the SEM micrographs of samples D60GS1, MDS3, BPM7, and DV2M1.

Although these samples are prepared starting from PTFE seeds differing in their size and using styrene or methylmethacrylate as the shell-forming monomer(s), in all cases they feature a quite narrow size distribution.

The composition of all the samples can be easily estimated from the TGA analysis, as reported in Figure 3 for typical samples. In all the thermograms, there are two main losses. The lower temperature loss is associated to the degradation of the shell-forming polymers which occurs at 410°C (midpoint) for polystyrene, at 350°C for polymethylmethacrylate, and at 390°C for the two acrylic mixtures C1 and C2 whereas the weight loss at 570°C

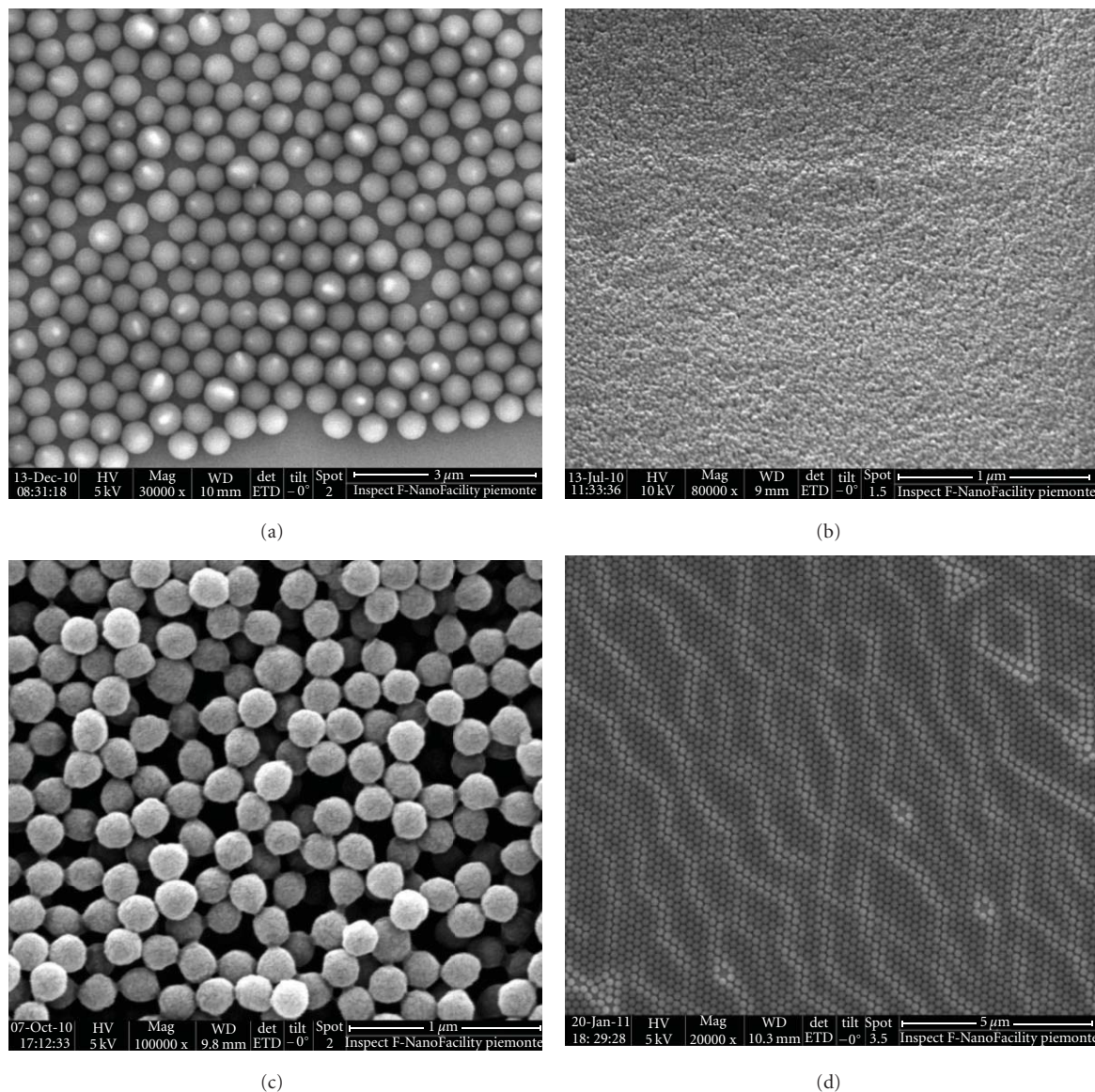


FIGURE 2: SEM micrographs of samples D60GS1 (a), BPM7 (b), DV2M1 (c), and MDS3 (d) [34, 35].

corresponds to PTFE decomposition. The composition of the various samples is in excellent agreement with the one calculated from the amount of the initially added PTFE and monomer or comonomeric mixtures.

The size and size distribution of the various samples were studied using a combination of SEM, AFM, and PCS analysis. Figure 4 reports typical PCS curves for MDSn series and, for comparison purposes, the PCS curve of the MD latex. No residual PTFE deriving from MD latex is present in the various samples, thus indicating that PTFE is highly efficient as seed in the styrene polymerization.

Figure 5 reports the SEM images for series MDSn as well as the size distribution, including the uniformity ratios U [42] whereas Figure 6 illustrates the trend of the particle diameter and the uniformity ratio as a function of the S/PTFE weight ratio.

Over the entire S/PTFE range, the particle size increases as the S/PTFE ratio increases indicating that secondary nucleation was prevented with all the monomer ending up as shell polymer. In addition, the uniformity ratio U decreases regularly as the ratio S/PTFE increases.

The described trend is observed in all the sample series prepared starting from the various PTFE seeds and using styrene or methylmethacrylate. To make a homogeneous comparison, the size and U data are plotted as a function of the ratio between the amount of styrene or methylmethacrylate and the number of PTFE particles in the reaction mixture. Figure 7 illustrates the various data.

For both monomers, the size and uniformity ratio trends are very similar. The particle size increases as the ratio between the amount of monomer and the number of PTFE particles increases whereas the relevant size distribution

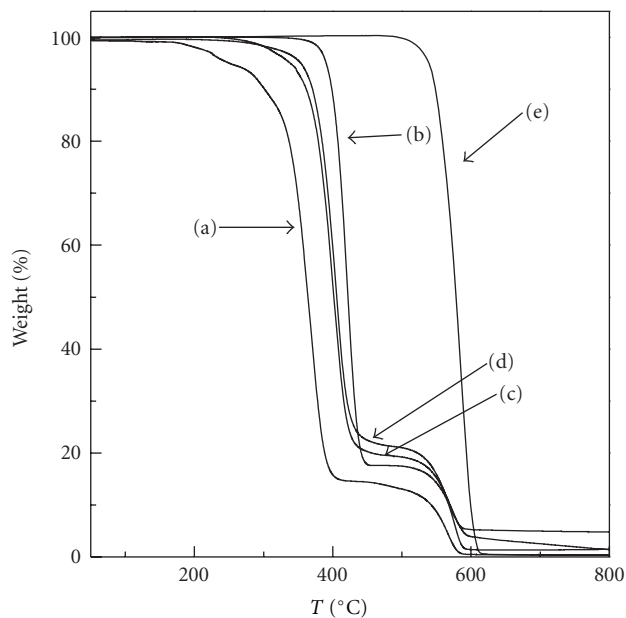


FIGURE 3: TGA curves at 10°C/min heating for various samples: DV2M4 (a), D60GS2 (b), 18MDC1 (c), 18MDC2 (d), and latex MD (e) [33–35].

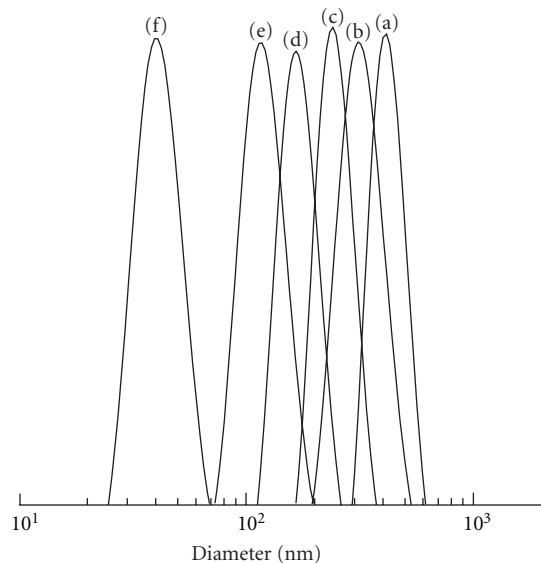


FIGURE 4: PCS spectra of MDS1 (a), MDS2 (b), MDS3 (c), MDS4 (d), MDS6 (e), and latex MD (f), (unpublished data).

decreases. Provided that no pure PMMA and PS or PTFE nanospheres are present at the end of the reaction, and taking into account the yield values, the size of the core-shell nanospheres can be estimated from the amount of the initially added PTFE and the relevant monomer. In all cases, the estimated size is in close agreement with the observed one. This indicates that over the entire monomer/PTFE range, secondary nucleation was prevented with all the monomer ending up as shell polymer. The inhibition of the

secondary nucleation suggests that the PTFE seed particles are able to capture all the unstable nuclei produced in the system even at very high monomer/PTFE ratios, thus avoiding the formation of stable secondary particles. A direct consequence of this observation is that particle size versus S/PTFE curve is superposable to the particle size versus M/PTFE curve. The overall picture of these data clearly indicates that a very precise control over the particle size and size distribution can be exerted by properly adjusting the ratio between the monomer and the PTFE seed.

It is also interesting to speculate about the tendency toward an increasing size uniformity as the ratio monomer/seed increases. During Smith-Ewart Interval II [19], the growing mechanism involves diffusion of monomer from the droplets to the particles and the growing probability appears related to the latex particle surface area. Consequently, bigger particles should display a growing probability higher than smaller particles. However, this mechanism would ultimately lead to an increase in the size distribution, in contrast with the experimental observations. We suggest that the thermodynamic tendency toward a reduction of the surface to volume ratio could produce an increased tendency of the smaller particles to absorb the monomer with respect to the bigger ones thus ultimately leading to size uniformity, provided that the monomer to seed ratio is sufficiently high. This suggestion is also in agreement with the competitive growth mechanism [19] of latex particles which indicates that small latex particles grow faster in size than larger ones, thus leading to narrow size distribution, when the particle size is lower than the critical value of 150 nm whereas the opposite occurs when the particle size is much larger than 150 nm. This general behavior is also very similar to the one described [43] for the seeded dispersion polymerization of methylmethacrylate using PMMA submicron seeds. In that system, the final number of particles was nearly the same as the initial number of seed particles thus allowing the final particle size to be precisely controlled leading to the target particle size with excellent reproducibility. In addition, although no explanation was given, a self-sharpening of the size distribution was also observed with increasing the monomer to seed ratio.

Similar results can be obtained in the case of the seeded polymerization of the two acrylic mixtures C1 and C2 starting from the MD PTFE seed. As a typical example, Figure 8 reports the AFM image of sample MDC1-3.

No residual MD latex is present in the various samples and monomodal and narrow size distribution of the latex particles are generally obtained. However, the particle size estimated assuming the presence of core-shell nanospheres only and quantitative yield is definitely lower than the core-shell particle diameters observed for series MDC1n and MDC2n (Figure 9).

In addition, the size of samples belonging to MDC1n series is always higher than the one of the corresponding samples of MDC2n series. These two observations suggest that in both sample series the shell is swollen in water possibly due to the presence of the ionic and pH-sensitive methacrylic acid units. The swelling degree appears lower for series nMDC2 due to the presence of butylacrylate units

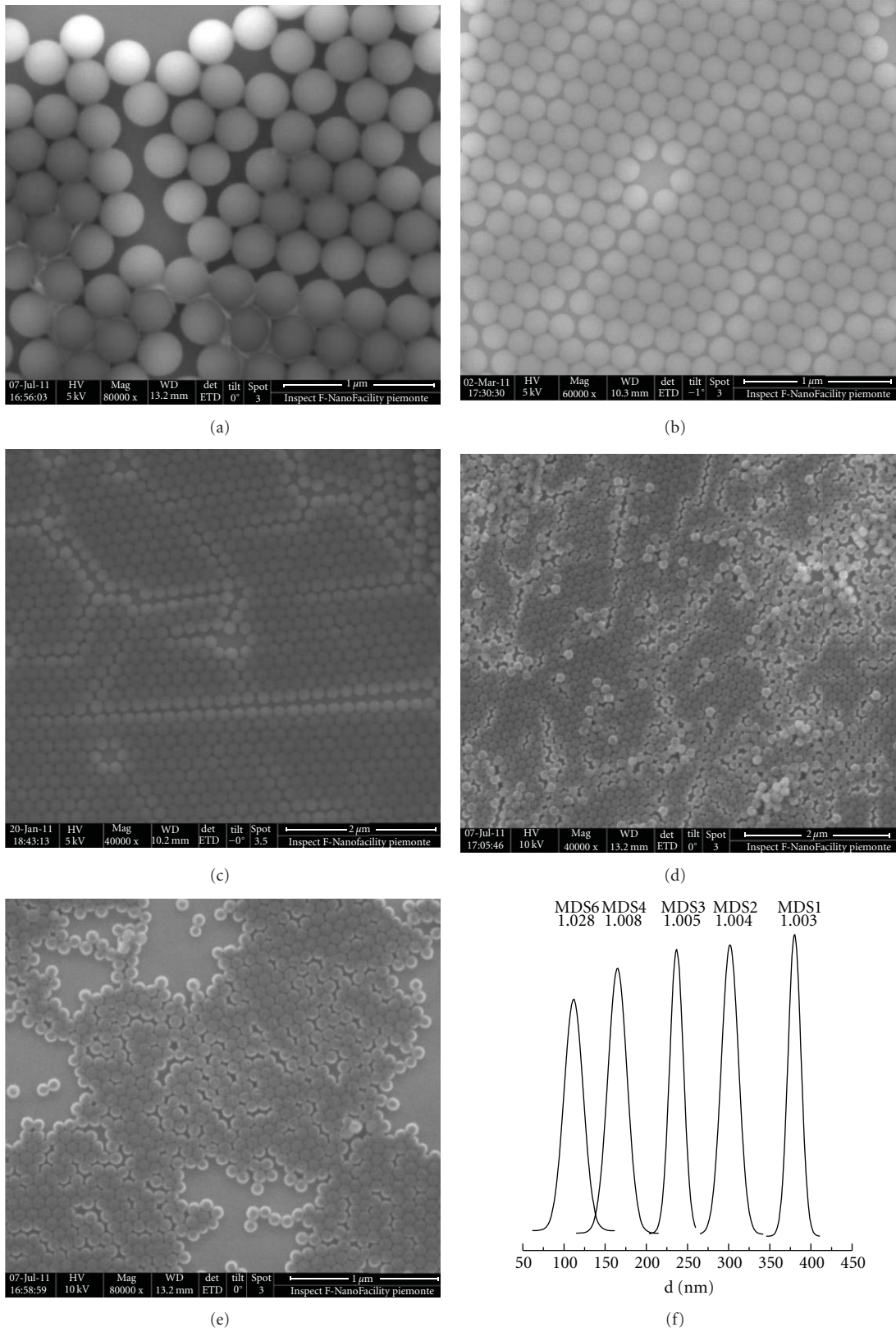


FIGURE 5: SEM micrograph of samples MDS1 (a), MDS2 (b), MDS3 (c), MDS4 (d), MDS6 (e), and relative diameter distribution (f), (unpublished data).

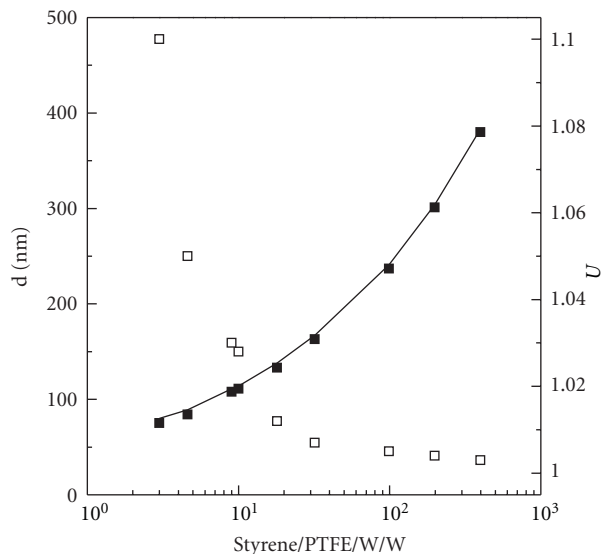
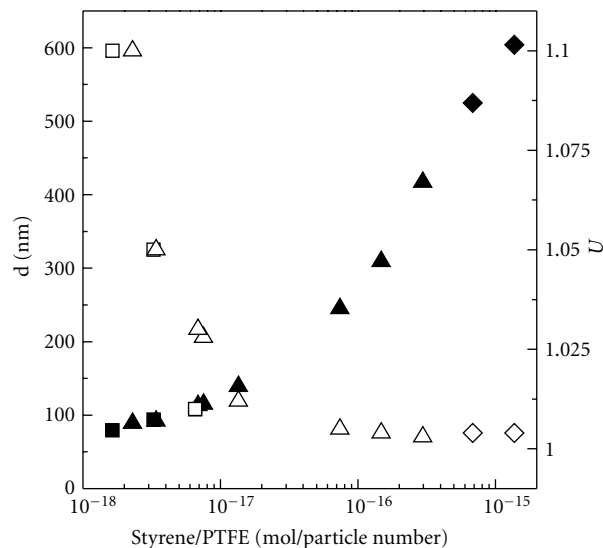


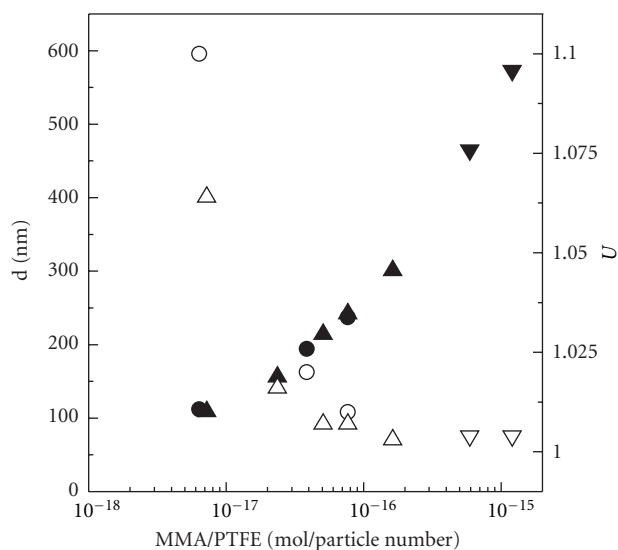
FIGURE 6: Particle size (d) and uniformity ratio (U) as a function of the S/PTFE weight ratio [31].

which are less hydrophilic than methyl- or ethylacrylate units which constitute the shell of nMDC1 series. PCS measurements confirmed this hypothesis and indicated a pH dependence of the particle size. This effect could be employed to produce 2D ordered layers with distinct periodicities by assembling the core-shell particles after equilibration at different pH values.

3.3. Thermal Behavior. The thermal behavior of the various samples was studied by combined differential scanning calorimetry and thermogravimetric analysis. Figure 10 illustrates the DSC heating and cooling traces of various sample in which the shell is constituted by PMMA, C1, and PS. The same figure reports the DSC traces of the seed MD, as a typical PTFE sample. In all the core-shell samples, at low temperature a step can be observed, due to the glass transition of the shell-forming polymer whereas, at high temperature, an endothermic transition is present, attributed to the PTFE melting. The crystallization of MD sample, at $-10^{\circ}\text{C}/\text{min}$ cooling rate, is observed at 310°C in agreement with literature data [44]. In contrast, the crystallization of PTFE cores in the three core shell samples occurs at 270°C . This peculiar crystallization behavior, recently described and thoroughly discussed [45] for a series of PTFE/PMMA core-shell nanoparticles, and also observed in PTFE blends with polyamides [12, 13], can be rationalized within the frame of the fractionated crystallization mechanism [46]. It is a characteristic of crystalline polymers to exhibit multiple crystallization transitions when dispersed as small particles [46] as may occur in some polymer blends [47, 48] or microphase separated in block copolymers [49]. In these cases, the number of the dispersed particles is much greater than the number of heterogeneities that usually nucleate the polymer in bulk. Then, the polymer crystallization occurs in one or more stages reflecting the nucleation



(a)



(b)

FIGURE 7: Particle size (d , fully symbols) and uniformity ratio (U , open symbols) as a function of the initial mol of monomer/PTFE particle number ratio for styrene (a) and methylmethacrylate (b): BPM (■), BP44 (●), MD (▲), D60 (▼), and D60G (◆), [31, 32, 34–36].

by different heterogeneities and consequently activated at different degrees of undercooling. The particles that do not contain a heterogeneity eventually nucleate through homogeneous nucleation, at the largest undercooling. In the present case, due to the compartmentalization of PTFE within the core-shell nanospheres, the number of the dispersed PTFE particles is much greater than the number of heterogeneities that usually nucleate the polymer in bulk. In these conditions, only one crystallization component at very high undercooling is observed, possibly deriving from the homogeneous nucleation mechanism. In turn, the observation of the single low-temperature crystallization

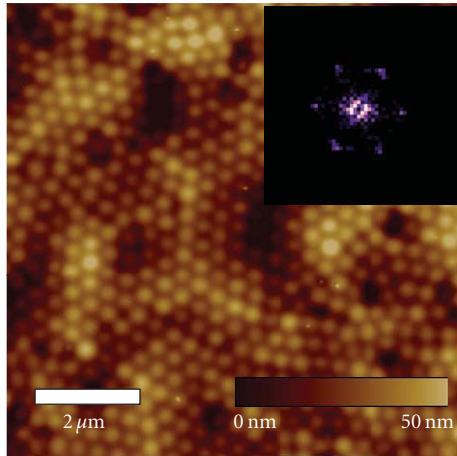


FIGURE 8: AFM image and 2D Fourier spectrum (inset) for the MDC1-3 specimen. Tapping-mode AFM image obtained from a film of core-shell nanoparticles that has been obtained from solvent evaporation on a drop-casted spread on a freshly cleaved muscovite mica disc. Heights are coded in shades according to the reported colour bar. The 2D Fourier transform of the central portion of the image (in the inset) shows the six intensity peaks denoting periodicity and hexagonal compact structure of the film with a periodicity of approximately 300 nm (correspondent to the measured average interparticle distance) [33].

exotherm can be viewed as a proof for the occurrence of a perfect dispersion of the PTFE seeds.

It should be observed that the melting of PTFE occurs at a temperature at which the shell forming polymers undergo thermal degradation. In fact, Figure 11 reports a series of successive DSC heating and cooling curves for sample. In the first cooling curve only the crystallization at 270°C can be observed whereas in the successive cooling traces the PTFE crystallization is structured into two components but it is apparent that the relative intensities of the peaks is different from the previous cooling curve. In particular, the intensity of the crystallization peak at 310°C increases whereas the opposite occurs for the crystallization component at 270°C.

This phenomenology is related to the parallel thermal decomposition of the PMMA shell which occurs through the well-known mechanism of random chain scission and followed by depropagation [50–52]. The unzipping and loss of the MMA allow the PTFE seeds to coalesce (Scheme 3).

The resulting increase in the PTFE domain size increases in turn the crystallization propensity of PTFE as demonstrated by the appearance and progressive growth of the PTFE crystallization component at 310°C.

3.4. 2D and 3D Colloidal Crystals. Several experiments were performed to obtain ordered 2D and 3D colloidal crystals. In particular, 2D colloidal crystal of spheres was formed by the floating technique [37–39], on the air liquid interface and then lifted on the surface of a solid substrate. Ordered monolayer samples of BPMS-3 underwent Reactive Ion Etching (RIE), a physical-chemical dry etching technique widely used in silicon technology to remove material in

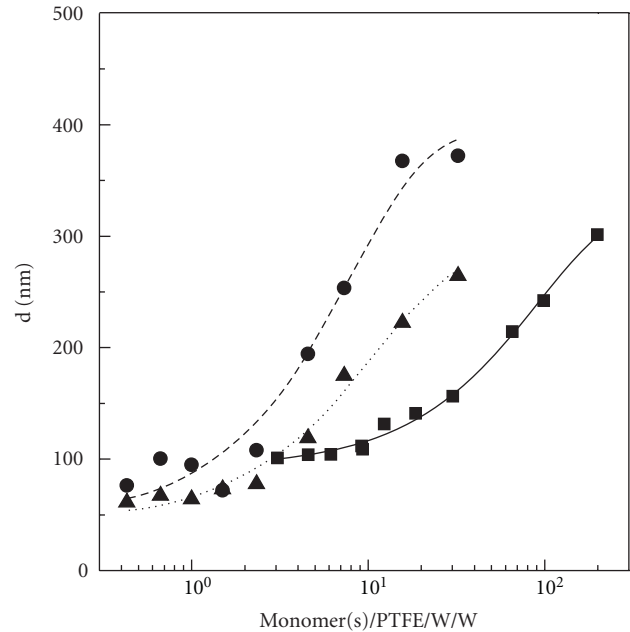
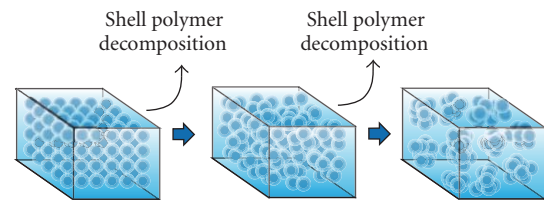


FIGURE 9: Trend of particle diameter as a function of initially PTFE added using MD latex as seed and different acrylic mixtures for shell: methyl methacrylate (■ and continuous line), acrylic mixture C1 (• and dashed line), and acrylic mixture C2 (▲ and dotted line) [33, 34, 36].



SCHEME 3: Decomposition of PMMA and PTFE seeds coalesce for a sample subjected to DSC heating-cooling cycles.

excess during microfabrication processes. The RIE was performed in oxygen plasma, at an operative pressure of 3.0E-1 mbar, flux of 80 sccm, 80 W RF power, at different etching time ranging from 20 to 120 seconds, as illustrated for a typical preparation in Figure 12.

Once subjected to RIE treatment, the nanospheres start reducing in size but the 2D structuring is not lost possibly because of the ionic anchoring of the negatively charged particles to the silicon surface. As the RIE time increases, the particle size decreases but the 2D ordering does not appear substantially perturbed. As the final particle size after 80 s RIE time is about 35 nm. This value represents the smallest 2D nanostructuring obtained by RIE [53] for the preparation of masks with a combination of nanosphere lithography and reactive ion etching.

3D colloidal crystals were prepared starting from various MDMn latexes. The corresponding opals, named OMDMn, were composed of flat domains with the [111] direction of the face-centered cubic lattice of spheres perpendicular to the glass substrate. The evolution of the stop band

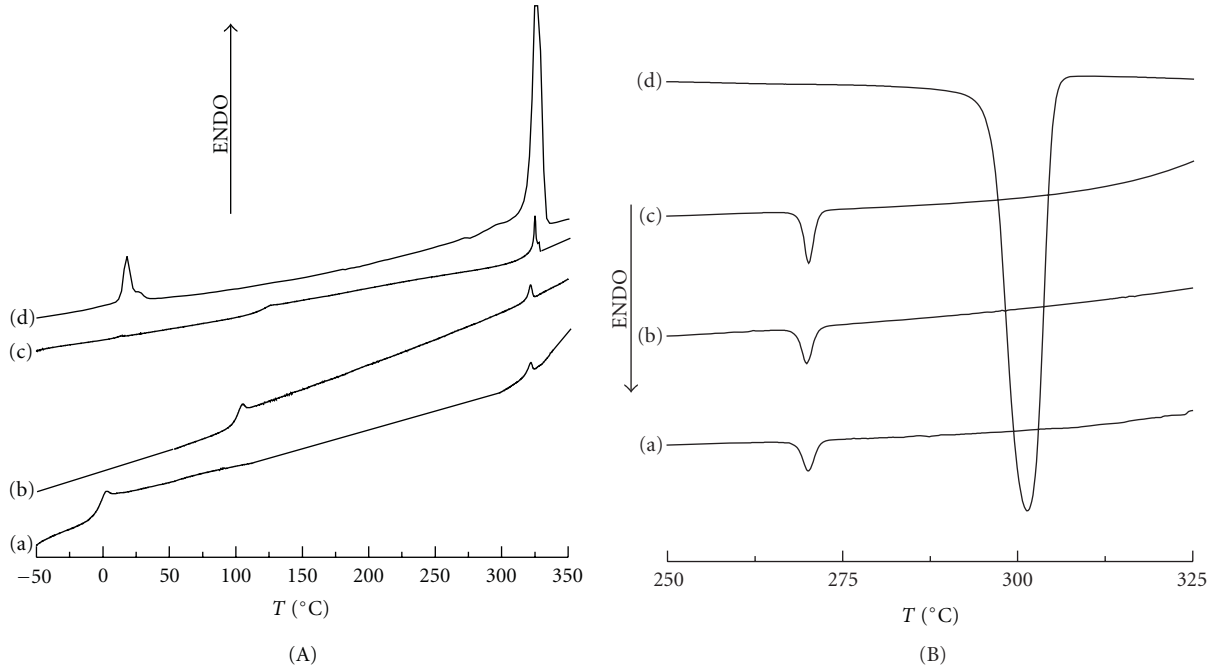


FIGURE 10: DSC first heating (A) and first cooling (B) at 10°C/min of samples MDC1–3 (a), MDS3 (b), MM4 (c), and latex PTFE (d). DSC traces for PTFE sample were divided by ten times [31–33, 36].

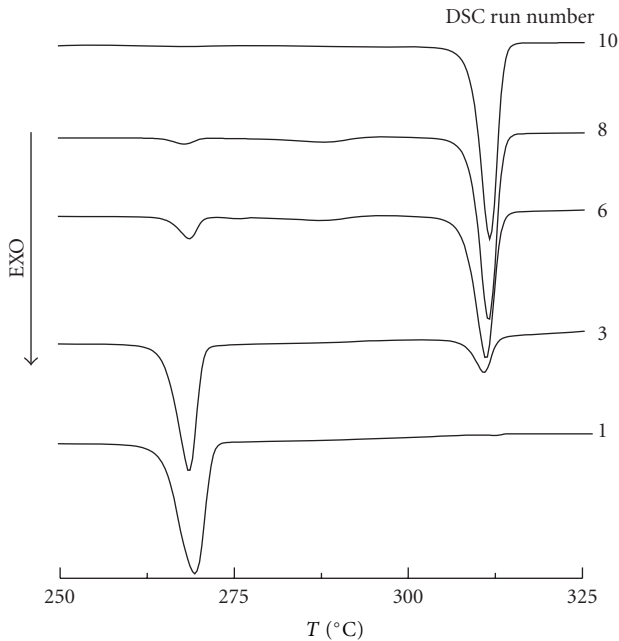


FIGURE 11: Successive DSC cooling curves at 10°C/min of DV2M4 sample subjected to a series of heating-cooling cycles from 200 to 360°C [45].

was studied both by reflectance spectra and transmittance spectroscopy at varying angles of incidence and as a function of polarization.

Figure 13 shows the SEM image of the opal OMDM1 and the corresponding near normal incidence reflectance spectrum.

The main reflectance peak is assigned to the Bragg peak due to the pseudogap along the ΓL (111) crystallographic direction of the FCC colloidal crystal. The spectral position of the stop band is determined only by the lattice spacing and the refractive index of composing materials [54]. A simple analytical form for the Bragg peak position, widely adopted for opals, is provided by the Bragg-Snell law [55]:

$$m\lambda_B = 2D\sqrt{n_{\text{eff}}^2 - \sin^2\theta}, \quad (1)$$

where m is the diffraction order, D , the interplanar spacing; n_{eff} , the effective refractive index of the PhC, and θ the incidence angle. In the case of a close packed FCC lattice, $D = (2/3)^{0.5}d$.

Additional features are observed in the reflectance spectrum below 400 nm. These peaks are a consequence of the complex opal photonic band structure occurring at energies higher than the pseudogap (corresponding to $m = 2$ and 3 in the Bragg-Snell law) and due to light diffraction along directions different from the incident one [56, 57]. The final characteristic of the spectrum is the presence on its background of an extended Fabry-Perot-like interference fringes pattern indicative of the optical quality of the opals, which can be used to determine the sample thickness as soon as the n_{eff} of the system is known [55]. In order to determine n_{eff} angle resolved spectroscopy combined with a fitting procedure through (1) is useful (see below).

Indeed, it is well known that the opal photonic band structure depends both on the wave vector of light and its

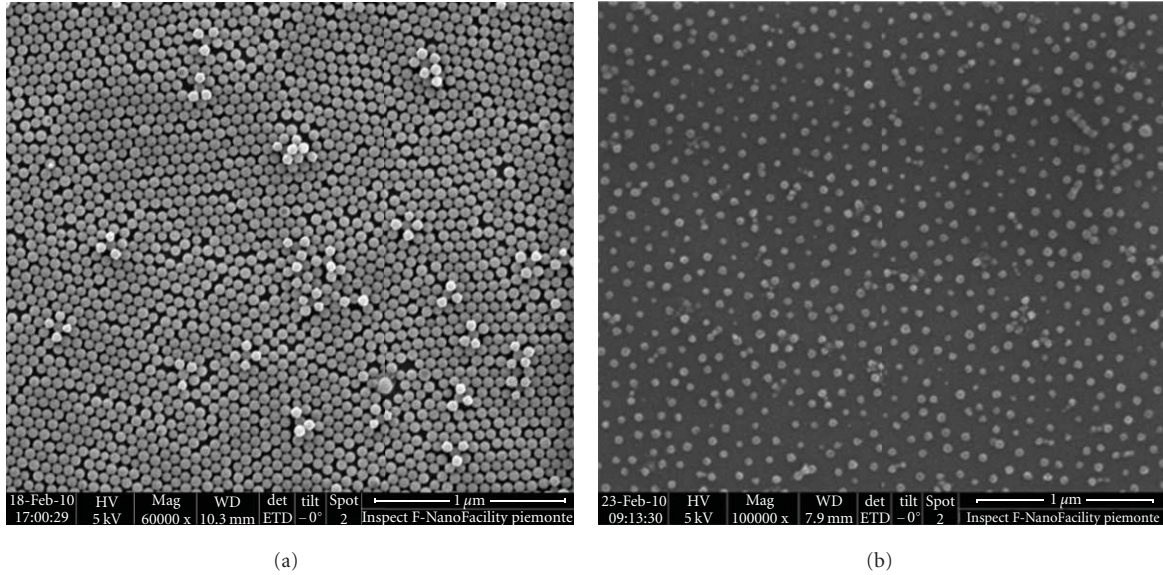


FIGURE 12: SEM micrographs of sample BPMS-3 after different RIE times: 0 s (a), 80 s (b) [32].

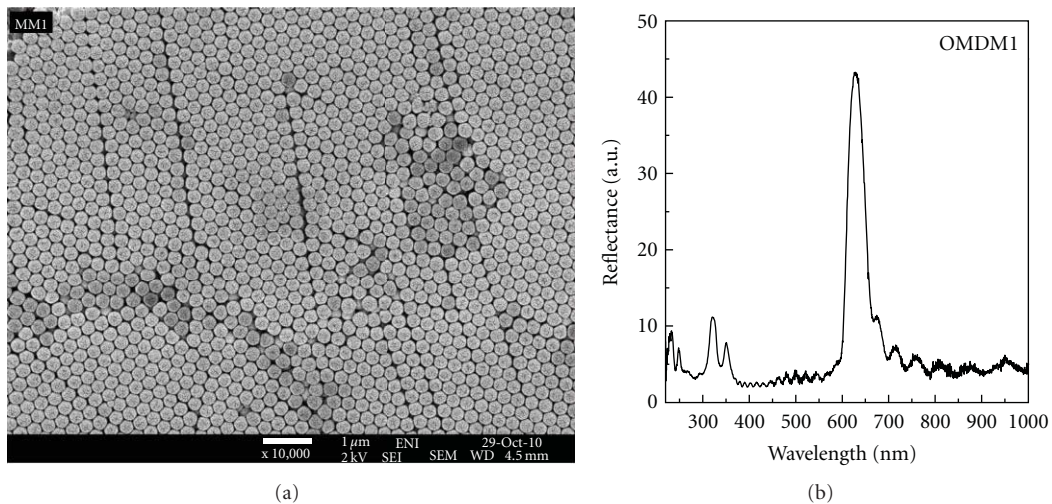


FIGURE 13: SEM micrograph (a) and reflectance spectrum of opal OMDM1 sample (b) [36].

polarization [56, 58, 59]. All these properties are also strongly dependent on the opal quality, which is a direct consequence of the monodispersity of colloids used for their growth. In order to probe the quality of the opals, a characterization of the opal by incidence-angle-dependent transmittance spectroscopy for both P (parallel to plane of incidence) and S (perpendicular to the plane of incidence) polarization was performed. The advantage of the angular-dependent measurements is to clearly show the dispersive and polarized optical properties of the opals. In order to show these effects, in Figure 14 the transmittance spectra recorded at different incidence angles (from 0 to 54°) are reported for the OMDM1 opal for S (a) and P (b) polarization and with vertical orientation of the sample (vertical means that the direction of meniscus displacement during the growth is vertical with respect to the lab floor).

The stop band at $\theta = 0^\circ$ is observed as a minimum at about 625 nm, which shifts towards lower wavelengths upon increasing θ . Upon fitting these data with (1) and by assuming that the interplanar spacing is determined only by the sphere diameter, a value of $n_{\text{eff}} = 1.32$ is obtained [36].

At about 350 nm, an additional structure having an opposite dispersion is instead observed, merging at about 40° with that of the main stop band and then crossing it. Additional structures, almost dispersiveless, are also observed below 400 nm. These complicate dispersive structures are strongly dependent on light polarization (more evident for P polarization) but are not characteristic of the nanosphere material since already observed for both polystyrene [56] and silica opals [60]. Finally, we notice that the full width at half maximum (FWHM) of the stop band becomes slightly anisotropic upon increasing the incidence angle. All these

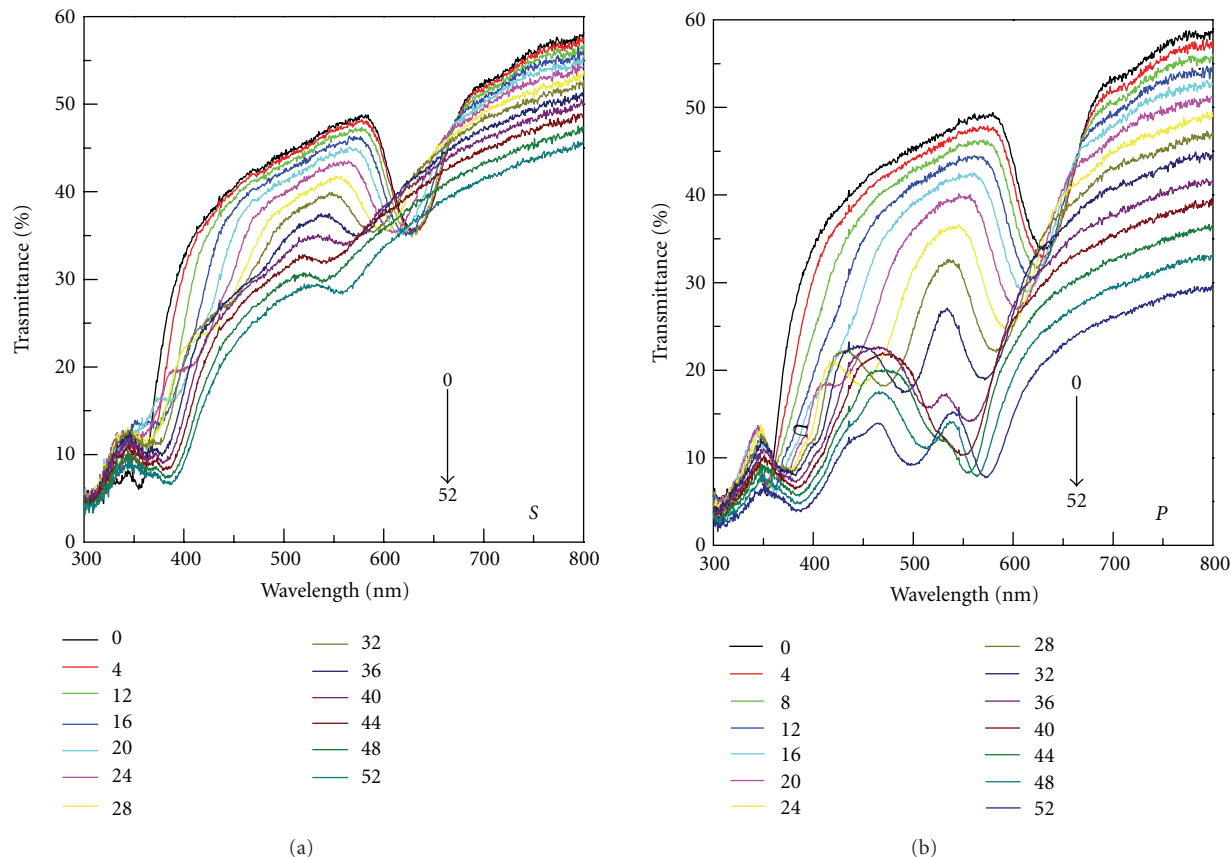


FIGURE 14: Transmittance spectra of OMDM1 opal as a function of the incidence angle from 0 to 52° for S (a) and P (b) polarized light [36].

features are in full agreement with theoretical calculations [56, 60] thus demonstrating the high optical quality of these opals and, as a consequence, of polymer nanospheres [36].

4. Conclusion

Polytetrafluoroethylene (PTFE) latexes with particles in the submicrometer size range can be successfully employed as seeds in the emulsifier-free emulsion polymerization of various monomers including styrene, acrylic mixture, or methyl methacrylate or thus leading to a wide variety of core-shell nanosphere architectures. The seeded surfactant-free emulsion polymerization technique reveals an efficient process to prepare monodisperse latexes because the final number of particles was nearly the same as the initial number of seed particles thus allowing the final particle size to be precisely controlled leading to the target particle size with excellent reproducibility. In addition, a self sharpening of the size distribution was also observed with increasing the monomer to seed ratio. As a consequence of the high PTFE compartmentalization, a fractionated crystallization behaviour was observed in which the only PTFE crystallization process occurs at very high undercooling, possibly deriving from the homogeneous nucleation mechanism.

These core-shell particles can be employed as very efficient additives able to provide blends featuring a perfect dispersion of PTFE particles provided that the shell is

constituted by the same polymeric material with which the polymer matrix is made up. In addition, due to the excellent control over the particle size and distribution, these nanoparticles are excellent building blocks for colloidal crystals and other nanostructured materials. In particular, 2D colloidal crystal of spheres leads to the smallest 2D nanostructuring for the preparation of masks with a combination of nanosphere lithography and reactive ion etching. 3D colloidal crystals were also obtained featuring excellent opal quality, which is a direct consequence of the monodispersity of colloids used for their growth.

Acknowledgment

Part of this work has been performed at NanoFacility Piemonte, INRiM, a laboratory supported by Compagnia di San Paolo.

References

- [1] E. Giannetti and M. Visca, "Process for the polymerization in aqueous dispersion of fluorinated monomers," US Patent, 4864006, 1987.
- [2] V. Kapeliouchko, E. Marchese, and P. Colaianna, "TFE polymerization process," EU Patent, 969027.
- [3] G. Gozzi, "Halogenated butyl rubber," US Patent, 4632963, 1987.

- [4] M. Albano, M. Apostolo, V. Arcella, and E. Marchese, "Fluoroelastomer compositions," US Patent, 6395834, 2002.
- [5] A. E. Feiring, J. F. Imbalzano, and D. L. Kerbow, "Advances in fluoroplastics," *Plastics Engineering*, vol. 27, 1994.
- [6] J. Scheirs, *Modern Fluoropolymers*, John Wiley & Sons, New York, NY, USA, 1997.
- [7] B. Zhao, W. J. Brittain, and E. A. Vogler, "Trichlorosilane chemisorption on surface-modified poly(tetrafluoroethylene)," *Macromolecules*, vol. 32, no. 3, pp. 796–800, 1999.
- [8] L. Y. Ji, E. T. Kang, K. G. Neoh, and K. L. Tan, "Oxidative graft polymerization of aniline on PTFE films modified by surface hydroxylation and silanization," *Langmuir*, vol. 18, no. 23, pp. 9035–9040, 2002.
- [9] E. Akinay and T. Tincer, "Radiation grafting of vinyl monomers onto poly(tetrafluoroethylene) powder produced by γ irradiation and properties of grafted poly(tetrafluoroethylene) filled low density polyethylene," *Journal of Applied Polymer Science*, vol. 79, no. 5, pp. 816–826, 2001.
- [10] U. König, M. Nitschke, A. Menning et al., "Durable surface modification of poly(tetrafluoroethylene) by low pressure H_2O plasma treatment followed by acrylic acid graft polymerization," *Colloids and Surfaces B*, vol. 24, no. 1, pp. 63–71, 2002.
- [11] L. Häußler, G. Pompe, D. Lehmann, and U. Lappan, "Fractionated crystallization in blends of functionalized poly(tetrafluoroethylene) and polyamide," *Macromolecular Symposia*, vol. 164, no. 1, pp. 411–419, 2001.
- [12] G. Pompe, L. Häußler, P. Pötschke et al., "Reactive polytetrafluoroethylene/polyamide compounds. I. Characterization of the compound morphology with respect to the functionality of the polytetrafluoroethylene component by microscopic and differential scanning calorimetry studies," *Journal of Applied Polymer Science*, vol. 98, no. 3, pp. 1308–1316, 2005.
- [13] G. Pompe, L. Häußler, G. Adam et al., "Reactive polytetrafluoroethylene/polyamide 6 compounds. II. Study of the reactivity with respect to the functionality of the polytetrafluoroethylene component and analysis of the notched impact strength of the polytetrafluoroethylene/polyamide 6 compounds," *Journal of Applied Polymer Science*, vol. 98, no. 3, pp. 1317–1324, 2005.
- [14] M. Okaniwa, "Synthesis of poly(tetrafluoroethylene)/poly(butadiene) core-shell particles and their graft copolymerization," *Journal of Applied Polymer Science*, vol. 68, no. 2, pp. 185–190, 1998.
- [15] J. Othegraven, R. Piazza, and E. Bartsch, "Synthesis and characterization of core-shell colloids with fluorocarbon cores," *Macromolecular Symposia*, vol. 151, no. 1, pp. 515–520, 2000.
- [16] X. Cui, S. Zhong, H. Zhang, Q. Gu, J. Li, and H. Wang, "Preparation and characterization of polytetrafluoroethylene-polyacrylate core-shell nanoparticles," *Polymers for Advanced Technologies*, vol. 18, no. 7, pp. 544–548, 2007.
- [17] K. I. Suresh, T. Pakula, and E. Bartsch, "Synthesis morphology and rheological behavior of fluoropolymer-polyacrylate nanocomposites," *Macromolecular Reaction Engineering*, vol. 1, no. 2, pp. 253–262, 2007.
- [18] R. Arshady, "Suspension, emulsion, and dispersion polymerization: a methodological survey," *Colloid & Polymer Science*, vol. 270, no. 8, pp. 717–732, 1992.
- [19] C. S. Chern, *Principles and Applications of Emulsion Polymerization*, John Wiley & Sons, New York, NY, USA, 2008.
- [20] Y. Xia, B. Gates, Y. Yin, and Y. Lu, "Monodispersed colloidal spheres: old materials with new applications," *Advanced Materials*, vol. 12, no. 10, pp. 693–713, 2000.
- [21] O. Kalinina and E. Kumacheva, "Polymeric nanocomposite material with a periodic structure," *Chemistry of Materials*, vol. 13, no. 1, pp. 35–38, 2001.
- [22] C. Paquet and E. Kumacheva, "Nanostructured polymers for photonics," *Materials Today*, vol. 11, no. 4, pp. 48–56, 2008.
- [23] U. Jeong, Y. Wang, M. Ibisate, and Y. Xia, "Some new developments in the synthesis, functionalization, and utilization of monodisperse colloidal spheres," *Advanced Functional Materials*, vol. 15, no. 12, pp. 1907–1921, 2005.
- [24] J. C. Hulthen and R. P. Van Duyne, "Nanosphere lithography: a materials general fabrication process for periodic particle array surfaces," *Journal of Vacuum Science and Technology A*, vol. 13, no. 3, pp. 1553–1558, 1995.
- [25] K. Inoue and K. Kazuo, *Photonic Crystals Physics, Fabrication and Applications*, vol. 94 of *Ohtaka editor Springer Series in Optical Sciences*, Springer, Berlin, Germany, 2004.
- [26] C. S. Chern, "Emulsion polymerization mechanisms and kinetics," *Progress in Polymer Science*, vol. 31, no. 5, pp. 443–486, 2006.
- [27] J. W. Goodwin, J. Hearn, C. C. Ho, and R. H. Ottewill, "Studies on the preparation and characterisation of monodisperse polystyrene latices - III. Preparation without added surface active agents," *Colloid and Polymer Science Kolloid Zeitschrift & Zeitschrift für Polymere*, vol. 252, no. 6, pp. 464–471, 1974.
- [28] J. W. Goodwin, H. R. Ottewill, R. Pelton, G. Vianello, and D. E. Yates, "Control of particle size in the formation of polymer lattices," *British Polymer Journal*, vol. 10, no. 3, pp. 173–180, 1978.
- [29] M. Egen and R. Zentel, "Surfactant-free emulsion polymerization of various methacrylates: towards monodisperse colloids for polymer opals," *Macromolecular Chemistry and Physics*, vol. 205, no. 11, pp. 1479–1488, 2004.
- [30] B. Lange, N. Metz, M. N. Tahir et al., "Functional polymer-opals from core-shell colloids," *Macromolecular Rapid Communications*, vol. 28, no. 20, pp. 1987–1994, 2007.
- [31] E. Giani, K. Sparnacci, M. Laus, G. Palamone, V. Kapeliouchko, and V. Arcella, "PTFE-polystyrene core-shell nanospheres and nanocomposites," *Macromolecules*, vol. 36, no. 12, pp. 4360–4367, 2003.
- [32] K. Sparnacci, D. Antonioli, S. Deregibus et al., "Two-dimensional non-close-packed arrays of nanoparticles via core-shell nanospheres and reactive ion etching," *Polymers for Advanced Technologies*. In press.
- [33] K. Sparnacci, D. Antonioli, S. Deregibus et al., "PTFE-based core-soft shell nanospheres and soft matrix nanocomposites," *Macromolecules*, vol. 42, no. 10, pp. 3518–3524, 2009.
- [34] V. Kapeliouchko, G. Palamone, T. Poggio et al., "PMMA-based core-shell nanoparticles with various PTFE cores," *Journal of Polymer Science A*, vol. 47, no. 11, pp. 2928–2937, 2009.
- [35] D. Antonioli, S. Deregibus, K. Sparnacci et al., "Fine tuning of the size of PTFE-PMMA core-shell nanospheres," *Polymers for Advanced Technologies*, vol. 23, no. 3, pp. 558–564, 2012.
- [36] D. Antonioli, S. Deregibus, G. Panzarasa et al., "PTFE-PMMA core-shell nanoparticles as building blocks for self-assembled opals: synthesis, properties and optical response," *Polymer International*. In press.
- [37] J. Rybczynski, U. Ebels, and M. Giersig, "Large-scale, 2D arrays of magnetic nanoparticles," *Colloids and Surfaces A*, vol. 219, pp. 1–6, 2003.
- [38] A. Kosiorok, W. Kandulski, H. Glaczynska, and M. Giersig, "Fabrication of nanoscale rings, dots, and rods by combining shadow nanosphere lithography and annealed polystyrene nanosphere masks," *Small*, vol. 1, no. 4, pp. 439–444, 2005.
- [39] S. M. Weekes, F. Y. Ogrin, W. A. Murray, and P. S. Keatley, "Macroscopic arrays of magnetic nanostructures from self-assembled nanosphere templates," *Langmuir*, vol. 23, no. 3, pp. 1057–1060, 2007.

- [40] P. Jiang, J. F. Bertone, and V. L. Colvin, "A lost-wax approach to monodisperse colloids and their crystals," *Science*, vol. 291, no. 5503, pp. 453–457, 2001.
- [41] L. Berti, M. Cucini, F. Di Stasio et al., "Spectroscopic investigation of artificial opals infiltrated with a heteroaromatic quadrupolar dye," *Journal of Physical Chemistry C*, vol. 114, no. 6, pp. 2403–2413, 2010.
- [42] S. M. Heard, F. Grieser, C. G. Barraclough, and J. V. Sanders, "The characterization of ag sols by electron microscopy, optical absorption, and electrophoresis," *Journal of Colloid And Interface Science*, vol. 93, no. 2, pp. 545–555, 1983.
- [43] S. Jiang, E. D. Sudol, V. L. Dimonie, and M. S. El-Aasser, "Seeding as a means of controlling particle size in dispersion polymerization," *Journal of Applied Polymer Science*, vol. 108, no. 6, pp. 4096–4107, 2008.
- [44] X. Q. Wang, D. R. Chen, J. C. Han, and S. Y. Du, "Crystallization behavior of polytetrafluoroethylene (PTFE)," *Journal of Applied Polymer Science*, vol. 83, no. 5, pp. 990–996, 2002.
- [45] M. Laus, K. Sparnacci, D. Antonioli et al., "On the multiple crystallization behavior of PTFE in PMMA/PTFE nanocomposites from core-shell nanoparticles," *Journal of Polymer Science B*, vol. 48, no. 5, pp. 548–554, 2010.
- [46] J. A. Koutsky, A. G. Walton, and E. Baer, "Nucleation of polymer droplets," *Journal of Applied Physics*, vol. 38, no. 4, pp. 1832–1839, 1967.
- [47] V. Everaert, G. Groeninckx, and L. Aerts, "Fractionated crystallization in immiscible POM/(PS/PPE) blends part 1: effect of blend phase morphology and physical state of the amorphous matrix phase," *Polymer*, vol. 41, no. 4, pp. 1409–1428, 2000.
- [48] V. Balsamo and L. M. Gouveia, "Interplay of fractionated crystallization and morphology in polypropylene/poly(ϵ -caprolactone) blends," *Journal of Polymer Science B*, vol. 45, no. 11, pp. 1365–1379, 2007.
- [49] H. L. Chen, J. C. Wu, T. L. Lin, and J. S. Lin, "Crystallization kinetics in microphase-separated poly(ethylene oxide)-block-poly(1, 4-butadiene)," *Macromolecules*, vol. 34, no. 20, pp. 6936–6944, 2001.
- [50] J. Pavlinec, M. Lazar, and K. Csomorova, "Thermal degradation of multilayer methacrylate-acrylate particle-bead polymer powders and melts," *Polymer Degradation and Stability*, vol. 55, no. 1, pp. 65–71, 1997.
- [51] B. J. Holland and J. N. Hay, "The kinetics and mechanisms of the thermal degradation of poly(methyl methacrylate) studied by thermal analysis-Fourier transform infrared spectroscopy," *Polymer*, vol. 42, no. 11, pp. 4825–4835, 2001.
- [52] D. Antonioli, M. Laus, K. Sparnacci et al., "Thermal and DMA characterization of PTFE-PMMA nanocomposites from core-shell nanoparticles," *Macromolecular Symposia*, vol. 296, no. 1, pp. 197–202, 2010.
- [53] Y. J. Zhang, W. Li, and K. J. Chen, "Application of two-dimensional polystyrene arrays in the fabrication of ordered silicon pillars," *Journal of Alloys and Compounds*, vol. 450, no. 1-2, pp. 512–516, 2008.
- [54] J. D. Joannopoulos, R. D. Meade, and J. N. Win, *Photonic Crystals: Molding the Flow of the Light*, Princeton University Press, Princeton, NJ, USA, 1995.
- [55] V. Morandi, F. Marabelli, V. Amendola, M. Meneghetti, and D. Comoretto, "Colloidal photonic crystals doped with gold nanoparticles: spectroscopy and optical switching properties," *Advanced Functional Materials*, vol. 17, no. 15, pp. 2779–2786, 2007.
- [56] E. Pavarini, L. C. Andreani, C. Soci, M. Galli, F. Marabelli, and D. Comoretto, "Band structure and optical properties of opal photonic crystals," *Physical Review B*, vol. 72, no. 4, pp. 1–10, 2005.
- [57] L. C. Andreani, A. Balestreri, J. F. Galisteo-López et al., "Optical response with three-fold symmetry axis on oriented microdomains of opal photonic crystals," *Physical Review B*, vol. 78, no. 20, pp. 205304–205311, 2008.
- [58] J. F. Galisteo-Lopez, F. Lopez-Tejiera, S. Rubio, C. Lopez, and J. Sanchez-Dehesa, "Experimental evidence of polarization dependence in the optical response of opal-based photonic crystals," *Applied Physics Letters*, vol. 82, no. 23, pp. 4068–4070, 2003.
- [59] F. Lopez-Tejiera, T. Ochiai, K. Sakoda, and J. Sanchez-Dehesa, "Symmetry characterization of eigenstates in opal-based photonic crystals," *Physical Review B*, vol. 65, no. 19, pp. 195110–195118, 2002.
- [60] D. Comoretto, D. Cavallo, G. Dellepiane et al., "Optical studies of artificial opals as 3D photonic crystals," *Material Research Society Symposium Proceeding*, vol. 708, no. 1, pp. 1–6, 2002.

Research Article

Preparation of a Novel Nanocomposite of Polyaniline Core Decorated with Anatase-TiO₂ Nanoparticles in Ionic Liquid/Water Microemulsion

Yanni Guo,^{1,2} Deliang He,¹ Sanbao Xia,¹ Xin Xie,¹ Xiang Gao,¹ and Quan Zhang³

¹ College of Chemistry and Chemical Engineering, Hunan University, Changsha 410082, China

² Department of Petrochemical Engineering, Hunan Petrochemical Vocational Technology College, Yueyang 414012, China

³ College of Civil Engineering, Hunan University, Changsha 410082, China

Correspondence should be addressed to Deliang He, delianghe@163.com

Received 6 June 2011; Accepted 6 September 2011

Academic Editor: Sherine Obare

Copyright © 2012 Yanni Guo et al. This is an open access article distributed under the Creative Commons Attribution License, which permits unrestricted use, distribution, and reproduction in any medium, provided the original work is properly cited.

Polyaniline core decorated with TiO₂ (PANI-TiO₂) nanocomposite particles was successfully synthesized in ionic liquid/water (IL/water) microemulsion in the presence of anatase TiO₂ nanoparticles. The TiO₂ nanoparticles had been dispersed beforehand in OP-10 and *n*-butanol to weaken the strong particles agglomeration of TiO₂. The PANI-TiO₂ nanocomposites were characterized by fourier transform infrared spectroscopy (FTIR), ultraviolet visible spectroscopy (UV-Vis), scanning electron microscopy (SEM), and transmission electron microscope (TEM), and their electrochemical behavior was estimated by the electrochemical workstation. SEM micrographs showed that the nanocomposites exhibited spherical morphology with particle sizes about 70 nm. The TEM result showed that the PANI-TiO₂ nanocomposites had a novel structure and that nanocrystalline TiO₂ deposited onto the surface of PANI, which was different from the reported structure of TiO₂-PANI nanocomposites. Both FTIR and UV-Vis spectra indicate that polyaniline and nano-TiO₂ particles are not simply blended or mixed up. A possible reaction mechanism for this nanocomposite preparation is suggested and analyzed.

1. Introduction

Organic-inorganic nanocomposites for synergetic behavior and a wide range of potential use have triggered great interest and concern of the related academic organizations and researchers over the past decade [1–4]. Specifically, core-shell structures nanocomposites of organic conjugated polymers and inorganic nanocrystals have attracted great attention due to a large number of potential applications such as photonics, photoelectronics, and catalysis [5]. Among the conducting polymers, conducting polyaniline (PANI) is often used as an organic part to prepare nanocomposites because of its low cost, easy preparation, controllable unique properties by oxidation and protonation state, excellent environmental stability, and potential application in electronic devices [6]. A number of different metal oxide particles have so far been encapsulated into the shell of polyaniline giving rise to a host of nanocomposites. Du et al. [7] reported an Ag-PANI

core-shell structure via one-pot redox reaction in ethanol at 250°C. The obtained Ag-PANI core-shell particles are with a large Ag core of the size of about 200 nm and relative thin polyaniline shell of the thickness of about 50 nm. Lei [8] successfully prepared Au-polyaniline nanocomposites with core-shell structure on ITO conducting electrode based on 4-aminothiophenol-capped Au nanoparticles via electrochemical synthesis, and the Au nanoparticle with a mean diameter of ca. 250 nm is the core of the nanocomposite and the polyaniline is the shell wrap of the Au nanoparticle. The CeO₂-polyaniline (CeO₂-PANI) core-shell nanocomposites prepared via chemical oxidation of aniline by CeO₂ were reported by Chuang and Yang [9]. Jing et al. [10] successfully synthesized Ag-polyaniline core-shell nanocomposites via in situ chemical oxidation polymerization of aniline based on mercaptocarboxylic-acid-capped Ag nanoparticle colloid. Yu et al. [11] prepared carbon nanotube-polyaniline core-shell nanowires by in situ inverse microemulsion. Nanocompos-

ites of “egg-like” cores and shell ranging in diameter from 40 to 80 nm and 60 to 120 nm, respectively, have been prepared successfully using hexadecyl trimethyl ammoniumbromide (CTAB) microemulsion by Asim et al. [12]. Nanosized titania, because of its unique physicochemical properties [13–16], is frequently combined with polyaniline. Zhang et al. [17] synthesized PANI-TiO₂ composite microspheres with an average diameter 2.5–3.5 μm by a template-free method in the presence of salicylic acid as dopant. The PANI-TiO₂ composites are typical core-shell structure, PANI-coated crystalline TiO₂. A polyaniline-nano-TiO₂ composite [18] was prepared by polyaniline for the surface modification of nano-TiO₂ particles, forming a core-shell structure.

There are many researches on the core/shell-metal oxide/polyaniline structures, but the structures of polyaniline core decorated with metal oxide are seldom investigated. As is known, the octahedrite-type TiO₂ has better chemical properties and photon characteristics, due to its good absorbability and lower electron/holes recombining rate [19]. The ultraviolet excitation (wavelength <380 nm) can overcome the energy gap of pristine titanium dioxide for photocatalysts for electrons to jump to conduction band to form the electron-hole pair. The formed holes and electrons can oxidize and reduce the H₂O, OH⁻, or O₂ adsorbed on the surface of TiO₂ to living free radicals, which can deteriorate the organic materials or undesired pollutants that adsorbed on the surface of TiO₂ catalyst resulting in generating nonpoisonous CO₂, H₂O, and some inorganic products. However, for TiO₂ core-PANI shell composites, because of package action of polyaniline, photon absorption of TiO₂ nanoparticles is blocked and the living free radicals generated from holes and electrons are hard to transfer onto the surface of polyaniline to oxidize organic materials; moreover, the living free radicals may react to the polyaniline in course of transfer. Thus, in fact, the photoelectric capabilities of TiO₂ are bated after being enwrapped by polyaniline. Hereby, polyaniline core decorated with TiO₂ (PANI-TiO₂) nanocomposite particles makes it possible to develop the properties of TiO₂.

Ionic liquids (ILs) are organic salts with low melting points [20] and have a stable liquid range temperature of over 300°C. Typical ILs have unusual properties including nonvolatility, nonflammability, wide electrochemical windows, higher ionic conductivity, and excellent thermal and chemical stability. More recently, synthesis of PANI has been advocated by electrochemical [21] and interfacial [22] polymerization in ILs. All of the PANIs exhibit excellent physical and chemical properties. Another potential advantage of synthesis in ILs is their unique solvent capabilities, which can avoid organic solvent volatilizing.

Microemulsions are thermodynamically stable dispersions of two or more immiscible liquids that are stabilized by an adsorbed surfactant film at the liquid-liquid interface. They are an effective method to prepare nanoparticles, nanowires, and nanorods [23]. Furthermore, it has been demonstrated that ILs could substitute water or conventional organic solvents to form novel microemulsion systems in the presence of surfactant, and these novel microemulsions

incorporate the advantages of ILs and microemulsion [24–26]. Our research group has successfully prepared PANI nanoparticles in IL/water emulsion systems [27, 28].

In the present study, a polyaniline core decorated with TiO₂ (PANI-TiO₂) nanocomposite was prepared in a microemulsion comprised of deionized water as the continuous aqueous phase and an oil solution including aniline and hydrophobic IL 1-butyl-3-methylimidazolium hexafluorophosphate ([bmim]PF₆) as the dispersed phase in the presence of anatase TiO₂ nanoparticles. The TiO₂ nanoparticles were dispersed beforehand in OP-10 and *n*-butanol. The nanocomposites were characterized by fourier transform infrared spectroscopy (FTIR), ultraviolet visible spectroscopy (UV-Vis), scanning electron microscopy (SEM), and transmission electron microscope (TEM). Moreover, the possible reaction mechanism for the preparation of PANI-TiO₂ nanocomposite is investigated here.

2. Experimental

2.1. Materials. IL 1-butyl-3-methylimidazolium hexafluorophosphate ([bmim]PF₆) was prepared as described in the literature [29]. Nanocrystalline TiO₂ (anatase <10 nm) was synthesized based on a sol-gel technique as described in the previous procedure [30]. Aniline, *n*-butanol, ammonium persulfate (APS), nitric acid, and other chemicals were analytical grade (Sinopharm Chemical Reagent Co., Ltd) and were used as received. The emulsifier nonylphenol ethoxylates (OP-10) was obtained from 3W Industry Co., Ltd. All aqueous solutions were prepared with deionized water.

2.2. Synthesis of Polyaniline Core Decorated with TiO₂ (PANI-TiO₂) Nanocomposite. The polyaniline core decorated with TiO₂ (PANI-TiO₂) composites was synthesized in microemulsion system via in situ chemical oxidative polymerization in the presence of TiO₂ nanoparticles, and the procedure was as follows: Firstly, hydrophobic IL [bmim]PF₆ (2 mL)/aniline (1 mL) mixture was added into the OP-10 (13 mL)/*n*-butanol (3 mL)/HNO₃ (0.115 mol·L⁻¹) solution; after the mixture was stirred for 1 h under magnetic stirring, a dispersion of TiO₂ nanoparticles (TiO₂: aniline = 25 wt%) in a mixed solution of 3 mL OP-10 and 2 mL *n*-butanol was in one time introduced into the mixture; after another 1 h of magnetic stirring, a transparent oil-in-water microemulsion was obtained. Then, the polymerization was initiated by adding 6 mL of 3 mol·L⁻¹ APS aqueous solution into the above microemulsion droplet within 30 min under magnetic stirring. The polymerization was allowed to proceed for 4 h under stirring. Finally, the obtained sap-green polyaniline core decorated with TiO₂ (PANI-TiO₂) nanocomposite powder was filtrated and rinsed with acetone and water repeatedly and then dried in vacuum at 55°C for 24 h. For comparison, polyaniline nanoparticles were also prepared under the same condition, but without TiO₂ nanoparticles added.

All the experimental procedures proceeded at room temperature except the drying of samples.

2.3. Characterization. The morphology of nanocomposites was examined by a JSM-6700F scanning electron microscope (SEM) and a JEM-3010 high-resolution transmission electron microscope (TEM). Fourier transform infrared (FT-IR) spectra were recorded on a Perkin Elmer Fourier transform infrared spectrometer. The ultraviolet visible (UV-vis) absorption spectra were recorded on a LabTech UV-240 spectrophotometer. Cyclic voltammetric studies of PANI and nanocomposites were performed by using an Iviumstat electrochemical working station (Ivium Technologies BV). A one-compartment cell was used with a platinum mesh as counter electrode and a saturated calomel electrode (SCE) as reference electrode. The electrolyte was composed of $1 \text{ mM} \cdot \text{L}^{-1} \text{ K}_3\text{Fe}(\text{CN})_6$, $1 \text{ mM} \cdot \text{L}^{-1} \text{ K}_4\text{Fe}(\text{CN})_6$ and $0.2 \text{ mol} \cdot \text{L}^{-1} \text{ NaCl}$. The scan speed was $0.1 \text{ V} \cdot \text{s}^{-1}$, and the potential range was from -200 mV to 600 mV . A certain volume of PANI or nanocomposite ethanol solution was added dropwise by an injector to the surface of graphite disk (0.7 cm^2). After having been dried in air at room temperature, the PANI/graphite or nanocomposite/graphite electrode was used as the working electrode.

3. Results and Discussion

3.1. A Possible Reaction Mechanism for PANI-TiO₂ Nanocomposite. Figure 1 shows a supposed model describing a polyaniline core decorated with TiO₂ (PANI-TiO₂) nanocomposite formation via microemulsion polymerization. There are plenty of surface hydroxyl groups on the surface of TiO₂ nanoparticles, which are produced from the adsorbed water molecules on the surface of TiO₂ nanoparticles. The hydrogen bonding interactions between the surface hydroxyl groups and the ether groups in OP-10 or the hydroxyl groups in *n*-butanol make it possible to weaken the strong particles agglomeration of TiO₂ and thus to form a dispersion of TiO₂ nanoparticles. When the above dispersion is added into the (IL+An)/water microemulsion, under the traction of lipophilic groups of OP-10 and *n*-butanol, the dispersed TiO₂ nanoparticles adsorb onto the surface of the microemulsion micelles to form core-shell-type nanomicelles. Afterwards, the polymerization is initiated by APS, during which some chemical bonds generate between TiO₂ and polyaniline chain which are stronger than the hydrogen bonds between the surface of TiO₂ and hydrophilic groups of OP-10 or *n*-butanol. After the polymerization ends, OP-10, *n*-butanol and IL can be washed down; finally, the polyaniline core decorated with TiO₂ nanocomposite are prepared.

3.2. FTIR and UV-Vis Spectra of PANI-TiO₂ Nanocomposites. The FTIR spectra of anatase TiO₂ nanoparticles, PANI, and PANI-TiO₂ nanocomposite are shown in Figure 2, respectively. From Figure 2(a), the broad peak from 400 to 700 cm^{-1} is the characteristic band of TiO₂. The characteristic bands of PANI (Figure 2(b)) are assigned as follows: the band at 3413 cm^{-1} is attributable to N-H stretching mode; C=N and C=C stretching modes for the quinoid and benzenoid rings occur at 1585 cm^{-1} and 1504 cm^{-1} ; the bands at about 1288 cm^{-1} and 1244 cm^{-1} have been attributed to C-

N stretching mode for the benzenoid ring, while the band at 1101 cm^{-1} is assigned to an in-plane bending vibration of C-H (mode of N=Q=N, Q=N⁺H=B and B-N⁺H-B), which is formed during protonation [31]. It is evident that the FTIR spectrum of the PANI-TiO₂ composite shown in Figure 2(c) contains contributions from both anatase TiO₂ and PANI. However, some bands of PANI have shifted due to interactions with anatase TiO₂ nanoparticles. For example, the bands at 1585 cm^{-1} , 1504 cm^{-1} , and 1288 cm^{-1} , corresponding to the stretching mode of C=N, C=C, and C-N, all shift to lower wavenumbers, and N-H stretching band at 3413 cm^{-1} shifts to higher wavenumber. Similarly, the band at 1101 cm^{-1} also shifts to 1120 cm^{-1} . These changes suggest that C=N, C=C and C-N bands become weaker in PANI-TiO₂ nanocomposite, while the N-H band becomes stronger. This is probably because of the action of hydrogen bonding between the surfaces of anatase TiO₂ nanoparticles and the N-H groups in PANI macromolecules. The results confirm that there is strong interaction between the PANI and nanocrystalline TiO₂, and the presence of anatase TiO₂ nanoparticles prompts the doping of PANI.

The UV-Vis absorption spectra of anatase TiO₂, PANI and the PANI-TiO₂ composite are shown in Figure 3. Clearly, the resulting PANI-TiO₂ composite can strongly absorb not only the near ultraviolet light but also the visible light, whereas the TiO₂ can absorb light with wavelengths below 250 nm only. As shown in Figure 3, we can clearly observe the characteristic bands of polyaniline at 366–373 nm and 535 nm, which are attributed to π - π^* transition of benzenoid ring, polaron- π^* , respectively [32]. Specifically, the absorption peaks of the PANI-TiO₂ nanocomposite at characteristic peaks of PANI become stronger; moreover, the characteristic absorption peak at 535 nm becomes un conspicuous because of being covered by a new absorption peak at 680 nm in visible region. This result further proves that it is not a simple mixing action between the PANI and nanocrystalline TiO₂, and the resulting PANI-TiO₂ nanocomposite could have a potential use as photocatalysis material.

3.3. Electrochemical Characteristics of PANI-TiO₂ Nanocomposite. The electrochemical characteristics of different samples were also investigated in relevant electrolyte. Cyclic voltammograms (CVs) of PANI and PANI-TiO₂ nanocomposite are shown in Figure 4. The reversible CV curves are observed obviously, which is related to the electrochemical probe of $\text{Fe}(\text{CN})_6^{4-}/\text{Fe}(\text{CN})_6^{3-}$. Although both shapes seem to be similar to each other, the oxidation and reduction peak current density ($3.13 \text{ mA} \cdot \text{cm}^{-2}$, $-3.45 \text{ mA} \cdot \text{cm}^{-2}$) of the PANI-TiO₂ nanocomposite are higher than those of the PANI ($2.30 \text{ mA} \cdot \text{cm}^{-2}$, $-2.70 \text{ mA} \cdot \text{cm}^{-2}$). The better electrochemical catalytic activity of the PANI-TiO₂ nanocomposite should be attributed to its special structure. When TiO₂ nanoparticles are mixed into the RTIL/water microemulsion under stirring, they assemble at the RTIL/water interface. Moreover, nano-TiO₂ exhibits electropositive properties in the acidic medium. They can attract a lot of anions, namely, nitrate ions, to assemble at the interface of the microemulsion. The anions are doped into the PANI chains

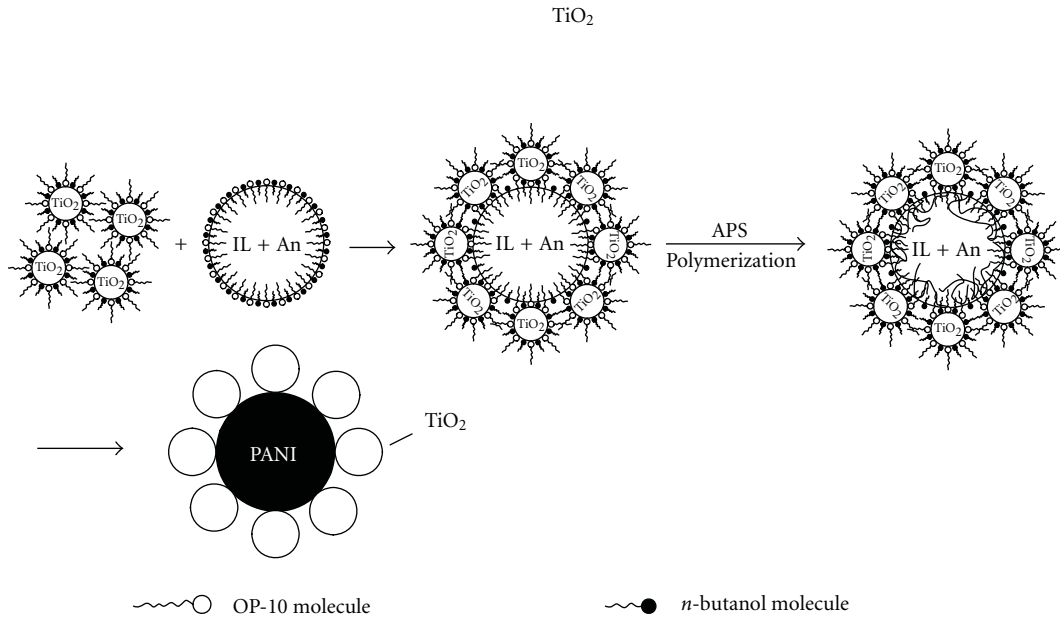


FIGURE 1: The forming mechanism of PANI-TiO₂ nanocomposite.

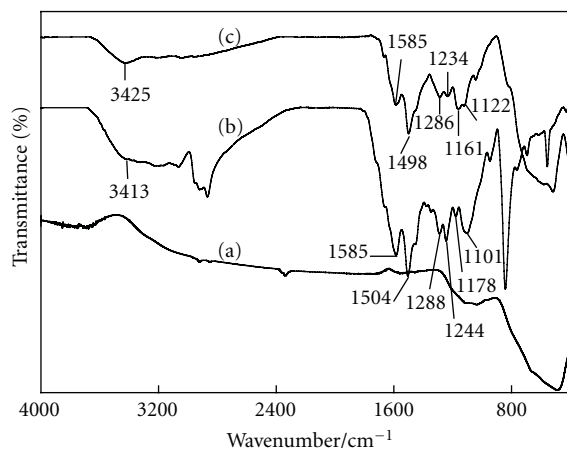


FIGURE 2: FTIR spectra of (a) TiO₂, (b) PANI, and (c) PANI-TiO₂.

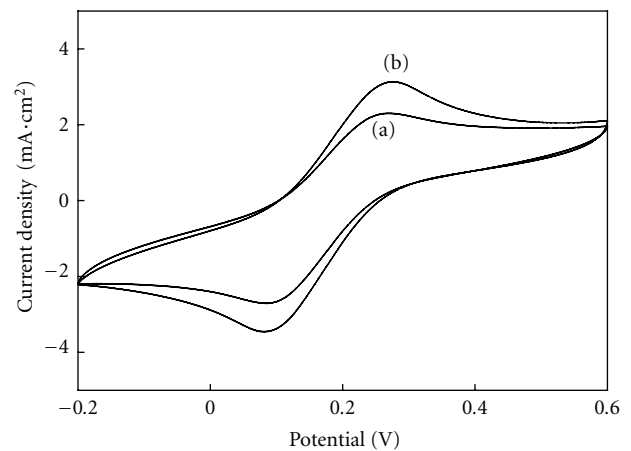


FIGURE 4: Cyclic voltammograms of different samples at a potential scan rate of 50 mV·s⁻¹. (a) PANI, (b) PANI-TiO₂.

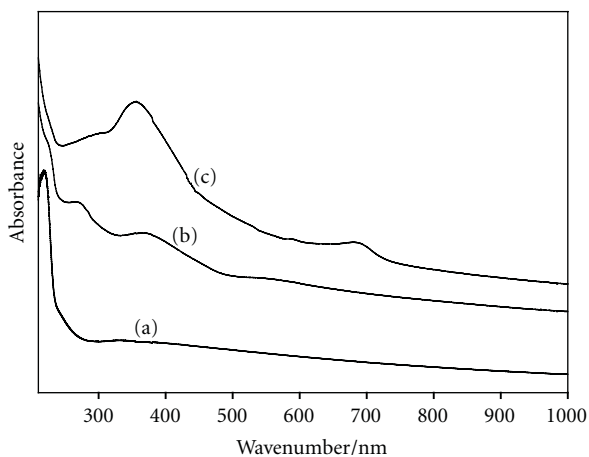
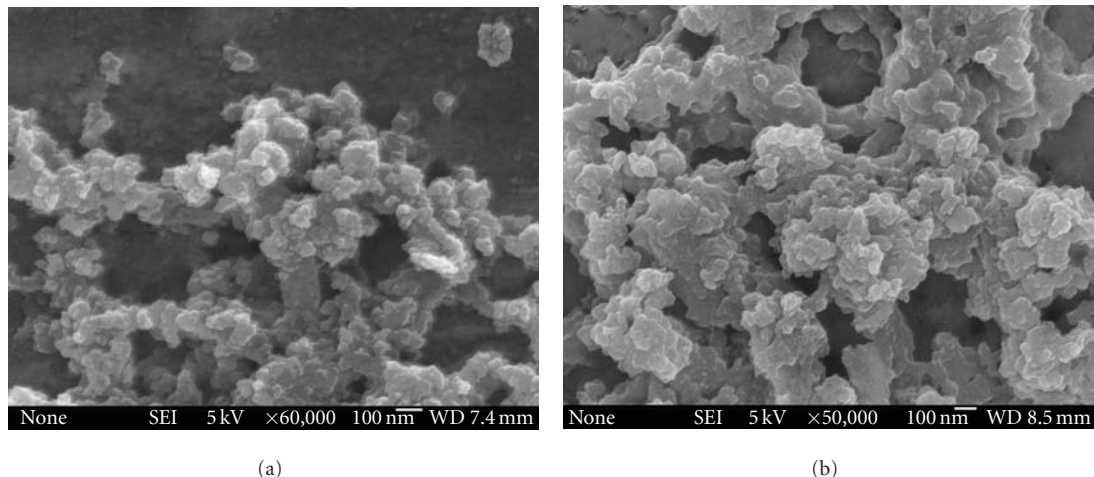


FIGURE 3: UV-Vis spectra of (a) TiO₂, (b) PANI, and (c) PANI-TiO₂.

as counterions when the polymerization is processed. Thus, the doping degree of the PANI-TiO₂ nanocomposite is improved, and a better electrochemical activity is exhibited.

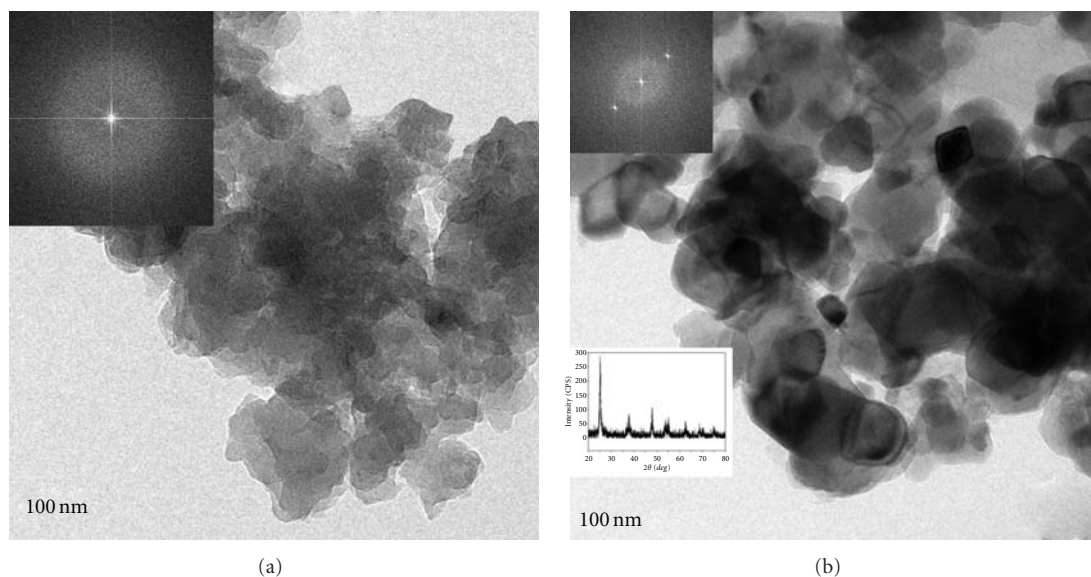
3.4. Morphology of PANI-TiO₂ Nanocomposite. The morphology and particle sizes of PANI and PANI-TiO₂ nanocomposite were determined by SEM and shown in Figure 5. It can be found from Figure 5(a) that the PANIs exhibit spherical morphology with particle sizes of about 50 nm, while after combination with TiO₂ the morphology of PANI-TiO₂ nanoparticles approaches spherical with particle size of about 70 nm (Figure 5(b)). It implies that TiO₂ nanoparticles enwrap the polyaniline.

Figure 6 shows the typical TEM images of PANI and PANI-TiO₂ nanocomposite. It can be found that the



(a)

(b)

FIGURE 5: SEM images of (a) PANI and (b) PANI-TiO₂.

(a)

(b)

FIGURE 6: TEM images of (a) PANI and (b) PANI-TiO₂ (The insets are the selected area electron diffraction patterns and the X-ray diffraction pattern of TiO₂.)

polyaniline is amorphous in Figure 6(a), which has great difference from Figure 6(b). Figure 6(b) gives the TEM image of the polyaniline core decorated with anatase TiO₂ shell nanocomposite. One can find that the polyaniline with a mean diameter of about 50 nm is the core of the nanocomposite and the TiO₂ nanoparticles deposit onto the surface of the polyaniline, which is different from the reported structure of TiO₂-PANI nanoparticles that TiO₂ is wrapped by polyaniline. The diffraction pattern from the edge of particles of PANI-TiO₂ composite in Figure 6(b) suggests that the TiO₂ nanoparticles deposited on the surface of polyaniline are typical anatase phase, and this agrees well with the X-ray diffraction result of the separate TiO₂ nanoparticle sample.

4. Conclusion

Polyaniline core decorated with TiO₂ (PANI-TiO₂) nanocomposite has been successfully prepared in IL/water microemulsion in the presence of nanocrystalline TiO₂ particles. TiO₂ nanoparticles dispersed on the (IL + An)/water interface could deposit uniformly onto the surface of PANI. It is confirmed that the diameter of the resulted PANI-TiO₂ nanoparticles is about 70 nm, and the interactions between two components are strong. FTIR and UV-Vis spectra indicate that polyaniline and nano-TiO₂ particles are not simply blended or mixed up, while the strong interactions which exist at the interface of polyaniline macromolecules and nano-TiO₂ particles need further investigations in the future. CV curves show that the PANI-

TiO₂ nanocomposite has better electrochemical catalytic activity than PANI.

Therefore, it can be expected that PANI-TiO₂ nanocomposite should be useful in photocatalysis and electrical and electrochemical fields. Furthermore, this method is simple and environmentally friendly and has a great potential for the commercialization of the technology.

Acknowledgment

This work is financially supported by the Hunan Provincial Natural Science Foundation of China (no. 11JJ3015, 11JJ1009).

References

- [1] L. Shi, X. Wang, L. Lu, X. Yang, and X. Wu, "Preparation of TiO₂/polyaniline nanocomposite from a lyotropic liquid crystalline solution," *Synthetic Metals*, vol. 159, no. 23-24, pp. 2525–2529, 2009.
- [2] J. Liu, E. N. Kadnikova, Y. Liu, M. D. McGehee, and J. M. J. Fréchet, "Polythiophene containing thermally removable solubilizing groups enhances the interface and the performance of polymer-titania hybrid solar cells," *Journal of the American Chemical Society*, vol. 126, no. 31, pp. 9486–9487, 2004.
- [3] N. Sakai, G. K. Prasad, Y. Ebina, K. Takada, and T. Sasaki, "Layer-by-layer assembled TiO₂ nanoparticle/PEDOT-PSS composite films for switching of electric conductivity in response to ultraviolet and visible light," *Chemistry of Materials*, vol. 18, no. 16, pp. 3596–3598, 2006.
- [4] D. Chowdhury, A. Paul, and A. Chattopadhyay, "Photocatalytic polypyrrole-TiO₂-nanoparticles composite thin film generated at the air-water interface," *Langmuir*, vol. 21, no. 9, pp. 4123–4128, 2005.
- [5] S. Sun, C. B. Murray, D. Weller, L. Folks, and A. Moser, "Monodisperse FePt nanoparticles and ferromagnetic FePt nanocrystal superlattices," *Science*, vol. 287, no. 5460, pp. 1989–1992, 2000.
- [6] J. Huang, S. Virji, B. H. Weiller, and R. B. Kaner, "Polyaniline nanofibers: facile synthesis and chemical sensors," *Journal of the American Chemical Society*, vol. 125, no. 2, pp. 314–315, 2003.
- [7] J. Du, Z. Liu, B. Han, Z. Li, J. Zhang, and Y. Huang, "One-pot synthesis of the macroporous polyaniline microspheres and Ag/polyaniline core-shell particles," *Microporous and Mesoporous Materials*, vol. 84, no. 1–3, pp. 254–260, 2005.
- [8] T. Lei, "Preparation of novel core-shell nanoparticles by electrochemical synthesis," *Transactions of Nonferrous Metals Society of China*, vol. 17, no. 6, pp. 1343–1346, 2007.
- [9] F. Y. Chuang and S. M. Yang, "Cerium dioxide/polyaniline core-shell nanocomposites," *Journal of Colloid and Interface Science*, vol. 320, no. 1, pp. 194–201, 2008.
- [10] S. Y. Jing, S. X. Xing, L. X. Yu, and Y. Wu, "Synthesis and characterization of Ag/polyaniline core-shell nanocomposites based on silver nanoparticles colloid," *Materials Letters*, vol. 61, no. 13, pp. 2794–2797, 2007.
- [11] Y. Yu, B. Che, Z. Si, L. Li, W. Chen, and G. Xue, "Carbon nanotube/polyaniline core-shell nanowires prepared by in situ inverse microemulsion," *Synthetic Metals*, vol. 150, no. 3, pp. 271–277, 2005.
- [12] N. Asim, S. Radiman, and M. A. B. Yarmo, "Preparation and characterization of core-shell polyaniline/V₂O₅ nanocomposite via microemulsion method," *Materials Letters*, vol. 62, no. 6-7, pp. 1044–1047, 2008.
- [13] Z. Yanqing, S. Erwei, C. Zhizhan, L. Wenjun, and H. Xingfang, "Influence of solution concentration on the hydrothermal preparation of titania crystallites," *Journal of Materials Chemistry*, vol. 11, no. 5, pp. 1547–1551, 2001.
- [14] M. Ferroni, V. Guidi, G. Martinelli, G. Faglia, P. Nelli, and G. Sberveglieri, "Characterization of a nanosized TiO₂ gas sensor," *Nanostructured Materials*, vol. 7, no. 7, pp. 709–718, 1996.
- [15] D. M. Blake, J. Webb, C. Turchi, and K. Magrini, "Kinetic and mechanistic overview of TiO₂-photocatalyzed oxidation reactions in aqueous solution," *Solar Energy Materials*, vol. 24, no. 1–4, pp. 584–593, 1991.
- [16] J. Karch, R. Birringer, and H. Gleiter, "Ceramics ductile at low temperature," *Nature*, vol. 330, no. 6148, pp. 556–558, 1987.
- [17] L. Zhang, M. Wan, and Y. Wei, "Polyaniline/TiO₂ microspheres prepared by a template-free method," *Synthetic Metals*, vol. 151, no. 1, pp. 1–5, 2005.
- [18] X. W. Li, G. H. Wang, X. X. Li, and D. M. Lu, "Surface properties of polyaniline/nano-TiO₂ composites," *Applied Surface Science*, vol. 229, no. 1, pp. 395–401, 2004.
- [19] B. Xia, H. Huang, and Y. Xie, "Heat treatment on TiO₂ nanoparticles prepared by vapor-phase hydrolysis," *Materials Science and Engineering B*, vol. 57, no. 2, pp. 150–154, 1999.
- [20] K. R. Seddon, A. Stark, and M. J. Torres, "Influence of chloride, water, and organic solvents on the physical properties of ionic liquids," *Pure and Applied Chemistry*, vol. 72, no. 12, pp. 2275–2287, 2000.
- [21] P. C. Innis, J. Mazurkiewicz, T. Nguyen, G. G. Wallace, and D. MacFarlane, "Enhanced electrochemical stability of polyaniline in ionic liquids," *Current Applied Physics*, vol. 4, no. 2–4, pp. 389–393, 2004.
- [22] H. Gao, T. Jiang, B. Han et al., "Aqueous/ionic liquid interfacial polymerization for preparing polyaniline nanoparticles," *Polymer*, vol. 45, no. 9, pp. 3017–3019, 2004.
- [23] Y. Xing, M. Li, S. A. Davis, and S. Mann, "Synthesis and characterization of cerium phosphate nanowires in microemulsion reaction media," *Journal of Physical Chemistry B*, vol. 110, no. 3, pp. 1111–1113, 2006.
- [24] Y. Gao, S. Han, B. Han et al., "TX-100/water/1-butyl-3-methylimidazolium hexafluorophosphate microemulsions," *Langmuir*, vol. 21, no. 13, pp. 5681–5684, 2005.
- [25] N. Li, Y. Gao, L. Zheng, J. Zhang, L. Yu, and X. Li, "Studies on the micropolarities of bmimBF₄/TX-100/toluene ionic liquid microemulsions and their behaviors characterized by UV-visible spectroscopy," *Langmuir*, vol. 23, no. 3, pp. 1091–1097, 2007.
- [26] C. Fu, H. Zhou, W. Peng, J. Chen, and Y. Kuang, "Comparison of electrodeposition of silver in ionic liquid microemulsions," *Electrochemistry Communications*, vol. 10, no. 5, pp. 806–809, 2008.
- [27] Z. Zhou, D. He, X. Li, X. Li, L. Zhang, and G. Li, "The micro-emulsion synthesis of polyaniline in ionic liquid/water system," *Acta Polymerica Sinica*, no. 8, pp. 757–760, 2007.
- [28] Z. Zhou, D. He, X. Li, S. Wang, and G. Li, "Preparation and properties of polyaniline codoped with ionic liquid and dodecyl benzene sulfonic acid or hydrochloric acid," *Polymer Science, Series B*, vol. 50, no. 7, pp. 209–214, 2008.
- [29] J. F. Zhong, D. L. He, Z. Zhou, and Y. B. Xu, "Electrochemical oxidation behavior of hydroxypivalaldehyde in the ionic liquids," *Chinese Chemical Letters*, vol. 19, no. 3, pp. 319–323, 2008.

- [30] Y. Zhou and M. Antonietti, "Synthesis of very small TiO₂ nanocrystals in a room-temperature ionic liquid and their self-assembly toward mesoporous spherical aggregates," *Journal of the American Chemical Society*, vol. 125, no. 49, pp. 14960–14961, 2003.
- [31] E. T. Kang, K. G. Neoh, and K. L. Tan, "Polyaniline: a polymer with many interesting intrinsic redox states," *Progress in Polymer Science*, vol. 23, no. 2, pp. 277–324, 1998.
- [32] Y. Xia, J. M. Wiesinger, A. G. MacDiarmid, and A. J. Epstein, "Camphorsulfonic acid fully doped polyaniline emeraldine salt: conformations in different solvents studied by an ultraviolet/visible/ near-infrared spectroscopic method," *Chemistry of Materials*, vol. 7, no. 3, pp. 443–445, 1995.

Research Article

Core-Shell Structure of a Silicon Nanorod/Carbon Nanotube Field Emission Cathode

Bohr-Ran Huang,¹ Ying-Kan Yang,¹ Tzu-Ching Lin,¹ and Wen-Luh Yang²

¹ Graduate Institute of Electro-Optical Engineering and Department of Electronic Engineering,
National Taiwan University of Science and Technology, Taipei 106, Taiwan

² Department of Electronic Engineering, Feng Chia University, Taichung 407, Taiwan

Correspondence should be addressed to Tzu-Ching Lin, d9702308@mail.ntust.edu.tw

Received 30 June 2011; Revised 23 August 2011; Accepted 24 August 2011

Academic Editor: Linbao Luo

Copyright © 2012 Bohr-Ran Huang et al. This is an open access article distributed under the Creative Commons Attribution License, which permits unrestricted use, distribution, and reproduction in any medium, provided the original work is properly cited.

A novel core-shell structure of silicon nanorods/carbon nanotubes (SiNRs/CNTs) is developed for use in field emission cathodes. The CNTs were synthesized on SiNRs, using the Ag-assisted electroless etching technique to form the SiNRs/CNT core-shell structure. This resulting SiNRs/CNT field emission cathode demonstrated improved field emission properties including a lower turn-on electric field E_{on} ($1.3\text{ V}/\mu\text{m}$, $1\ \mu\text{A}/\text{cm}^2$), a lower threshold electric field E_{th} ($1.8\text{ V}/\mu\text{m}$, $1\ \text{mA}/\text{cm}^2$), and a higher enhancement factor β (2347). These superior properties indicate that this core-shell structure of SiNRs/CNTs has good potential in field emission cathode applications.

1. Introduction

Carbon nanotubes (CNTs) have unique physical and chemical properties such as a high aspect ratio, small radius of curvature, exceptional chemical inertness, excellent environmental stability, and high mechanical strength [1–5]. Given their high field emission current density at low electric field and highly stable current, CNTs can be applied to field emission cathodes [6]. However, the field emission properties of densely packed CNTs are affected by the field-screening effect among neighboring nanotubes [7]. Patterning the alignment of CNTs has been found to improve field emission properties [8–11]. Combining CNTs and other nonplanar substrates has also been used to improve field emission properties, for example, on tungsten tips [12], nanocrystalline diamond films [13], and silicon nanostructures [14–17]. CNTs have been grown on the top of silicon nanowires (SiNWs), performing the E_{on} of $2\text{ V}/\mu\text{m}$ ($10\ \mu\text{A}/\text{cm}^2$) [15]. These structures could be used to effectively improve field emission properties. CNT field emission cathodes can be fabricated by various methods such as direct growth, electrophoresis,

screen printing, the spray method, and composite plating [18–22].

In this work, the CNTs were grown directly onto the SiNRs, forming the core-shell structure of a SiNRs/CNTs field emission cathode by thermal chemical vapor deposition. Investigation of the field emission properties of SiNRs, CNTs, and the SiNRs/CNTs field emission cathode showed that this core-shell structure of SiNRs/CNTs improves the cathode field emission properties.

2. Experimental

The SiNRs were synthesized on a p-type ($1\text{--}10\ \Omega\text{cm}$, B doped, $520\ \mu\text{m}$) Cz silicon (100) wafer using the Ag-assisted electroless etching technique [23]. First, the wafer was cleaned ultrasonically for 20 min in both acetone and isopropyl alcohol. The cleaned silicon wafer was then immersed in a mixture of 5 mol/L aqueous hydrofluoric acid (HF) and 0.02 mol/L silver nitrate (AgNO_3) solution for 3 hours at room temperature. Following the electroless etching process,

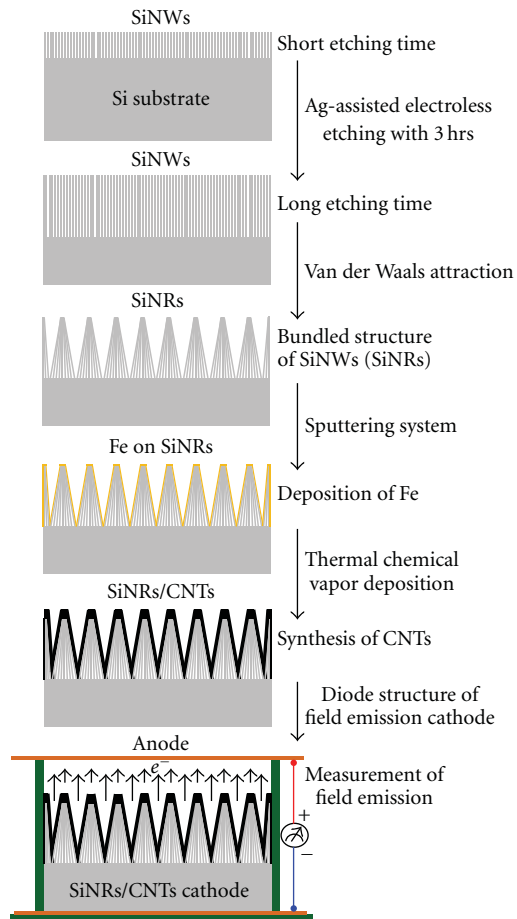


FIGURE 1: Schematic diagram of the procedures for fabricating the core-shell structure of SiNRs/CNTs field emission cathodes.

the high-density tree-like dendritic structures of silver films were removed using 30 wt% HNO_3 aqueous solution for 60 s. Finally, the samples were rinsed with deionized water and air-dried.

The as-prepared SiNRs and silicon substrate were deposited with iron (Fe) catalyst layers and immediately placed in a quartz tube furnace to grow CNTs. Furnace conditions were 700°C at atmospheric pressure with a mixed gas of N_2 and C_2H_2 (10 : 3) using the thermal chemical vapor deposition method.

The surface morphologies of films were characterized by field emission scanning electron microscopy (FESEM, JEOL JSM-6700F, operated at 15 kV) and transmission electron microscopy (TEM, Philips Tecnai F20 G2 FEI-TEM). The bonding structures of CNTs were analyzed using micro-Raman spectroscopy with excitation of spectrum 514 nm. The field emission measurements were performed using parallel-plate geometry with a gap of $150\ \mu\text{m}$ between the anode (copper) and the cathode (samples) in a vacuum chamber with a base pressure of about 1×10^{-6} Torr. A Keithley 237 was used to provide variable dc voltages and collect electric current across the specimen, and the emission measurement area was $10 \times 10\ \text{mm}^2$. Figure 1 schematically

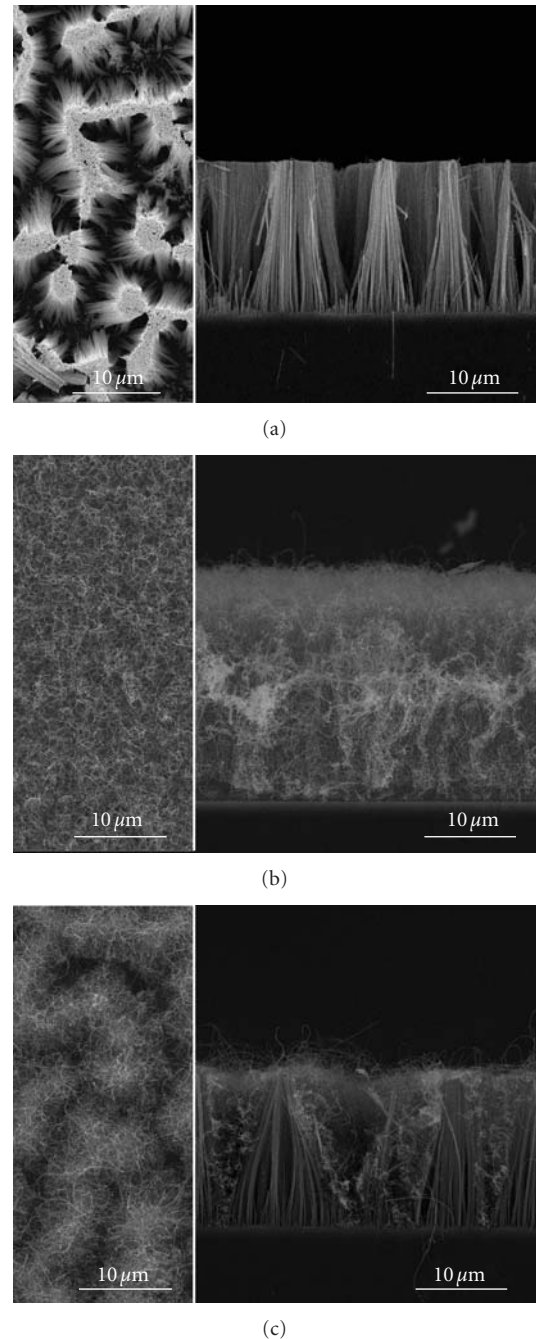


FIGURE 2: SEM images of surface and cross-section morphology of (a) SiNRs, (b) CNTs, and (c) SiNRs/CNTs.

diagrams the procedures for fabricating the core-shell structure of the SiNRs/CNTs field emission cathode.

3. Result and Discussion

Figure 2 shows the SEM images of the surface and cross-section morphology of the SiNRs, CNTs, and SiNRs/CNTs films. During the long etching time the silicon nanowires (SiNWs) take on a bundled structure, which is attributed to

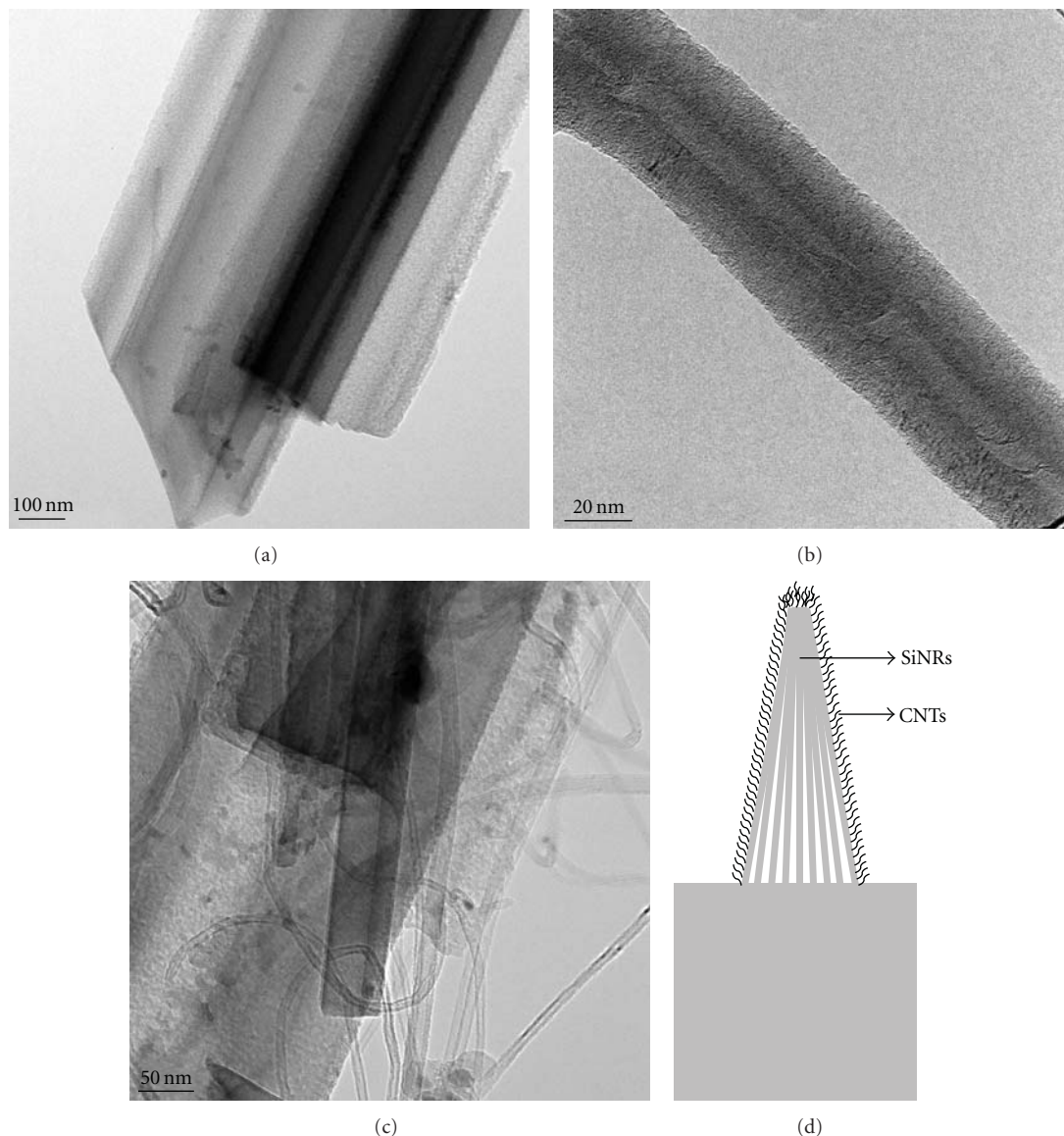


FIGURE 3: TEM images of (a) SiNR, (b) CNT, and (c) core-shell structure of SiNRs/CNTs, and (d) schematic diagram of the SiNRs/CNTs.

the strong SiNRs van der Waals attraction [24]. As a result, in this study, the SiNRs bundle structure is denominated the SiNRs. The SiNRs are separated from each other and are held perpendicular to the sample surface at an average height of $\sim 17 \mu\text{m}$. A large quantity of highly aligned CNTs film was deposited on the silicon substrate, as shown in Figure 2(b). Ten min growth produces a CNTs film with a thickness of $\sim 26 \mu\text{m}$. The physical deposition is limited to the nanoscale which causes discontinuous deposition of the Fe catalyst layer on the SiNRs. This suggests that the top of the SiNRs is covered by a thicker Fe layer than their sidewalls and bottom. Hence, the numerous entangled CNTs form the nest-shaped assemblages of CNTs on the top of each SiNRs, and the CNTs are also synthesized on the SiNRs side-walls to form a core-shell structure, as shown in Figure 2(c).

Figures 3(a)–3(c) show the TEM images of SiNRs, CNTs, and SiNRs/CNTs. Figure 3(b) shows a multiwall

nanotube with a hollow structure and reveals the well-ordered lattice fringes of the nanotube. Figure 3(c) shows that the SiNRs are surrounded by CNTs. Figure 3(d) shows the magnified schematic diagram of the core-shell structure of SiNRs/CNTs.

The Raman spectrum of CNTs typically has two characteristic peaks at around 1350 and 1580 cm^{-1} [25]. The 1580 cm^{-1} peak can be identified as the G band of crystalline graphite arising from its zone-center E_{2g} mode. For graphite-like materials with defects, the 1350 cm^{-1} peak is identified as the D band, which is activated due to defects in and disorder of the carbonaceous material. Thus, the smaller relative intensity ratio of the D and G bands (I_D/I_G) implies a better graphite structure and a higher degree of graphitization. In comparison with the localized electrons in σ bonds on CNTs, the delocalized electrons in the π orbital of the sp^2 bond have a higher degree of mobility and are more easily

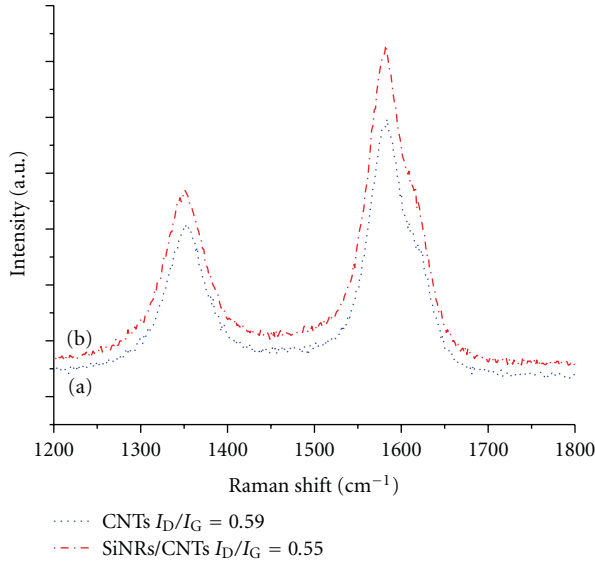


FIGURE 4: Raman spectra of (a) CNTs and (b) SiNRs/CNTs.

emitted from CNTs [26]. Therefore, greater sp^2 bonding (i.e., lower I_D/I_G ratio) would improve the field emission properties [27]. Figure 4 shows the Raman spectra of the CNTs and the SiNRs/CNTs, with respective I_D/I_G ratios of about 0.59 and 0.55. The core-shell structure does not affect the graphitization of the CNTs, which makes them applicable to field emission devices.

Figure 5 shows the current density-electric field ($J - E$) plot and the corresponding Fowler-Nordheim (FN) plot. According to the FN equation, the emission current density $J = A(\beta E)^2 \exp(-B\phi^{3/2}/\beta E)$, where A and B are constants, E is the applied electric field, β is the enhancement factor, and ϕ is the work function of 5 and 4.15 eV for CNTs and SiNRs, respectively [15, 28]. The respective E_{on} at a current density of $1 \mu A/cm^2$ for the SiNRs, CNTs, and SiNRs/CNTs field emission cathodes is 4.5, 2.4, and 1.3 $V/\mu m$. The respective E_{th} at a current density of $1 mA/cm^2$ for CNTs and SiNRs/CNTs field emission cathodes is 4.2 and 1.8 $V/\mu m$. The respective enhancement factor β of the SiNRs, CNTs, and SiNRs/CNTs field emission cathodes is estimated at about 1154, 1675, and 2347.

The field emission property with E_{th} of the core-shell structure of SiNRs/CNTs is comparable to that found in previous reports. Li and Jiang, deposited CNTs on a silicon nanoporous pillar array prepared by hydrothermal etching technique [16], which provided good field emission properties with the E_{th} about 1.9 $V/\mu m$. Qinke et al. synthesized CNTs on the top of a SiNW array prepared by Ag-assisted electroless etching [15], which showed the E_{th} at about 3.3 $V/\mu m$. CNTs only synthesized on the top of the SiNW array, which failed to effectively enhance the field emission properties. The SiNRs/CNTs field emission cathode shows not only a high enhancement factor but also low E_{on} and low E_{th} . The screening effect of densely packed CNTs produced among neighboring nanotubes resulted in disappointing CNTs field emission properties [29]. The core-shell structure

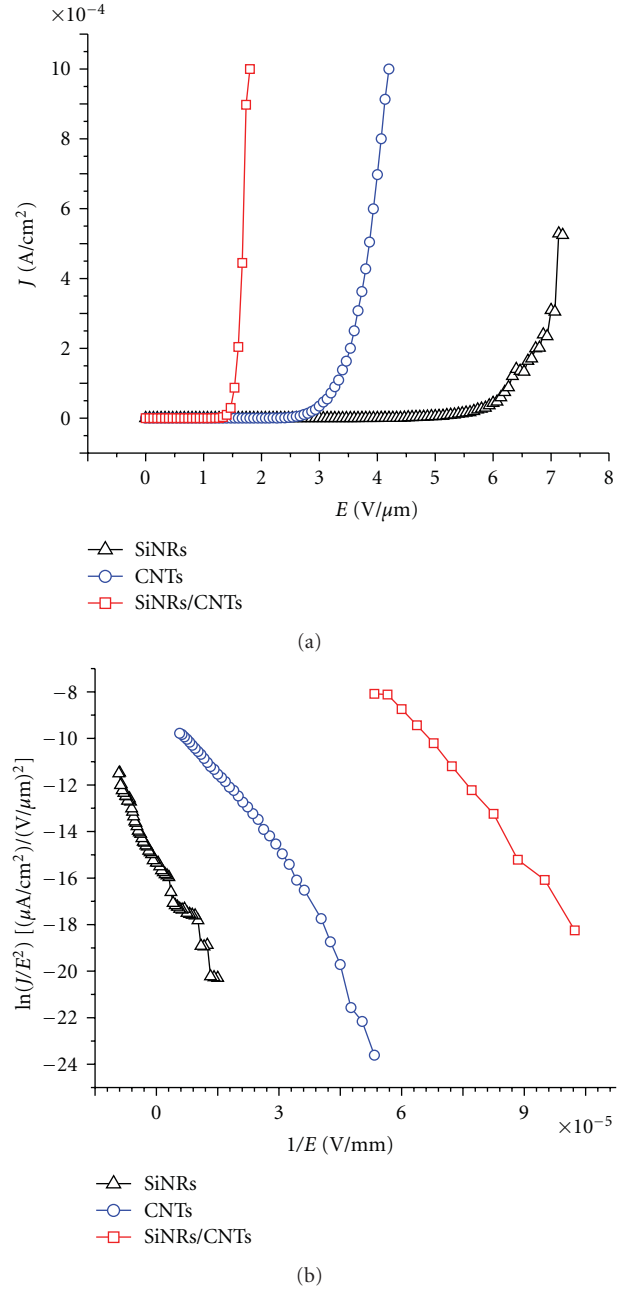


FIGURE 5: Field emission properties of the SiNRs, CNTs, and SiNRs/CNTs cathodes: (a) current density versus electric field ($J - E$) plots; (b) Fowler-Nordheim plots.

of the SiNRs/CNTs reduces the density of CNTs, thus further decreasing the screening effect and improving the field emission properties. In addition, we suggest that the SiNRs/CNTs structure could reduce the work function below 5 eV. Consistent with previous reports, the lower work function of SiNRs/CNTs field emission cathode also enhances field emission properties, resulting in a higher current density, lower turn-on electric field, and higher enhancement factor [30, 31]. However, excellent field emission properties were achieved in the CNTs field emission cathode with a core-shell structure using SiNRs. Further studies are needed

to determine the optimum SiNRs diameter and CNTs film thickness for the core-shell structure of SiNRs/CNTs cathode to promote field emission properties.

4. Conclusion

We developed a novel core-shell structure of SiNRs/CNTs for field emission cathodes, effectively improving field emission properties including an E_{on} of $1.3\text{ V}/\mu\text{m}$, E_{th} of $1.8\text{ V}/\mu\text{m}$, and β of 2347. These improvements were attributed to the SiNRs/CNTs core-shell structure reducing the screening effect and work function. These results indicate that the core-shell structure of SiNRs/CNTs might be suitable for improved cathode of field emission displays.

Acknowledgment

This work was supported by the National Science Council of Taiwan under Grant no. 99-2221-E-011-065.

References

- [1] S. Iijima, "Helical microtubules of graphitic carbon," *Nature*, vol. 354, no. 6348, pp. 56–58, 1991.
- [2] B. I. Yakobson, C. J. Brabec, and J. Bernholc, "Nanomechanics of carbon tubes: instabilities beyond linear response," *Physical Review Letters*, vol. 76, no. 14, pp. 2511–2514, 1996.
- [3] K. H. An, S. Y. Jeong, H. R. Hwang, and Y. H. Lee, "Enhanced sensitivity of a gas sensor incorporating single-walled carbon nanotube-polypyrrole nanocomposites," *Advanced Materials*, vol. 16, no. 12, pp. 1005–1009, 2004.
- [4] H. Usui, H. Matsui, N. Tanabe, and S. Yanagida, "Improved dye-sensitized solar cells using ionic nanocomposite gel electrolytes," *Journal of Photochemistry and Photobiology A*, vol. 164, no. 1-3, pp. 97–101, 2004.
- [5] W. A. De Heer, A. Châtelain, and D. Ugarte, "A carbon nanotube field-emission electron source," *Science*, vol. 270, no. 5239, pp. 1179–1180, 1995.
- [6] Y. Liu and S. Fan, "Field emission properties of carbon nanotubes grown on silicon nanowire arrays," *Solid State Communications*, vol. 133, no. 2, pp. 131–134, 2005.
- [7] L. Nilsson, O. Groening, C. Emmenegger et al., "Scanning field emission from patterned carbon nanotube films," *Applied Physics Letters*, vol. 76, no. 15, pp. 2071–2073, 2000.
- [8] H. J. Jeong, S. C. Lim, K. S. Kim, and Y. H. Lee, "Edge effect on the field emission properties from vertically aligned carbon nanotube arrays," *Carbon*, vol. 42, no. 14, pp. 3036–3039, 2004.
- [9] J. S. Suh, K. S. Jeong, J. S. Lee, and I. Han, "Study of the field-screening effect of highly ordered carbon nanotube arrays," *Applied Physics Letters*, vol. 80, no. 13, p. 2392, 2002.
- [10] R. C. Smith and S. R. P. Silva, "Maximizing the electron field emission performance of carbon nanotube arrays," *Applied Physics Letters*, vol. 94, no. 13, Article ID 133104, 3 pages, 2009.
- [11] S. H. Jo, Y. Tu, Z. P. Huang, D. L. Carnahan, D. Z. Wang, and Z. F. Ren, "Effect of length and spacing of vertically aligned carbon nanotubes on field emission properties," *Applied Physics Letters*, vol. 82, no. 20, pp. 3520–3522, 2003.
- [12] P. N. Hong, B. H. Thang, N. T. Hong, S. Lee, and P. N. Minh, "Electron field emission characteristics of carbon nanotube on tungsten tip," *Journal of Physics: Conference Series*, vol. 187, no. 1, 5 pages, 2009.
- [13] K. J. Liao, W. L. Wang, C. Z. Cai, J. W. Lu, and C. G. Hu, "Investigation on field electron emission from carbon nanotubes on nanocrystalline diamond films," *Journal of Metastable and Nanocrystalline Materials*, vol. 23, pp. 35–38, 2005.
- [14] K. Matsumoto, S. Kinoshita, Y. Gotoh, T. Uchiyama, S. Manalis, and C. Quate, "Ultralow biased field emitter using single-wall carbon nanotube directly grown onto silicon tip by thermal chemical vapor deposition," *Applied Physics Letters*, vol. 78, no. 4, pp. 539–540, 2001.
- [15] S. Qinke, J. Wei, K. Wang et al., "Fabrication and field emission properties of multi-walled carbon nanotube/silicon nanowire array," *Journal of Physics and Chemistry of Solids*, vol. 71, no. 4, pp. 708–711, 2010.
- [16] X. J. Li and W. F. Jiang, "Enhanced field emission from a nest array of multi-walled carbon nanotubes grown on a silicon nanoporous pillar array," *Nanotechnology*, vol. 18, no. 6, 5 pages, 2007.
- [17] J. Li, W. Lei, X. Zhang, B. Wang, and L. Ba, "Field emission of vertically-aligned carbon nanotube arrays grown on porous silicon substrate," *Solid-State Electronics*, vol. 48, no. 12, pp. 2147–2151, 2004.
- [18] Z. W. Pan, S. S. Xie, B. H. Chang, L. F. Sun, W. Y. Zhou, and G. Wang, "Direct growth of aligned open carbon nanotubes by chemical vapor deposition," *Chemical Physics Letters*, vol. 299, no. 1, pp. 97–102, 1999.
- [19] A. R. Boccaccini, J. Cho, J. A. Roether, B. J. C. Thomas, E. Jane Minay, and M. S. P. Shaffer, "Electrophoretic deposition of carbon nanotubes," *Carbon*, vol. 44, no. 15, pp. 3149–3160, 2006.
- [20] Y. S. Shi, C. C. Zhu, W. Qikun, and L. Xin, "Large area screen-printing cathode of CNT for FED," *Diamond and Related Materials*, vol. 12, no. 9, pp. 1449–1452, 2003.
- [21] Y. D. Lee, K. S. Lee, Y. H. Lee, and B. K. Ju, "Field emission properties of carbon nanotube film using a spray method," *Applied Surface Science*, vol. 254, no. 2, pp. 513–516, 2007.
- [22] B. R. Huang, T. C. Lin, Y. K. Yang, and S. D. Tzeng, "The stability of the CNT/Ni field emission cathode fabricated by the composite plating method," *Diamond and Related Materials*, vol. 19, no. 2-3, pp. 158–161, 2010.
- [23] T. Qiu and P. K. Chu, "Self-selective electroless plating: an approach for fabrication of functional 1D nanomaterials," *Materials Science and Engineering R*, vol. 61, no. 1-6, pp. 59–77, 2008.
- [24] K. Zhu, T. B. Vinzant, N. R. Neale, and A. J. Frank, "Removing structural disorder from oriented TiO₂ nanotube arrays: reducing the dimensionality of transport and recombination in dye-sensitized solar cells," *Nano Letters*, vol. 7, no. 12, pp. 3739–3746, 2007.
- [25] M. S. Dresselhaus, G. Dresselhaus, and P. H. Avouris, *Carbon Nanotubes: Synthesis, Properties and Applications*, vol. 80 of *Springer Series in Topics in Applied Physics*, Springer, Berlin, Germany, 2001.
- [26] S. Han and J. Ihm, "Role of the localized states in field emission of carbon nanotubes," *Physical Review B*, vol. 61, no. 15, pp. 9986–9989, 2000.
- [27] K. F. Chen, K. C. Chen, Y. C. Jiang et al., "Field emission image uniformity improvement by laser treating carbon nanotube powders," *Applied Physics Letters*, vol. 88, no. 19, Article ID 193127, 3 pages, 2006.

- [28] F. Zhao, D. D. Zhao, S. L. Wu, G. A. Cheng, and R. T. Zheng, "Fabrication and electron field emission of silicon nanowires synthesized by chemical etching," *Journal of the Korean Physical Society*, vol. 55, no. 6, pp. 2681–2684, 2009.
- [29] L. Nilsson, O. Groening, C. Emmenegger et al., "Scanning field emission from patterned carbon nanotube films," *Applied Physics Letters*, vol. 76, no. 15, pp. 2071–2073, 2000.
- [30] Z. S. Hu, F. Y. Hung, S. J. Chang et al., "Nanostructural characteristics of oxide-cap GaN nanotips by iodine-gallium ions etching," *Journal of Alloys and Compounds*, vol. 509, no. 5, pp. 2360–2363, 2011.
- [31] Y. F. Tzeng, Y. C. Lee, C. Y. Lee, H. T. Chiu, and I. N. Lin, "Electron field emission properties on UNCD coated Si-nanowires," *Diamond and Related Materials*, vol. 17, no. 4-5, pp. 753–757, 2008.

Research Article

Freestanding Ge/GeO₂ Core-Shell Nanocrystals with Varying Sizes and Shell Thicknesses: Microstructure and Photoluminescence Studies

P. K. Giri^{1,2} and Soumen Dhara¹

¹ Department of Physics, Indian Institute of Technology Guwahati, Guwahati 781039, India

² Centre for Nanotechnology, Indian Institute of Technology Guwahati, Guwahati 781039, India

Correspondence should be addressed to P. K. Giri, pravat_g@yahoo.com

Received 31 May 2011; Accepted 30 June 2011

Academic Editor: Linbao Luo

Copyright © 2012 P. K. Giri and S. Dhara. This is an open access article distributed under the Creative Commons Attribution License, which permits unrestricted use, distribution, and reproduction in any medium, provided the original work is properly cited.

Freestanding Ge/GeO₂ core-shell nanocrystals (NCs) with varying sizes and shell thicknesses were synthesized by a ball milling method. The core-shell NCs consist of single crystalline Ge core and crystalline GeO₂ shell. With increasing milling time, sizes of the NCs decrease while GeO₂ shell layer thicknesses increase. After 30 hours of milling, size of the core-shell NCs goes down to 11 nm. Analysis of high-resolution transmission electron microscope images revealed the presence of strain in the NCs and lattice distortion/dislocations in the Ge core near the interface of Ge core and GeO₂ shell. This induced a strong phonon localization effect as evident from Raman studies and leads to enhanced radiative recombination, resulting in intense photoluminescence. Strong photoluminescence peaks in the visible and UV region were observed from all the samples and are attributed to Ge/GeO₂ interface defect states. Optical Raman scattering studies confirm the formation of strained Ge/GeO₂ core-shell NCs with varying thicknesses.

1. Introduction

Nanocrystals (NCs) of indirect-gap semiconductors like Si and Ge are widely studied as they open new possibilities for applications as a building block in the optoelectronics and microelectronics [1–3]. As the exciton Bohr radius of Ge (24.3 nm) [4] is much larger than Si (4.9 nm) [5], the quantum confinement effect and hence the enhancement of bandgap are more prominent in Ge NCs. The optical properties, for example, photoluminescence (PL) in the UV-Vis region from of the isolated Ge NCs or Ge NCs embedded in SiO₂ matrix or Ge/GeO₂ core-shell NCs have been reported earlier [2, 6–10]. It is found that light emission is more prominent in the case of Ge/GeO₂ core-shell NCs. The light emission mechanism has been explained on the basis of radiative recombination via Ge quantum confined or due to interface defects at the nanocrystal/matrix or in the matrix itself. The role of interface in both passivating nonradiative states and in the formation of radiative states is also reported

to be quite significant. Now it is generally accepted that both localized defect states at the interface and quantum confinement of excitons due to size reduction have combined contributions toward UV-Vis PL from Ge NCs/GeO₂ core-shell system. It is difficult to isolate the relative contributions of interfacial defects and size, as the interfacial defect-related PL itself depends on size [11, 12]. In most of the studies the Ge or Ge/GeO₂ NCs were synthesized by high temperature annealing. Such high temperature processing is not compatible for the fabrication of electronic devices and also it can degrade the device performance. Recently, Tsai et al. [13] synthesized Ge NCs embedded in GeO_x film at low temperature without postannealing by using CO₂ laser-assisted chemical vapour deposition technique and studied its microstructure and light emission property. Here we synthesized isolated freestanding Ge/GeO₂ core-shell NCs with varying shell thicknesses by employing simple mechanical ball milling. Microstructure was analysed by X-ray diffraction (XRD) and transmission electron microscope

(TEM) and correlate the influence of shell-NCs interface on the observed PL in the UV-Vis region.

2. Experimental Details

The freestanding Ge NCs were prepared from high purity (99.999%) Ge powder by mechanical milling in a planetary ball mill for the duration of 5–30 h. The Ge powder was milled in a zirconium oxide vial with small balls of zirconium oxide. This ensures that no metallic contaminants are introduced during the milling process. The milling was performed under normal atmospheric conditions with presence of air to enable the formation of oxide shell layer over the NCs. The nanopowder samples obtained for different hours of milling were studied by high resolution X-ray diffraction (XRD) measurements (Bruker, Advance D8) in a slow scan mode. A 200 KV HRTEM (JEOL-2100) was used to study the size and the microstructure of the freestanding NCs. The UV-Visible absorption spectra of all the samples were recorded using a commercial spectrometer (Shimadzu 3010PC). The PL spectra of the freestanding core-shell Ge NCs for different milling hours were recorded (Jobin-Yvon, T64000) with an excitation of 325nm laser. Raman scattering measurement was carried out with a 488 nm Ar⁺ laser excitation using a micro-Raman spectrometer (LabRam HR800) equipped with a liquid nitrogen cooled charge coupled device (CCD) detector. Fourier transformed infrared spectroscopy (FTIR, Perkin Elmer, Spectrum BX) was used to check the chemical bonding configuration of the NCs. For discussion, we denote the unmilled, 5 h, 10 h, 20 h, 25 h, and 30 h milled Ge NCs samples as Ge-0, Ge-5, Ge-10, Ge-20, Ge-25, and Ge-30, respectively.

3. Results and Discussion

Figure 1(a) shows the TEM image of an isolated Ge/GeO₂ NC for the Ge-10 sample. The variation in contrast at the edge of the NCs (region marked with hollow arrow) indicates the presence of GeO₂ shell layer over the Ge core. Figures 1(b)–1(d) show the core-shell NCs for the Ge-20, Ge-25, and Ge-30 samples, respectively. With increase in milling time, the size of the NCs gradually decreases and after 30h of milling, average size of the NCs is 11 nm. The size obtained from the TEM images is the diameter of the core-shell NCs, whereas XRD gives the average size of the Ge core in the Ge/GeO₂ core-shell NCs. Therefore extraction of sizes obtained from TEM imaging by the sizes obtained from the XRD line profile analysis can give the estimated thickness of the shell in the core-shell NCs. In this case, we calculated the GeO₂ shell thickness in the Ge/GeO₂ NCs. It is found that shell thickness gradually increases from 0.5 nm to 1.5 nm for the milled time duration 10 h to 30 h. From Ge-5 to Ge-30, the sizes of the NCs are smaller than the exciton Bohr diameter of bulk Ge. Therefore, one would expect enhanced PL from all the samples. Insets of Figures 1(b) and 1(d) show the inverse fast Fourier transformed (FFT) lattice images of the isolated NC for the Ge-20 and Ge-30, respectively. One can clearly see the presence of lattice dislocation/distortion (region marked with solid arrow) induced defect states near

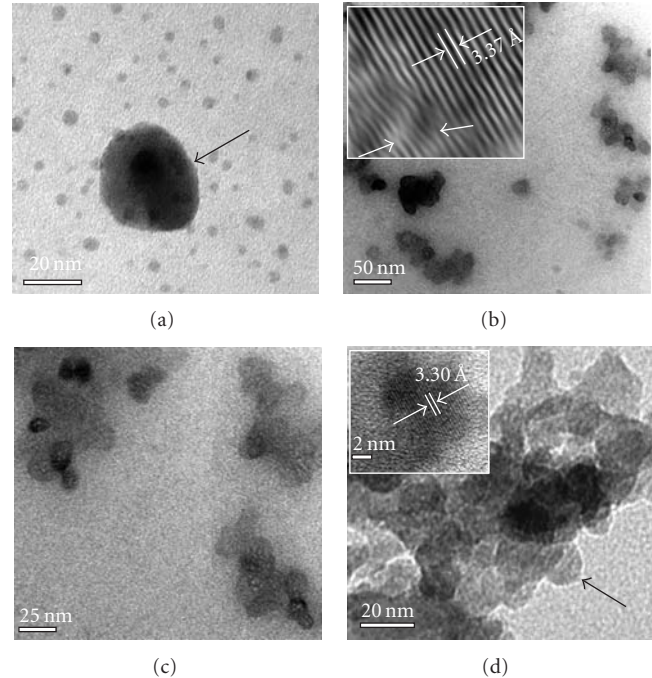


FIGURE 1: TEM images for the Ge-10, Ge-20, Ge-25, and Ge-30 NCs. Insets of (b) and (d) show the high-resolution lattice image of the Ge NCs core for the Ge-20 and Ge-30, respectively.

the grain boundary between Ge core and GeO₂ shell. The lattice spacing of the Ge core for the Ge-20 sample is calculated to be 3.37 Å, which corresponds to the (111) plane of Ge with diamond cubic structure. The calculated lattice spacing is larger than the lattice spacing of unstrained Ge (3.27 Å). This confirms that tensile strain is indeed present in the core-shell NCs. For the Ge-30 sample, it is found that lattice spacing reduced to 3.30 Å, which indicates a relaxation of lattice strain. These results are consistent with the XRD results. It is known that high densities of structural defects could lead to the phonon localization effects [14], therefore, one would expect enhanced PL properties from the ultra small and strained Ge/GeO₂ core-shell NCs due to combined effects of quantum confinement and phonon localization.

Figure 2 shows the XRD pattern of the freestanding Ge/GeO₂ core-shell NCs milled for different time durations. Along with the strong Ge(111) peak, GeO₂-related XRD peaks are also observed. With the increase in milling time, the intensities of the Ge(111) peak decrease, while intensities of GeO₂(101) peak increase. The intensity ratio of GeO₂(101) to the Ge(111) peak increases from 0.6 to 3.2. The observed intensity enhancement for the GeO₂(101) peak clearly indicates that thickness of GeO₂ layer increases with increasing milling time, while the size of the Ge NCs reduces accordingly. The XRD results clearly show the formation of Ge/GeO₂ core-shell NCs with varying thicknesses. The d spacing of Ge(111) core increases with increasing milling time up to 20 h of milling as found from shift in 2θ value. This increase in lattice spacing indicates the presence of tensile strain in the NCs, which increases with increase in shell thickness. The exact sizes of the Ge core in the Ge/GeO₂

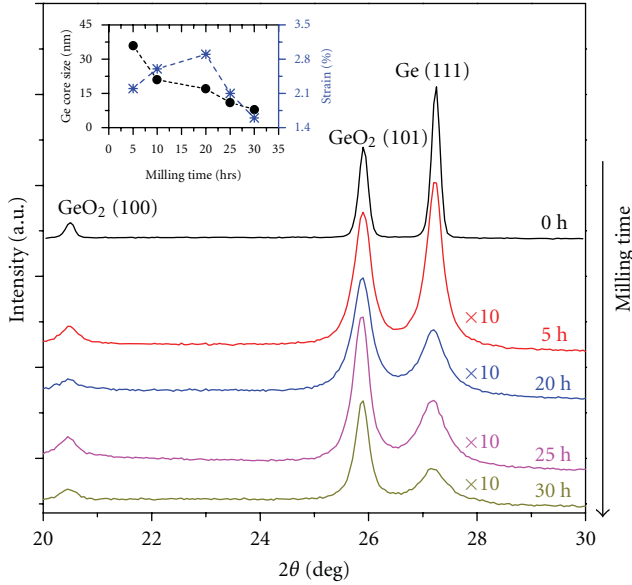


FIGURE 2: XRD patterns of the freestanding Ge/GeO₂ core-shell NCs milled for different time duration. Intensity of the GeO₂(101) peak increases systematically with increasing milling time.

NCs and the lattice strain are calculated by detailed analysis of XRD line profile. The method proposed by Ungar and Borbely [15] is used to calculate the exact Ge core size and lattice strain of the GeO₂NCs. According to the Ungar and Borbely method, individual contribution of size and strain to the broadening can be expressed as

$$\Delta K = \frac{0.9}{D_U} + 2eK\sqrt{C}, \quad (1)$$

where $\Delta K = (2\beta \cos \theta_B)/\lambda$, β is the FWHM (in radians) of the Bragg reflections, θ is the Bragg angle of the analyzed peak, λ is the wavelength of X-rays, D_U is the average crystallite size, $K = 2 \sin \theta_B/\lambda$, e is the strain, and C is the dislocation contrast factor, respectively. Details of the above calculation for Ge NCs can be found elsewhere [16]. The Sizes of the Ge core and lattice strain calculated from the above method are shown as inset of Figure 2. With increase in milling time size of the Ge core gradually decreases from 36 nm to 8 nm for 5 h to 30 h samples. On the other hand, the strain first increases up to 20 hours of milling (maximum strain ~2.9%) and then it decrease for higher milling time. This strain reduction indicates the release of tensile strain in the Ge/GeO₂ NCs. This can be explained as follows: during milling the strain and dislocations first develop, however for prolonged milling when the dislocation density is high the crystal breaks along the slip plane and thus produces smaller size NCs. In this way, NC size is reduced and strain is partly released for prolonged milling time [16].

The crystalline quality of the Ge/GeO₂ core-shell NCs and lattice strain was further studied by micro-Raman analysis, which is shown in Figure 3 for various samples. The Ge-0 sample exhibits a sharp peak at 298.5 cm⁻¹ with FWHM of 5.4 cm⁻¹ and a weak hump at ~570 cm⁻¹. These two modes are attributed as the well-known Raman active first-order and

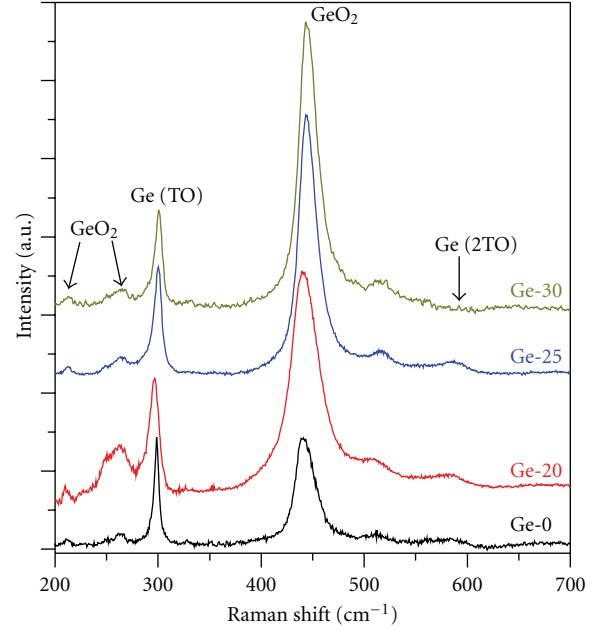


FIGURE 3: Raman spectra of the Ge/GeO₂ core-shell NCs obtained after different milling times. With increase in milling time, Raman peak intensity of GeO₂ increases while Raman peak intensity of Ge decreases.

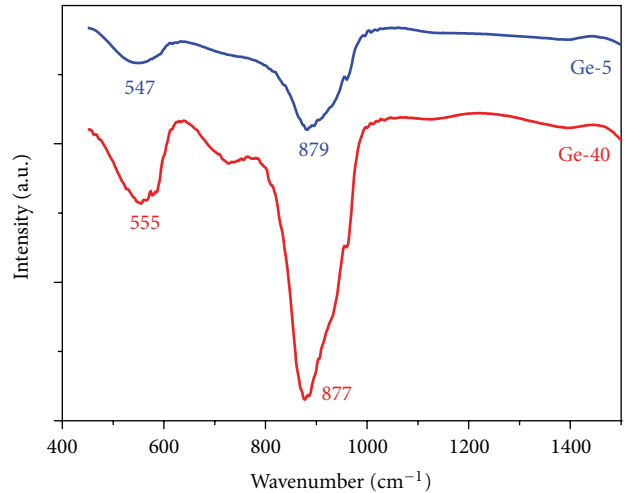


FIGURE 4: FTIR spectra for the Ge-5 and Ge-30 samples. Various Ge-O vibrational modes are labelled with corresponding wave numbers.

second-order transverse optical (TO) phonon mode of crystalline Ge [17]. Along with the TO modes of Ge, additional three modes are observed from all the samples at ~212 cm⁻¹, ~261 cm⁻¹, and ~440 cm⁻¹. These three modes are the characteristic Raman active modes of crystalline GeO₂ [18]. With increase in milling times, the intensity ratio of strongest GeO₂ Raman mode to the Ge(TO) mode increases gradually from 1.01 to 2.65. This indicates the increase of shell layer thickness from Ge-0 to Ge-30. These results are consistent with the XRD results, discussed earlier. From Ge-0 to Ge-20, the TO modes of Ge shows gradual redshift from 298.5 to

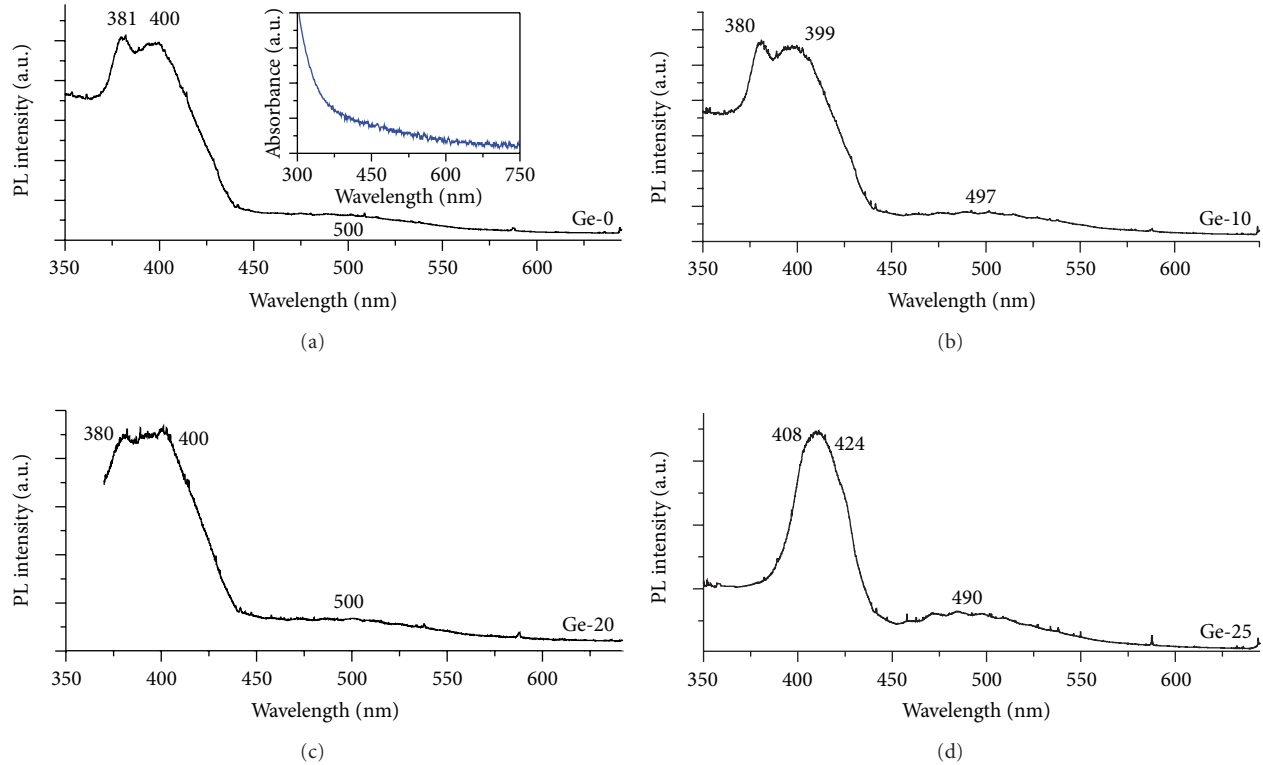


FIGURE 5: Room temperature PL spectra for the Ge-0, Ge-10, Ge-20, and Ge-25. Inset of (a) shows the absorption spectra of the corresponding Ge/GeO₂ NCs.

296.3 cm⁻¹ and FWHM increases from 5.4 to 11.7 cm⁻¹. The observed redshift is due to the combined effects of phonon confinement and tensile strain, as both the effects result in redshift in the Raman modes [19, 20]. The line width broadening is caused by size distribution of Ge NCs and phonon confinement effect in the Ge NCs. The Raman line width is known to be inversely proportional to the size of the NCs. With further milling, TO modes of Ge are blueshifted due to decrease in tensile strain by lattice relaxation. Here, observed blueshift results from the reduced tensile strain and this is consistent with the XRD analysis.

FTIR spectroscopy was employed further to investigate the chemical bonding configuration of the core-shell Ge/GeO₂ NCs. Figure 4 shows the FTIR spectra for the Ge-5 and Ge-40 samples. Two intense broad bands are observed from all the samples. The bands at 5472 cm⁻¹ and 555 cm⁻¹ correspond to the Ge-O-Ge bending modes while the bands at 879 cm⁻¹ and 877 cm⁻¹ correspond to Ge-O-Ge stretching modes of GeO₂, respectively [21]. These oxide species stem from the oxide shell layer on the Ge core.

Figure 5 shows the room temperature PL spectra for Ge-0, Ge-10, Ge-20, and Ge-25 samples. From Ge-0 to Ge-30, all the samples show strong peaks in the UV region as well as weak peak in the visible region. The UV-Vis absorption spectrum of the Ge-0 sample is shown as inset in Figure 5(a). The absorption spectrum shows strong absorption in the UV region and a weak absorption in the visible region. Other samples show similar absorption spectra with varying

intensities. Two PL emission peaks in the UV-violet region (~380–400 nm) and one peak in the green region (~500 nm) were observed from all the samples. Note that as compared to other samples, Ge-25 shows a redshift in the UV-violet peaks with PL peaks at 408 and 424 nm. Though exact mechanism of this redshift is not clear, this might be related to the relaxation of strain in the Ge-25. In all the samples, PL spectra have similar features and peak positions are nearly independent of sizes of Ge NCs. And direct recombination in GeO₂ results in PL emission below 250 nm [22]. Thus, the observed PL does not originate from the radiative recombination of excitons confined in the Ge or GeO₂ NCs. Therefore, first PL component may originate from dislocation related defects at the Ge core and GeO₂ boundary, as intensity of the first component systematically increases from Ge-0 to Ge-20. Note that, dislocation-related defect density gradually increases from Ge-0 to Ge-20. The high density of defects due to lattice dislocation/disorder, located in surface and grain boundaries of the NCs induced a significant localisation effect resulting in strong PL. The ~400 nm peak is attributed to Ge/O stoichiometric defect states at the interface [23]. As the milling was done in sealed vial, it is expected to form Ge/O stoichiometric defect states in NCs. The ~500 nm peak is originated from radiative recombination between the oxygen vacancies and oxygen-germanium vacancy centers [24]. No observable visible PL emission is observed from Ge NCs core, perhaps due to large strain that causes nonradiative recombination centres to quench the PL.

4. Conclusions

We have synthesized freestanding Ge/GeO₂ core-shell NCs with size down to 11 nm with varying shell thicknesses (up to 1.5 nm) by ball milling method. Analysis of HRTEM images and XRD patterns revealed the presence of lattice strain in the Ge core near the interface between Ge and GeO₂ and the nature of strain is tensile. With increase in milling time, lattice strain initially increases up to 20 hours of milling then partially released for further milling. The Raman scattering studies shows that observed redshift in the Raman modes results from the combined effect of quantum confinement and tensile strain. High densities of structural defects (lattice dislocation/distortion) in the synthesized NCs result in enhanced PL in the UV and visible region and are attributed to various Ge/GeO₂ interface defects. No observable visible PL emission is observed from Ge NCs core, perhaps due to large strain that causes nonradiative recombination centres to quench the PL.

References

- [1] T. C. Tsai, L. Z. Yu, and C. T. Lee, "Electroluminescence emission of crystalline silicon nanoclusters grown at a low temperature," *Nanotechnology*, vol. 18, no. 27, Article ID 275707, 2007.
- [2] Y. Maeda, "Visible photoluminescence from nanocrystallite Ge embedded in a glassy SiO₂ matrix: evidence in support of the quantum-confinement mechanism," *Physical Review B*, vol. 51, no. 3, pp. 1658–1670, 1995.
- [3] C. L. Yuan and P. S. Lee, "Enhanced charge storage capability of Ge/GeO₂ core/shell nanostructure," *Nanotechnology*, vol. 19, no. 35, Article ID 355206, 2008.
- [4] Y. Maeda, N. Tsukamoto, Y. Yazawa, Y. Kanemitsu, and Y. Masumoto, "Visible photoluminescence of Ge microcrystals embedded in SiO₂ glassy matrices," *Applied Physics Letters*, vol. 59, no. 24, pp. 3168–3170, 1991.
- [5] A. G. Cullis, L. T. Canham, and P. D. J. Calcott, "The structural and luminescence properties of porous silicon," *Journal of Applied Physics*, vol. 82, no. 3, pp. 909–966, 1997.
- [6] X. Ma, W. Shi, and B. Li, "The size dependence of the optical and electrical properties of Ge quantum dots deposited by pulsed laser deposition," *Semiconductor Science and Technology*, vol. 21, no. 5, pp. 713–716, 2006.
- [7] P. K. Giri, S. Bhattacharyya, S. Kumari et al., "Ultraviolet and blue photoluminescence from sputter deposited Ge nanocrystals embedded in SiO₂ matrix," *Journal of Applied Physics*, vol. 103, no. 10, Article ID 103534, 9 pages, 2008.
- [8] S. Takeoka, M. Fujii, S. Hayashi, and K. Yamamoto, "Size-dependent near-infrared photoluminescence from Ge nanocrystals embedded in SiO₂ matrices," *Physical Review B*, vol. 58, no. 12, pp. 7921–7925, 1998.
- [9] P. K. Sahoo, S. Dhar, S. Gasiorok, and K. P. Lieb, "Stable violet cathodoluminescence of α -quartz after Ge⁺ implantation at elevated temperature," *Journal of Applied Physics*, vol. 96, no. 3, pp. 1392–1397, 2004.
- [10] C. L. Yuan and P. S. Lee, "Enhancement of photoluminescence of Ge/GeO₂ core/shell nanoparticles," *Europhysics Letters*, vol. 83, no. 4, Article ID 47010, 5 pages, 2008.
- [11] X. X. Wang, J. G. Zhang, L. Ding et al., "Origin and evolution of photoluminescence from Si nanocrystals embedded in a SiO₂ matrix," *Physical Review B*, vol. 72, no. 19, Article ID 195313, 6 pages, 2005.
- [12] G. Hadjisavvas and P. C. Kelires, "Structure and energetics of Si nanocrystals embedded in *a*-SiO₂," *Physical Review Letters*, vol. 93, no. 22, Article ID 226104, 4 pages, 2004.
- [13] T.-C. Tsai, D.-S. Liu, L.-R. Lou, and C.-T. Lee, "Structure and photoluminescence of Ge nanoclusters embedded in GeO_x films deposited using laser assistance at low temperature," *Journal of Applied Physics*, vol. 108, no. 7, Article ID 074318, 4 pages, 2010.
- [14] N. H. Nickel, P. Lengsfeld, and I. Sieber, "Raman spectroscopy of heavily doped polycrystalline silicon thin films," *Physical Review B*, vol. 61, no. 23, pp. 15558–15561, 2000.
- [15] T. Ungar and A. Borbely, "The effect of dislocation contrast on x-ray line broadening: a new approach to line profile analysis," *Applied Physics Letters*, vol. 69, no. 21, pp. 3173–3175, 1996.
- [16] P. K. Giri, "Strain analysis on freestanding germanium nanocrystals," *Journal of Physics D*, vol. 42, no. 24, Article ID 245402, 7 pages, 2009.
- [17] Z. Sui and I. P. Herman, "Effect of strain on phonons in Si, Ge, and Si/Ge heterostructures," *Physical Review B*, vol. 48, no. 24, pp. 17938–17953, 1993.
- [18] S. Tsutomu and S. L. Jun, "Lattice dynamics and temperature dependence of the linewidth of the first-order Raman spectra for sintered hexagonal GeO₂ crystalline," *Journal of the Physical Society of Japan*, vol. 67, no. 11, pp. 3809–3815, 1998.
- [19] R. Jalilian, G. U. Sumanasekera, H. Chandrasekharan, and M. K. Sunkara, "Phonon confinement and laser heating effects in Germanium nanowires," *Physical Review B*, vol. 74, no. 15, Article ID 155421, 6 pages, 2006.
- [20] Y. Y. Fang, J. Tolle, R. Roucka et al., "Perfectly tetragonal, tensile-strained Ge on Ge_{1-y}Sn_y buffered Si(100)," *Applied Physics Letters*, vol. 90, no. 6, Article ID 061915, 3 pages, 2007.
- [21] M. Ardyanian, H. Rinnert, and M. Vergnat, "Influence of hydrogenation on the structure and visible photoluminescence of germanium oxide thin films," *Journal of Luminescence*, vol. 129, no. 7, pp. 729–733, 2009.
- [22] D. M. Christie and J. R. Chelikowsky, "Electronic and structural properties of germania polymorphs," *Physical Review B*, vol. 62, no. 22, pp. 14703–14711, 2000.
- [23] M. Zacharias and P. M. Fauchet, "Blue luminescence in films containing Ge and GeO₂ nanocrystals: the role of defects," *Applied Physics Letters*, vol. 71, no. 3, pp. 380–382, 1997.
- [24] X. C. Wu, W. H. Song, B. Zhao, Y. P. Sun, and J. J. Du, "Preparation and photoluminescence properties of crystalline GeO₂ nanowires," *Chemical Physics Letters*, vol. 349, no. 3-4, pp. 210–214, 2001.

Research Article

Synchrotron X-Ray Absorption Spectroscopy Study of Self-Assembled Nanoparticles Synthesized from $\text{Fe}(\text{acac})_3$ and $\text{Pt}(\text{acac})_2$

K. Chokprasombat,¹ C. Sirisathitkul,¹ P. Harding,¹ S. Chandarak,² and R. Yimnirun³

¹ *Molecular Technology Research Unit, School of Science, Walailak University, Nakhon Si Thammarat 80161, Thailand*

² *School of Ceramic Engineering, Institute of Engineering, Suranaree University of Technology, Nakhon Ratchasima 30000, Thailand*

³ *School of Physics, Institute of Science, Suranaree University of Technology and Synchrotron Light Research Institute (Public Organization), Nakhon Ratchasima 30000, Thailand*

Correspondence should be addressed to C. Sirisathitkul, schitnar@wu.ac.th

Received 30 May 2011; Accepted 1 July 2011

Academic Editor: Linbao Luo

Copyright © 2012 K. Chokprasombat et al. This is an open access article distributed under the Creative Commons Attribution License, which permits unrestricted use, distribution, and reproduction in any medium, provided the original work is properly cited.

The synchrotron X-ray absorption technique was used to complement electron microscopy in the investigation of nanoparticles synthesized from the coreduction of iron acetylacetonate, $\text{Fe}(\text{acac})_3$ and platinum acetylacetonate, $\text{Pt}(\text{acac})_2$. A much higher Pt composition than Fe leads to an extended X-ray absorption fine structure (EXAFS) spectrum for the sample that differs from that of fcc FePt nanoparticles. Most importantly, X-ray absorption near-edge structure (XANES) spectra clearly indicate the existence of $\alpha\text{-Fe}_2\text{O}_3$ and Pt metal. Since these monodisperse nanoparticles have a diameter of around 4 nm and tend to self-assemble into hexagonal arrangements, they can be modeled as Pt-rich cores with an $\alpha\text{-Fe}_2\text{O}_3$ shell stabilized by organic surfactants.

1. Introduction

Iron-platinum (FePt) nanoparticles are a prime candidate for the next generation of ultrahigh density recording materials [1]. Whereas other magnetic materials become hysteresis-free superparamagnetic particles when their sizes are below 10 nm, FePt nanoparticles of these sizes still exhibit ferromagnetism which is a requirement for nonvolatile recording [2]. To obtain substantial magnetic anisotropy for recording applications, not only the size but also the composition and local structure have to be controlled. It has been shown that as-synthesized FePt exhibits a chemically disordered fcc phase and is superparamagnetic but can be transformed into the ferromagnetic fct structure after heat treatment. In this fct arrangement, Fe and Pt atoms are in alternate planes with a balanced atomic ratio [3].

The synthesis of FePt nanoparticles conventionally uses the thermal decomposition of iron pentacarbonyl, $\text{Fe}(\text{CO})_5$ [3]. Since this starting material is very toxic, the coreduction

of iron acetylacetonate, $\text{Fe}(\text{acac})_3$ and platinum acetylacetonate, $\text{Pt}(\text{acac})_2$ has been studied as a green alternative [4–7]. Metal acetylacetonates are universally regarded as versatile and nontoxic precursors in the synthesis of transition metal oxide nanoparticles [8]. However, the control of the composition and local structure of the FePt product from these starting materials still remain the subject of study. Commonly, the phase is identified by X-ray diffraction (XRD). The local composition can be obtained by energy dispersive spectroscopy (EDS) whereas the global composition is averaged by inductively coupled plasma-optical emission spectroscopy (ICP-OES).

In the case of the nanoparticles synthesized from the reaction between $\text{Fe}(\text{acac})_3$ and $\text{Pt}(\text{acac})_2$ and stabilized by organic surfactants, several possible core-shell structures may be obtained. The configuration gets more complicated when the ratio between Fe and Pt is highly unbalanced or a significant amount of oxygen is present. As a result, the conclusion about the local structure cannot be reached solely

by using conventional characterization techniques. X-ray absorption spectroscopy offers a unique opportunity to shine light on local structures and complement the information on composition and phase. From X-ray absorption spectra, Shinoda et al. concluded that different synthetic conditions led to nanoparticles of varying structures including a Pt-rich FePt core with an Fe-rich amorphous shell [9]. Huang et al. studied the shift in absorption peaks as a function of thermal treatments [10] and copper additions [11]. In addition to X-ray absorption studies of FePt, Antoniak et al. demonstrated that the technique was also useful in the case of iron oxide [12]. Since we are interested in using X-ray absorption from a synchrotron radiation source to probe such nanoparticles, self-assembled nanoparticles from metal acetylacetonate precursors are used as the case study in this work. Similar studies could then be extended to other related structures including those iron oxide-coated Pt nanoparticles [13].

2. Experimental

2.1. General. Fe(acac)₃ (99.99%), Pt(acac)₂ (97%), oleic acid (90%), oleylamine (70%) were obtained from Fluka Chemical Company and used as received. Benzyl ether was degassed for 15 min before use. Other AR grade organic solvents used for purification (e.g., hexane and absolute ethanol) were used as purchased. All manipulations were performed under dry nitrogen (N₂) using standard Schlenk line techniques.

2.2. Nanoparticles Preparation. A mixture of 0.5 mmol Pt(acac)₂ and 0.5 mmol Fe(acac)₃ was added in a 100 mL Schlenk flask filled with 20 mL benzyl ether. Oxygen was removed from the reaction flask *in vacuo* before being filled with N₂. Once the solution reached 120°C, 5.0 mmol oleic acid and 5.0 mmol oleylamine as surfactants were added, and the solution was then heated to 210°C and kept at that temperature for 30 min. The black solution was refluxed at 300°C for 30 min then cooled to room temperature under N₂. The particles were precipitated by addition of ethanol and then isolated by centrifugation. The obtained precipitate was redispersed in ethanol, followed by centrifugation. This washing procedure was repeated three times. Then, the washed particles were dispersed in hexane with a small amount (*ca.* 0.05 mL) of oleic acid and oleylamine, followed by bubbling with N₂ to remove O₂. The colloid was stored in glass bottles in a refrigerator at 4°C.

2.3. Characterization Methods. For characterization, samples were prepared by depositing the colloid on solid substrates and evaporating the solvent at room temperature. The morphology of the products was examined by transmission electron microscopy (TEM) and the elemental composition was probed by EDS. X-ray absorption spectroscopy was obtained using synchrotron radiation at BL-8, Synchrotron Light Research Institute, Thailand. The X-ray absorption near-edge structure (XANES) and extended X-ray absorption fine structure (EXAFS) measurements of the Fe *K*-edge and Pt *M*₅-edge were performed in the transmission mode with an electron energy of 1.2 GeV. The spectra were collected

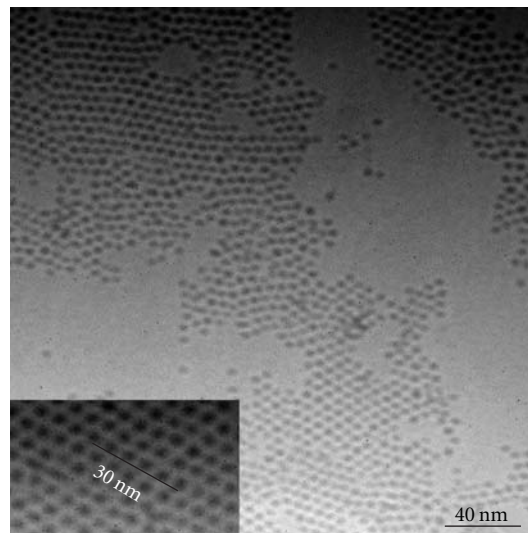


FIGURE 1: TEM images of synthesized nanoparticles.

at ambient temperature with a germanium(111) double crystal monochromator and recorded after performing an energy calibration. To increase the count rate, the ionization chamber was filled with argon gas. The storage ring was running at an energy of 1.22 GeV with electron currents between 140 mA and 80 mA.

3. Results and Discussion

The as-synthesized spherical nanoparticles in Figure 1 show a tendency to self-assemble into a hexagonal pattern. The higher magnification image in the inset reveals that these monodisperse particles have an approximate diameter of 4 nm and interparticle spacing is around 2 nm. This agrees to the observation by Nakaya et al. that such metal core dimensions and surfactants lead to a hexagonal assembly whereas larger nanoparticles (around 6 nm) tend to self-assemble into square patterns [5]. Elemental compositions of the colloid deposits by EDS analysis are 74.93% Pt, 8.24% Fe, and 16.83% O. Even though the molar ratio of Fe:Pt sources is 1:1 and a high boiling point solvent combines with high surfactants: metal ratio, Pt rich nanoparticles are still obtained rather than an ideal 1:1 stoichiometric FePt nanoparticles. This can be understood by the heterocoagulation model recently proposed by Beck et al. for the reaction between metal acetylacetonates [14]. In contrast to the binary nucleation model in which Fe-rich particles from the decomposition of Fe(CO)₅ occur simultaneously with Pt-rich particles [3], Fe(acac)₃ is harder to reduce than Pt(acac)₂, and this leads to the intermediate products of Pt-rich nuclei with the deposition of iron oxide on their surface. These iron oxides are then reduced to Fe atoms by a CO-spillover process on surface of the Pt nuclei, and the Fe atoms diffuse into the Pt-rich nuclei at high temperatures. It follows that the reduction of iron oxides is more pronounced in the case of smaller Pt nuclei (larger surface area). The composition of nanoparticles from this mechanism is

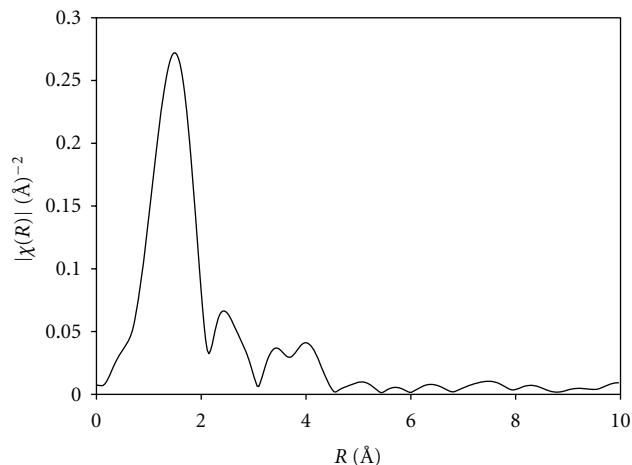


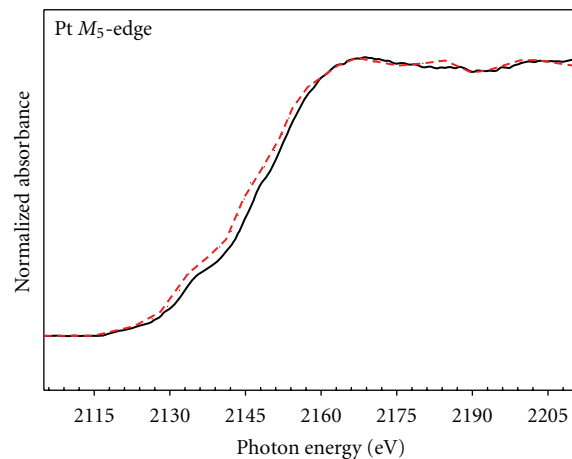
FIGURE 2: Fourier transform of Fe K-edge EXAFS spectrum of nanoparticles.

then sensitive to the reflux conditions as well as the amount of surfactants. Excessive amount of surfactants leads to particles of larger size but lowers the effectiveness of the reduction process. Moreover, the excess surfactants may impede the reduction process on the particle surface.

Fourier transformation of the EXAFS spectrum of the Fe K-edge is shown in Figure 2. The highest peak between 0.1 and 0.2 nm corresponds to nearest neighboring Fe-O correlation which is different from the Fe-Pt profile shown in work reported by Shinoda et al. [9]. The Fe K-edge and Pt M_5 -edge XANES spectra of the nanoparticles are shown in Figure 3. Between 21002–2200 eV in Figure 3(a), the profile fits well with that of the Pt standard, indicating that the sample contains Pt metal. In contrast, the XANES spectrum between 7000 and 7200 eV of the Fe K-edge does not match that of the Fe standard. Instead, as shown in Figure 3(b), it resembles that of hematite (α -Fe₂O₃) which is the most thermodynamically stable iron oxide at ambient conditions. XANES has the advantage of distinguishing the different valence states of Fe as is evident in this case because the different forms of iron oxide nanoparticles are difficult to differentiate by other techniques [12]. The results from X-ray absorption spectroscopy suggest that the sample contains mostly Pt metal and α -Fe₂O₃ with small amount of Fe metal. Since these nanoparticles have rather uniform size distribution and self-assembled arrangement, it is likely that Pt-rich cores with α -Fe₂O₃ shells are formed. This core-shell structure is surrounded by oleic acid and oleylamine. Although these surfactants are not detected by TEM or X-ray absorption spectroscopy, the model is confirmed by the stability of the nanoparticles in hexane without agglomeration and sedimentation over a long period of time.

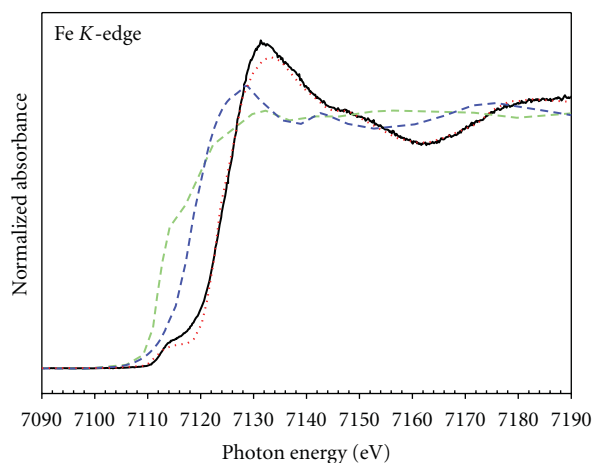
4. Conclusion

Self-assembled monodisperse nanoparticles were synthesized from the coreduction of Fe(acac)₃ and Pt(acac)₂ in the presence of benzyl ether and organic surfactants. With a composition of Fe lower than 10%, X-ray absorption spectra are



--- Pt foil
— Sample_S4

(a)



--- Fe foil
--- FeO
..... Fe₂O₃
— Sample_S4

(b)

FIGURE 3: XANES spectra of nanoparticles (Sample_S4) for (a) Pt M_5 -edge compared to Pt foil and (b) Fe K-edge compared to Fe foil, FeO, and Fe₂O₃.

consistent with a Pt-rich core with a α -Fe₂O₃ shell over an Fe-Pt alloy consistent with a heterocoagulation mechanism in a modified polyol process. It was demonstrated that the core shell can be modeled from the study by X-ray absorption spectroscopy and electron microscopy.

Acknowledgments

This project is financially supported by the National Electronics and Computer Technology Center, National Science and Technology Development Agency and Industry/University Cooperative Research Center (I/UCRC) in HDD Component, the Faculty of Engineering, Khon Kaen University. Support from Seagate (Thailand) and the proof-reading by Dr. D. James Harding are gratefully acknowledged.

References

- [1] B. D. Terris and T. Thomson, "Nanofabricated and self-assembled magnetic structures as data storage media," *Journal of Physics D*, vol. 38, no. 12, pp. R199–R222, 2005.
- [2] H. W. Zhang, Y. Liu, and S. H. Sun, "Synthesis and assembly of magnetic nanoparticles for information and energy storage applications," *Frontiers of Physics in China*, vol. 5, no. 4, pp. 347–356, 2010.
- [3] S. Sun, "Recent advances in chemical synthesis, self-assembly, and applications of FePt nanoparticles," *Advanced Materials*, vol. 18, no. 4, pp. 393–403, 2006.
- [4] V. Nandwana, K. E. Elkins, and J. P. Liu, "Magnetic hardening in ultrafine FePt nanoparticle assembled films," *Nanotechnology*, vol. 16, no. 12, pp. 2823–2826, 2005.
- [5] M. Nakaya, M. Kanehara, and T. Teranishi, "One-pot synthesis of large FePt nanoparticles from metal salts and their thermal stability," *Langmuir*, vol. 22, no. 8, pp. 3485–3487, 2006.
- [6] C. Liu, X. Wu, T. Klemmer et al., "Polyol process synthesis of monodispersed FePt nanoparticles," *Journal of Physical Chemistry B*, vol. 108, no. 20, pp. 6121–6123, 2004.
- [7] K. E. Elkins, T. S. Vedantam, J. P. Liu et al., "Ultrafine FePt nanoparticles prepared by the chemical reduction method," *Nano Letters*, vol. 3, no. 12, pp. 1647–1649, 2003.
- [8] A. L. Willis, Z. Y. Chen, J. Q. He, Y. M. Zhu, N. J. Turro, and S. O'Brien, "Metal acetylacetonates as general precursors for the synthesis of early transition metal oxide nanomaterials," *Journal of Nanomaterials*, vol. 2011, Article ID 525967, 5 pages, 2011.
- [9] K. Shinoda, K. Sato, B. Jeyadevan, K. Tohji, and S. Suzuki, "Local structural studies of directly synthesized L10 FePt nanoparticles by using XRD, XAS and SAXS," *Journal of Magnetism and Magnetic Materials*, vol. 310, no. 2, pp. 2387–2389, 2007.
- [10] T. W. Huang, Y. H. Huang, T. H. Tu, and C. H. Lee, "X-ray diffraction and absorption spectroscopy studies of the structure of self-assembled FePt nanoparticles during annealing," *Journal of Magnetism and Magnetic Materials*, vol. 282, no. SI, pp. 127–130, 2004.
- [11] T. W. Huang, T. H. Tu, Y. H. Huang, C. H. Lee, and C. M. Lin, "X-ray scattering and absorption spectroscopy study of the order-disorder transition of (FePt)_{1-x}Cu_x nanoparticles," *IEEE Transactions on Magnetics*, vol. 41, no. 2, pp. 941–943, 2005.
- [12] C. Antoniak, A. Warland, M. Darbandi et al., "X-ray absorption measurements on nanoparticle systems: self-assembled arrays and dispersions," *Journal of Physics D*, vol. 43, no. 47, Article ID 474007, 8 pages, 2010.
- [13] H. He and C. Gao, "Synthesis of Fe₃O₃/Pt nanoparticles decorated carbon nanotubes and their use as magnetically recyclable catalysts," *Journal of Nanomaterials*, vol. 2011, Article ID 193510, 10 pages, 2011.
- [14] W. Beck Jr., C. G. S. Souza, T. L. Silva, M. Jafelicci Jr., and L. C. Varanda, "Formation mechanism via a heterocoagulation approach of FePt nanoparticles using the modified polyol process," *Journal of Physical Chemistry C*, vol. 115, no. 21, pp. 10475–10482, 2011.

Research Article

In Situ Synthesis of Poly(methyl methacrylate)/SiO₂ Hybrid Nanocomposites via “Grafting Onto” Strategy Based on UV Irradiation in the Presence of Iron Aqueous Solution

Hong Zhang, Chao Li, Jinshan Guo, Limin Zang, and Jiahe Luo

Institute of Polymer Science and Engineering, College of Chemistry and Chemical Engineering, Lanzhou University, 222 Tianshui South Road, Gansu 730000, China

Correspondence should be addressed to Jinshan Guo, gjs@lzu.edu.cn

Received 11 March 2011; Revised 6 May 2011; Accepted 1 June 2011

Academic Editor: Hai-Sheng Qian

Copyright © 2012 Hong Zhang et al. This is an open access article distributed under the Creative Commons Attribution License, which permits unrestricted use, distribution, and reproduction in any medium, provided the original work is properly cited.

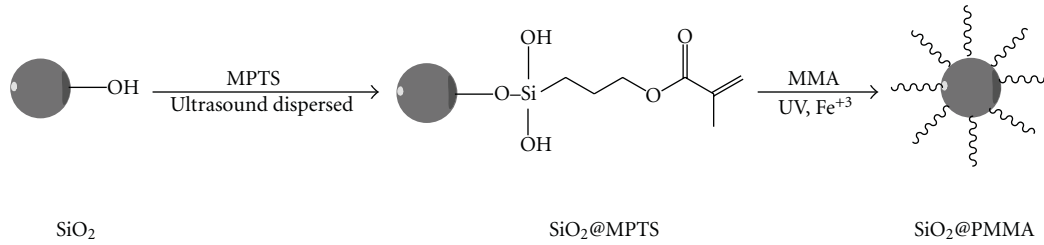
Poly(methyl methacrylate)/SiO₂ (PMMA/SiO₂) hybrid composites were prepared via “grafting onto” strategy based on UV irradiation in the presence of iron aqueous solution. Two steps were used to graft polymethyl methacrylate (PMMA) onto the surface of nanosilica, anchoring 3-(methacryloxy) propyl trimethoxysilane (MPTS) onto the surface of nanosilica to modify it with double bonds, and then grafting PMMA onto the surface of nanosilica with FeCl₃ as photoinitiator. The products were characterized by FT-IR, TGA, TEM, DLS, and XPS. The results showed that it is easy to graft PMMA onto the surface of nanosilica under UV irradiation, and the hybrid particles are monodisperse and have core-shell structure with nanosilica as the core and PMMA layers as the shell. Furthermore, the products initiated by FeCl₃ have higher monomer conversion, percent grafting, and better monodispersity compared with the products initiated by traditional photoinitiator such as 2-hydroxy-4-(2-hydroxyethoxy)-2-methyl-propiophenone (Irgacure 2959).

1. Introduction

Recently, the polymer/inorganic nanocomposites have gained great attention [1–5] because of their potential applications in many surface-based technologies such as composite materials, biomaterials, adhesion and wetting, molecular recognition, microfluidics, chemical sensing, and organic synthesis [6–12]. What is more is that the polymer/inorganic nanocomposites have excellent properties, such as mechanical properties, thermal stability, and flame retardance, gas barrier properties, and biodegradation and abrasion resistance [13–16]. The polymer/inorganic hybrid materials are generally prepared by surface modification of the inorganic particles. At present, there are many approaches for modifying solid surfaces with polymers, including physisorption, covalent attachment, and electrostatic adsorption [17]. Physisorption is relatively an easy way, but it suffers from solvolytic and thermal instabilities due to the absence of stable covalent bonds on the surface [18]. There are three approaches to covalently graft

polymer chains on the surface of inorganic particles: (1) the “grafting to” method [19, 20], where the end-functionalized polymers react with an appropriate surface; (2) the “grafting from” method [21, 22], where polymer chains are grown from initiator-terminated self-assembled monolayer; (3) the “grafting onto” method [23], where surface copolymerization is through a covalently linked monomer.

UV light has also become a useful tool for initiating polymerization due to its significant advantages [24, 25], and this method has been applied to emulsion polymerization [26, 27]. The polymerization can be easily varied by controlling the emulsifier concentration and the initiator concentration. Furthermore, it could accomplish high efficiency of the polymerization process in a short time even using a small percentage of photoinitiation. In contrast to thermally based applications which usually require elevated temperatures, photopolymerization can also be performed at room temperature and below. This is a striking advantage for both classical polymerization of monofunctional monomers and modern curing applications. Low-molecular-weight organic



SCHEME 1: The grafting polymerization of MMA from the MPTS-modified nanosilica surface.

TABLE 1: Compositions of the PMMA grafting onto silica nanoparticles.

Sample	m (SiO ₂ @MPTS) (g)	CTAB (g)	MMA (g)	FeCl ₃ ·6H ₂ O (g)	Irgacure 2959 (g)	H ₂ O (g)
S-1	0.01	0.25	5.0	0.01	—	20
S-2	0.03	0.25	5.0	0.01	—	20
S-3	0.05	0.25	5.0	0.01	—	20
S-4	0.20	0.25	5.0	0.01	—	20
S-5	0.50	0.25	5.0	0.01	—	20
S-6	0.05	0.25	5.0	—	0.01	20

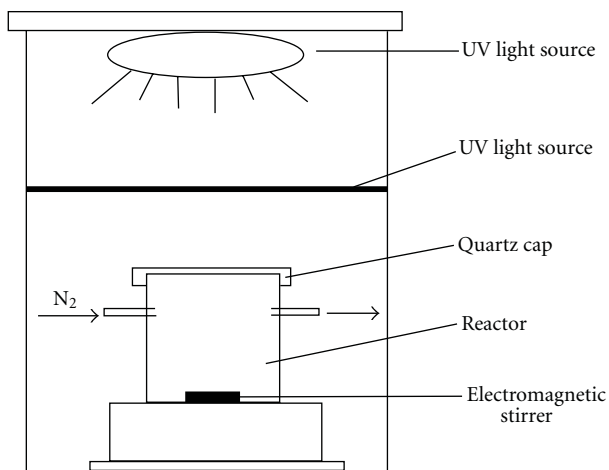


FIGURE 1: A schematic representation of the UV initiated polymerization reacting setup.

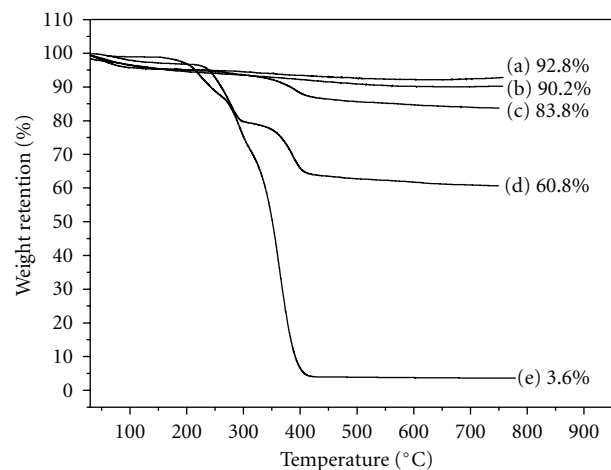


FIGURE 3: Thermogravimetric analysis (TGA) of (a) bare silica, (b) SiO₂@MPTS particles, (c) SiO₂@PMMA particles (S-5), (d) SiO₂@PMMA particles (S-4), and (e) SiO₂@PMMA particles (S-3); TGA was performed in nitrogen at a heating rate of 10° C/min.

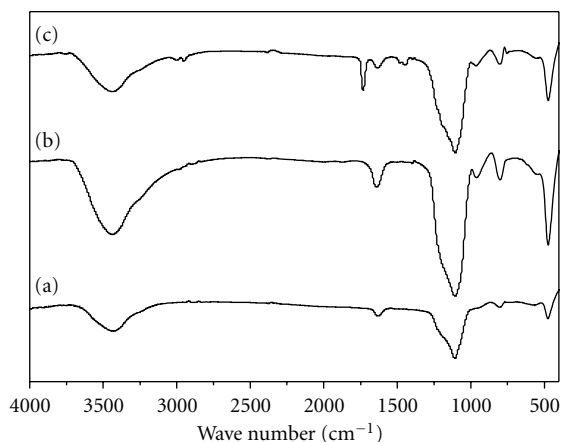


FIGURE 2: FTIR spectra of (a) bare silica particles, (b) SiO₂@MPTS particles, and (c) SiO₂@PMMA particles.

photoinitiators, however, have many intrinsic disadvantages such as hydrophobicity, odor, and toxicity, which limit the applications of photoinitiation in emulsion polymerization. One possible way to solve this problem is the use of water-soluble inorganic photoinitiators.

In this work, we used FeCl₃ as photoinitiator to prepare PMMA/SiO₂ hybrid nanocomposites. The likely mechanism of photoinitiation using Fe³⁺ as photoinitiator has been reported by Evans et al. [28]. It has been found in our research that it possesses high efficient photoinitiation even though using a small percentage of photoinitiation. Moreover, there are several advantages by using FeCl₃ as photoinitiator such as water solubility, nonpollution, and odorlessness. After the polymerization, it could be scoured

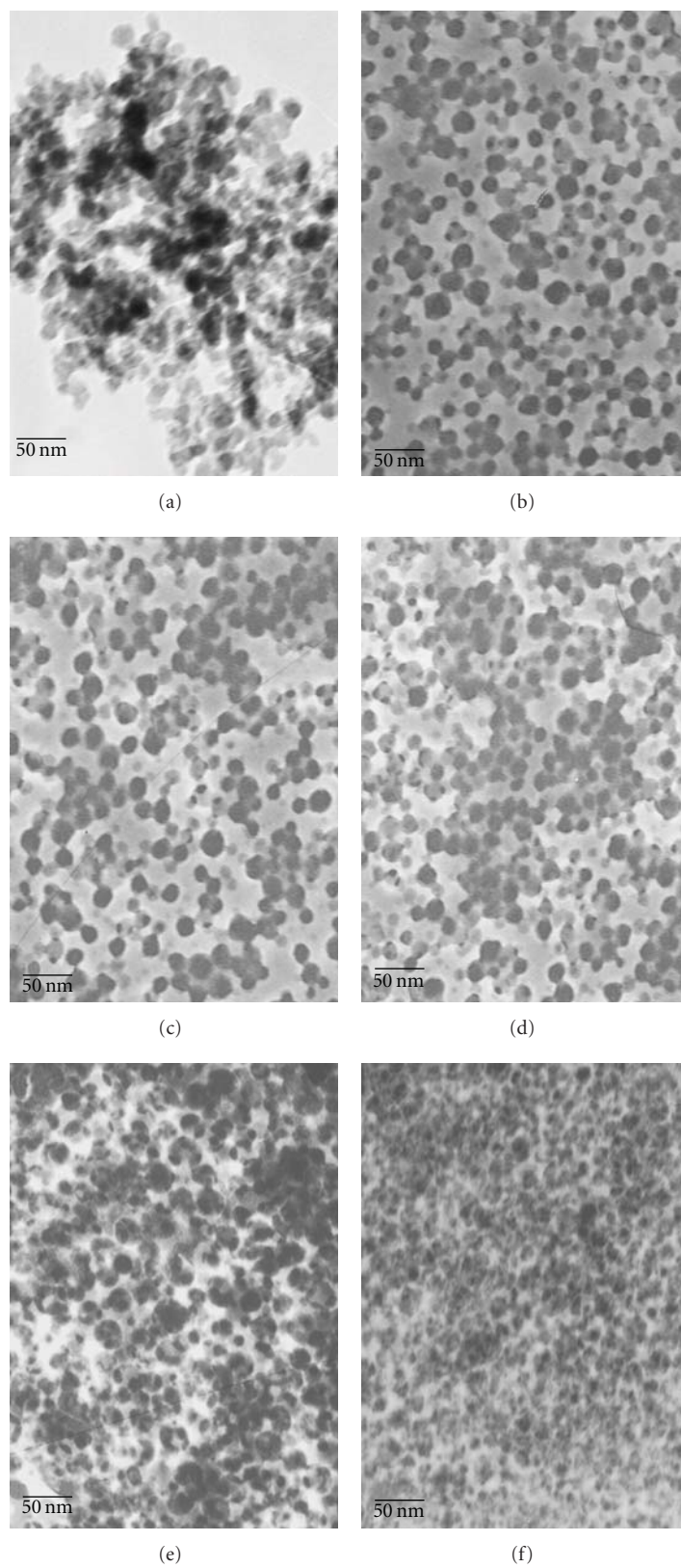


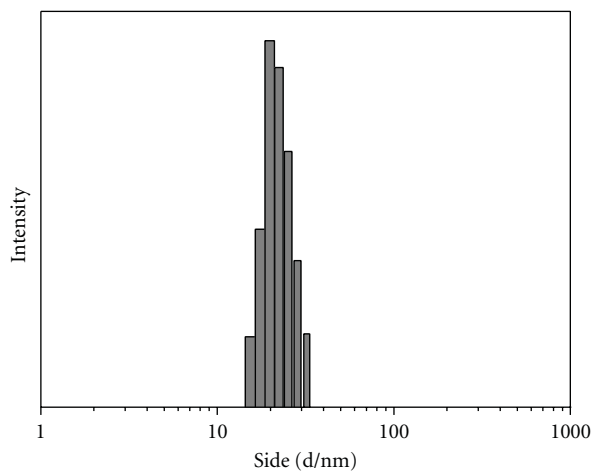
FIGURE 4: TEM images of (a) bare silica particles, (b) SiO₂@PMMA particles (S-1), (c) SiO₂@PMMA particles (S-2), (d) SiO₂@PMMA particles (S-3), (e) SiO₂@PMMA particles (S-4), and (f) SiO₂@PMMA particles (S-5) cast from dilute deionized water.

TABLE 2: Comparison of UV-initiated polymerization initiated by FeCl_3 and Irgacure 2959.

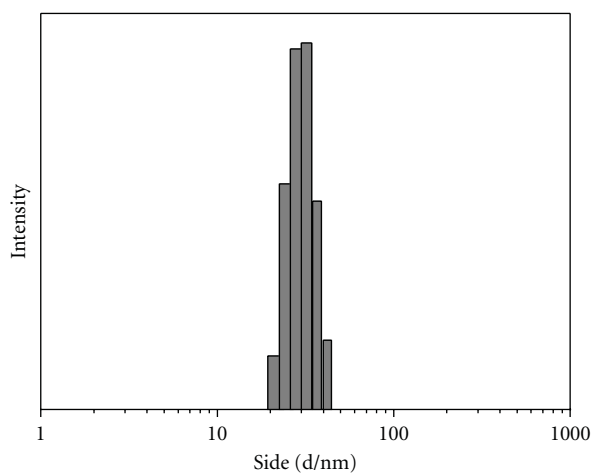
Sample	Particle size (nm)	PDI	Reaction time (min)	Conversion (%) ^a	Grafting (%) ^b
S-3	32	0.289	10	95.4	98.0
S-6	27	0.352	10	75.7	85.8

^a Conversion values determined using gravimetric analysis.

^b Polymer grafting (%) is calculated from (2).



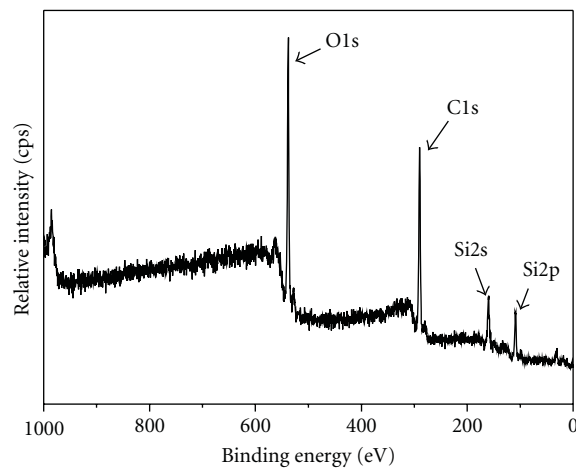
(a)



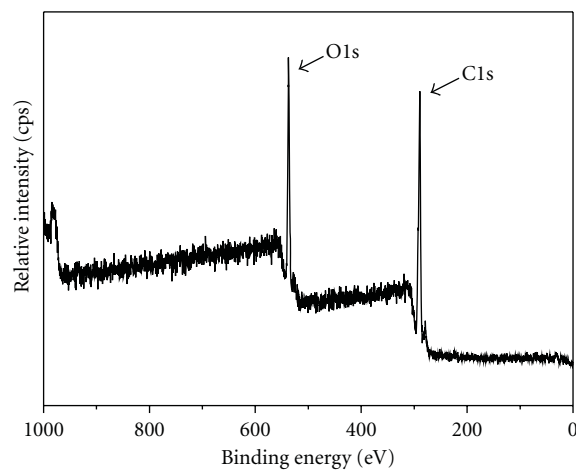
(b)

FIGURE 5: DLS images of (a) bare silica particles and (b) SiO_2 @PMMA particles (S-3).

off easily. Compared to the traditional photoinitiation initiated by Irgacure 2959, the products initiated by FeCl_3 have higher monomer conversion, percent grafting, and better monodispersity. Considering the above factors, herein, we describe an effective strategy to prepare PMMA/ SiO_2 hybrid composites via “grafting onto” strategy based on UV irradiation in the presence of iron aqueous solution. Nanosilica particles have been surface modified by 3-(methacryloxy) propyl trimethoxysilane (MPTS) to possess double bonds, so that methyl methacrylate (MMA) can be grafted onto SiO_2 with nanosilica as the core and PMMA as the shell. FeCl_3 was used for the photoinitiator



(a)



(b)

FIGURE 6: XPS wide scan for (a) SiO_2 @MPTS particles and (b) SiO_2 @PMMA particles (S-3).

under UV irradiation in this process. Scheme 1 shows the overall synthesis route. The products were characterized by FT-IR, TGA, TEM, XPS, and DLS. In addition, different proportions of SiO_2 were added to discuss the best condition of preparing PMMA/ SiO_2 particles with better monodispersity and uniform morphology.

2. Experimental Section

2.1. Materials. The silica having mean particle size of 20 nm was kindly supplied by Aladdin Chemical Reagent Co., Ltd. 3-(methacryloxy) propyl trimethoxysilane (MPTS)

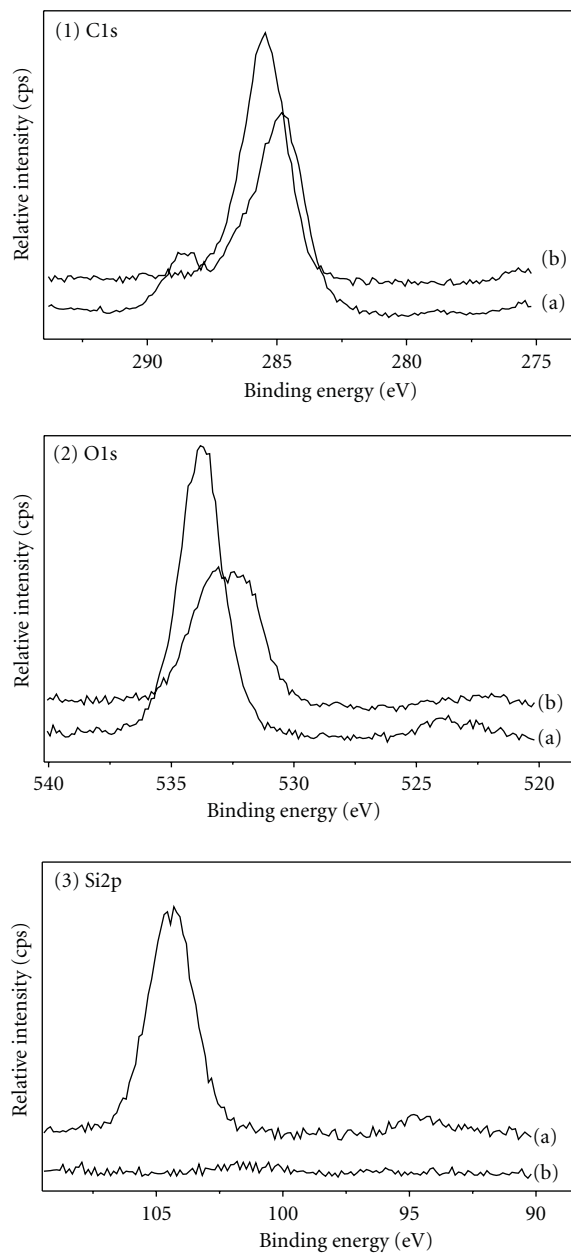


FIGURE 7: XPS analysis of C1s (1), O1s (2), and Si2p (3) spectra for (a) SiO₂@MPTS particles and (b) SiO₂@PMMA particles.

was acquired from Aldrich Chemical Co., Ltd. Hexa-aquo iron(III) chloride, FeCl₃·6H₂O (Across Organics, 99%), was used as received. MMA (Fluka, 99%) was distilled to an ice bath under reduced pressure in the presence of hydroquinone, washed twice with 5% NaOH in water, and dried over CaCl₂. Cetytrimethylammonium bromide (CTAB) was purchased from Sigma-Aldrich Chemical Co. (St. Louis, Mo). 2-hydroxy-4-(2-hydroxyethoxy)-2-methyl-propionophenone (Irgacure 2959) was acquired from Sigma-Aldrich Co. All chemicals were of analytical grade and used without further purification. Doubly deionized water was used through all the processes.

2.2. Characterization. The FTIR measurements (Impact 400, Nicolet, Waltham, Mass) were carried out with the KBr pellet method. Thermogravimetric analysis (TGA) results were obtained with a TA Instrument 2050 thermogravimetric analyzer at a heating rate of 10°C/min from 25 to 800°C under a nitrogen atmosphere. The microstructure of these hybrid nanocomposites was imaged using Hitachi H-600 equipment, and TEM samples of nanoparticles were prepared by casting one drop of a dilute colloid solution onto a carbon-coated copper grid. X-ray photoelectron spectra (XPS) were performed on a PHI-5702 instrument using MgK α radiation with pass energy of 29.35 eV. The product particle size and its distribution were determined by dynamic light scattering (DLS) using a Malvern Zetasizer NanoZS apparatus with a laser of 660 nm wavelength at 25°C. Before the analysis, the latexes were diluted with deionized water to minimize the particle-particle interactions.

2.3. Synthesis

2.3.1. Surface Modification of Silica Particles. Into a 250 mL dried round-bottom flask, 3.0 g nanosilica was ultrasound dispersed in 100 mL ethanol for 30 min, then 2.5 g MPTS was added and ultrasound dispersed for 2 h. The product was washed by centrifugations/redispersions three times in ethanol and dried in vacuum at room temperature for 24 h. The grafting density of grafted vinyl group was determined by TGA and was calculated by [29]

Grafting density (mol/m²)

$$= \frac{(W_{60-730}/(100 - W_{60-730})) \times 100 - W_{\text{silica}}}{MS_{\text{spec}} \times 100} \times 10^6, \quad (1)$$

where W_{60-730} is the weight loss from 60 to 730°C corresponding to the decomposition of the MPTS, M (g/mol) is the molar mass of the degradable part of the grafted molecule (205 g/mol), S_{spec} (m²/g) and W_{silica} are the specific surface area and the weight loss of silica determined before grafting, respectively.

2.3.2. Photopolymerization of PMMA on SiO₂@MPTS. PMMA/SiO₂ hybrid nanoparticles were synthesized through surface-grafted photopolymerization using a high-pressure Hg lamp as the UV light source. The compositions of emulsion are listed in Table 1. A pre-emulsification of SiO₂-g-MPTS, MMA, CTAB, FeCl₃·6H₂O (or Irgacure 2959), and water was carried out for 30 min in a flask with stirring at a speed of 400 rpm. The polymerization was conducted for 10 min in a reactor with a quartz cap as shown in Figure 1. The UV source used was a 1000 W high-pressure mercury lamp, and the light intensity was 20 mW/cm². During the UV irradiation, stirring and a nitrogen purge were maintained at ambient temperature. Hybrid particles were isolated via centrifugation at 4000 rpm. Then the particles were dispersed into 10 mL of tetrahydrofuran (THF) to remove PMMA absorbed on the particles. The solvent (THF) was replaced every eight hours. Particles were purified by centrifugation/redispersion for three times and then dried at

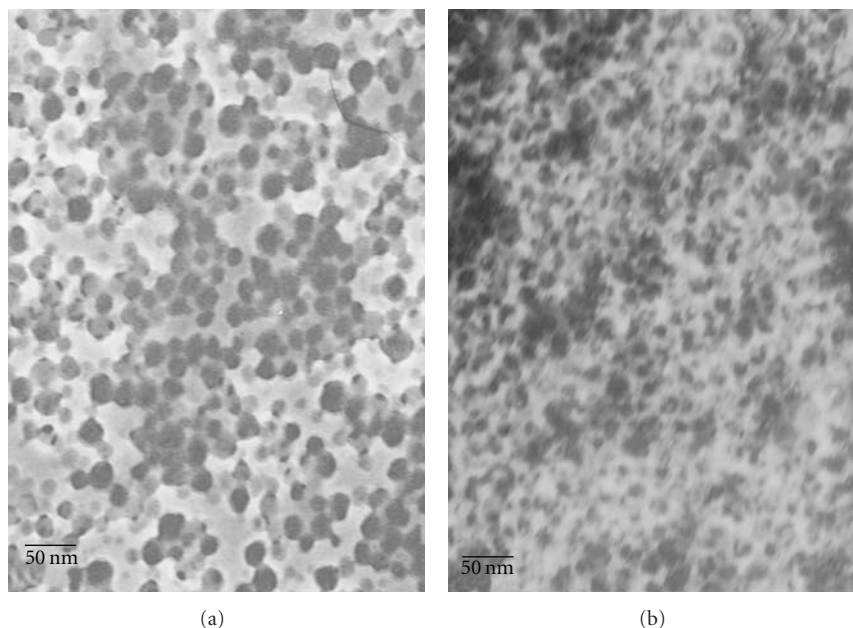
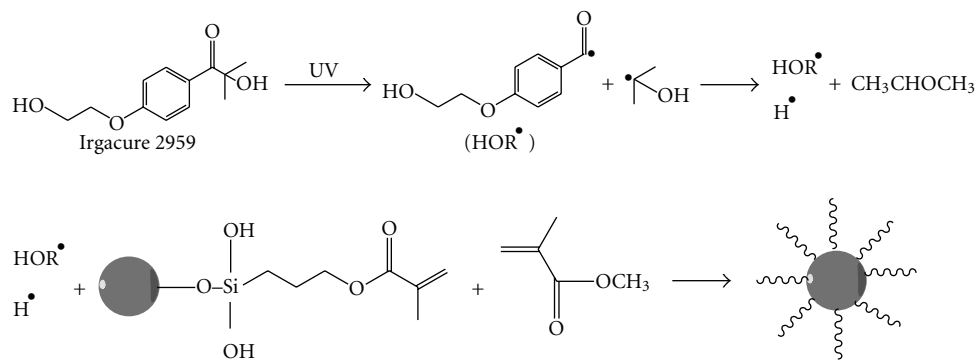


FIGURE 8: TEM images of (a) SiO₂@PMMA particles (S-3) and (b) SiO₂@PMMA particles (S-6) cast from dilute deionized water.



SCHEME 2: The mechanisms of grafting polymerization initiated by Irgacure 2959.

room temperature under a vacuum to generate PMMA/SiO₂ hybrid nanoparticles.

The polymer grafting (%) was determined by TGA and calculated by [30]

$$\text{Polymer grafting (\%)} = \frac{\text{Organic composition/g}}{\text{Bare silica/g}} \times 100, \quad (2)$$

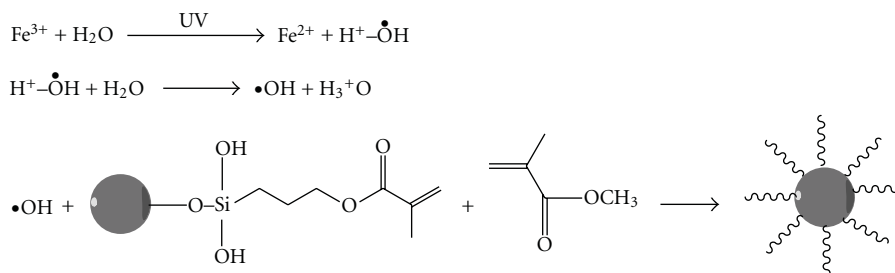
where the amount of organic composition (g) was calculated from the TGA weight loss from 150 to 700°C corresponding to the decomposition of PMMA. Bare silica (g) is the weight retention by TGA corresponding to the bare silica.

3. Results and Discussions

3.1. Analysis of FTIR. MPTS is well accepted as a suitable coupling agent for silica since the trimethoxysilyl groups can be hydrolyzed and condensed with the silanol groups at the surface of silica particles. Then, the nanosilica can be chemically modified by the reaction between PMMA and

MPTS. Figure 2 shows the FTIR spectra of SiO₂, SiO₂-g-MPTS, and PMMA/SiO₂. It can be seen that there is a very pronounced band appearing at 1108 cm⁻¹, together with two less pronounced bands at 805 and 475 cm⁻¹ in the spectrum of SiO₂ as shown in Figure 2(a), which corresponds to the vibration absorption of Si-O-Si groups. The similar consequence appears in SiO₂-g-MPTS in Figure 2(b). In the spectrum of PMMA/SiO₂ in Figure 2(c), there are peaks at 2952, 1732, and 1445 cm⁻¹, which are assigned to CH, C-O, and CH₃ stretching vibration of PMMA, respectively. This result indicates that PMMA has been grafted onto the surface of SiO₂ successfully.

3.2. Analysis by TGA. The thermogravimetric analysis (TGA) of bare silica, SiO₂-g-MPTS, and PMMA/SiO₂ particles (S-3, S-4 and S-5) is shown in Figure 3. The high temperature required to decompose and evaporate the organic content of the modified silica particles demonstrates that the silane-coupling agent is strongly bound to the particle surface and one can expect a covalent bond [31]. Calculation



SCHEME 3: The mechanisms of grafting polymerization initiated by FeCl_3 .

based on TGA shows that the grafting density of grafted vinyl group is $0.92 \mu\text{mol}/\text{m}^2$ calculated from (1). The weight loss of bare silica below 200°C is 4.8% which is attributed to the physisorbed water and residual organic solvent. As for PMMA/SiO_2 particles, the beginning decomposition at 300°C corresponds to the decomposed temperature of PMMA covalently attached to nanosilica particles. The weight loss is increased from 9.0% to 89.2% when the SiO_2 -g-MPTS decreased from 0.50 g to 0.05 g and polymer grafting is increased from 13.5% to 98.0%. These results show that the grafting degree increase resulted from the decreasing of the amount of the modified nanosilica.

3.3. Analysis by TEM. The morphologies of bare silica particles and functional silica particles modified by PMMA were investigated by TEM as shown in Figure 4. Figure 4(a) revealed that the bare silica particles with an average effective diameter of 20 nm are low dispersed and have a few aggregates. However, the size of PMMA/SiO_2 particles becomes larger than bare silica particles, and the dispersibility has been improved. With an increase of the concentration of SiO_2 -g-MPTS, the aggregates increased and the dispersibility got worse. Figures 4(b), 4(c), and 4(d) show better dispersibility. In Figure 4(d), silica particles are completely encapsulated with PMMA that free silica can nearly not be observed and most of the hybrid nanoparticles appeared to be roughly spherically symmetric, although several larger nanoparticles appeared to be rather irregular. It can be concluded that PMMA can successfully encapsulate on silica once silica particles are modified by the double bonds. Besides, it exists a suitable MMA/SiO_2 ratio to prepare the core-shell structural PMMA/SiO_2 effectively.

3.4. Analysis by DLS. The sizes and distributions of bare silica particles and functional silica particles modified by PMMA have been investigated by DLS. Figure 5(a) shows that bare silica particles possess a narrow distribution with an average effective diameter of 20 nm. This result agreed with the measure of TEM. The size of PMMA/SiO_2 in Figure 5(b) became bigger, and its size distribution ranged from 20 to 42 nm with one intensive peak at 32 nm. From the result obtained, it can be assumed that PMMA has been grafted onto the surface of the silica nanoparticles successfully, and finally the core/shell structural nanosilica/polymethyl methacrylate composite latex has been formed.

3.5. Analysis by XPS. XPS measurement was used to further investigate the composition of the polymer on the silica surface. The wide scan XPS spectra of SiO_2 -g-MPTS (a) and PMMA/SiO_2 (b) are shown in Figure 6. We can see that the signals of Si2s (160.9 eV) and Si2p (109.3 eV) in Figure 6(b) are much weaker than in Figure 6(a), which indicates that silica particles are basically encapsulated with PMMA. We can see from the wide scan XPS spectra of PMMA/SiO_2 as shown in Figure 7(1)(b) that the strongest signal appears, which corresponds to the aliphatic hydrocarbon (C-C/C-H, at a binding energy of 284.7 eV). It is larger than the C1s signal (285.4 eV) intensity of SiO_2 -g-MPTS in Figure 7(1)(a). These signals indicate the presence of PMMA on the surface of silica. Figure 7(2) is the O1s XPS scan spectra; the O1s signal of MPTS-modified silica is due to the Si-O bond. As for O1s signal of the PMMA/SiO_2 , the weak signal shifted to a binding energy of 533.8 eV, which corresponds to the carbonyl oxygen (O=C) of methyl methacrylate. Judging by combination of FTIR and XPS results, we can conclude that a functionalized surface has been generated by the method outlined in Scheme 1.

3.6. Analysis of Photoinitiation by Different Photoinitiator. Figure 8 shows the TEM images of PMMA/SiO_2 particles initiated by FeCl_3 and Irgacure 2959. It is obvious that PMMA/SiO_2 particles initiated by FeCl_3 presents better dispersion, uniformity, and higher encapsulated ratio. To make a further comparison between the FeCl_3 and Irgacure 2959, different emulsions have been carried out and the results are presented in Table 2. As shown in Table 2, the two products have almost the same size. The particles initiated by FeCl_3 have smaller polydispersity index (PDI) than initiated by Irgacure 2959. More significantly, the particles initiated by FeCl_3 have higher monomer conversion and percent grafting. This proves that FeCl_3 possesses higher efficiency than Irgacure 2959. The probable mechanisms of grafting polymerization initiated by Irgacure 2959 and FeCl_3 are shown in Schemes 2 and 3, respectively. Consequently, we can conclude that FeCl_3 has preferable property due to its well water-solubility, lower steric hindrance, and higher free radical production rate. Besides, small amounts of FeCl_3 can promote the stability of emulsion.

4. Conclusions

A simple and convenient “grafting onto” strategy which involves two-step reaction to prepare PMMA/SiO_2 hybrid

composites by UV irradiation is reported. Well-defined hybrid particles have been obtained via emulsion polymerization. The grafting density of the polymer can be adjusted in a wide range by simply controlling the introduction and the conversion of the double bonds on the silica surface. Especially, a small amount of FeCl₃ can initiate the polymerization in 10 min. It is highly efficient for the functionalization of nanosilica. Compared to the traditional photoinitiation initiated by Irgacure 2959, the products initiated by FeCl₃ have higher monomer conversion, percent grafting, and better monodispersity.

References

- [1] S. T. Milner, "Polymer brushes," *Science*, vol. 251, no. 4996, pp. 905–914, 1991.
- [2] L. P. Wang, Y. P. Wang, R. M. Wang, and S. C. Zhang, "Preparation of polymer brushes on palygorskite surfaces via RAFT polymerization," *Reactive and Functional Polymers*, vol. 68, no. 2, pp. 643–648, 2008.
- [3] A. M. Granville, S. G. Boyes, B. Akgun, M. D. Foster, and W. J. Brittain, "Thermo-responsive behavior of semi-fluorinated polymer brushes on flat substrates," *Macromolecules*, vol. 38, no. 8, pp. 3263–3270, 2005.
- [4] Q. Zhou, X. Fan, C. Xia, J. Mays, and R. Advincula, "Living anionic surface initiated polymerization (SIP) of styrene clay surfaces," *Chemistry of Materials*, vol. 13, no. 8, pp. 2465–2467, 2001.
- [5] X. Fan, C. Xia, T. Fulghum, M. K. Park, J. Locklin, and R. C. Advincula, "Polymer brushes grafted from clay nanoparticles adsorbed on a planar substrate by free radical surface-initiated polymerization," *Langmuir*, vol. 19, no. 3, pp. 916–923, 2003.
- [6] D. A. Rider, J. I. L. Chen, J. C. Eloi et al., "Controlling the morphologies of organometallic block copolymers in the 3-dimensional spatial confinement of colloidal and inverse colloidal crystals," *Macromolecules*, vol. 41, no. 6, pp. 2250–2259, 2008.
- [7] W. Norde and D. Gags, "Interaction of bovine serum albumin and human blood plasma with PEO-tethered surfaces: influence of PEO chain length, grafting density, and temperature," *Langmuir*, vol. 20, no. 10, pp. 4162–4167, 2004.
- [8] J. Lahiri, L. Isaacs, B. Grzybowski, J. D. Carbeck, and G. M. Whitesides, "Biospecific binding of carbonic anhydrase to mixed SAMs presenting benzenesulfonamide ligands: a model system for studying lateral steric effects," *Langmuir*, vol. 15, no. 21, pp. 7186–7198, 1999.
- [9] A. Hucknall, S. Rangarajan, and A. Chilkoti, "In pursuit of zero: polymer brushes that resist the adsorption of proteins," *Advanced Materials*, vol. 21, no. 23, pp. 2441–2446, 2009.
- [10] D. E. Kataoka and S. M. Troian, "Patterning liquid flow on the microscopic scale," *Nature*, vol. 402, no. 6763, pp. 794–797, 1999.
- [11] B. Zhao and W. J. Brittain, "Polymer brushes: surface-immobilized macromolecules," *Progress in Polymer Science*, vol. 25, no. 5, pp. 677–710, 2000.
- [12] J. W. Park and E. L. Thomas, "A surface-reactive rod-coil diblock copolymer: nano- and micropatterned polymer brushes," *Journal of the American Chemical Society*, vol. 124, no. 4, pp. 514–515, 2002.
- [13] F. Gong, M. Feng, C. Zhao, S. Zhang, and M. Yang, "Thermal properties of poly(vinyl chloride)/montmorillonite nanocomposites," *Polymer Degradation and Stability*, vol. 84, no. 2, pp. 289–294, 2004.
- [14] H. Zheng, Y. Zhang, Z. Peng, and Y. Zhang, "Influence of clay modification on the structure and mechanical properties of EPDM/montmorillonite nanocomposites," *Polymer Testing*, vol. 23, no. 2, pp. 217–223, 2004.
- [15] J. Y. Lee and H. K. Lee, "Characterization of organobentonite used for polymer nanocomposites," *Materials Chemistry and Physics*, vol. 85, no. 2-3, pp. 410–415, 2004.
- [16] F. Gong, M. Feng, C. Zhao, S. Zhang, and M. Yang, "Particle configuration and mechanical properties of poly(vinyl chloride)/montmorillonite nanocomposites via in situ suspension polymerization," *Polymer Testing*, vol. 23, no. 7, pp. 847–853, 2004.
- [17] D. C. Tully, A. R. Trimble, J. M. J. Fréchet, K. Wilder, and C. F. Quate, "Synthesis and preparation of ionically bound dendrimer monolayers and application toward scanning probe lithography," *Chemistry of Materials*, vol. 11, no. 10, pp. 2892–2898, 1999.
- [18] B. Zhao and W. J. Brittain, "Synthesis of polystyrene brushes on silicate substrates via carbocationic polymerization from self-assembled monolayers," *Macromolecules*, vol. 33, no. 2, pp. 342–348, 2000.
- [19] Y. Tran and P. Auroy, "Synthesis of poly(styrene sulfonate) brushes," *Journal of the American Chemical Society*, vol. 123, no. 16, pp. 3644–3654, 2001.
- [20] P. Mansky, Y. Liu, E. Huang, T. P. Russell, and C. Hawker, "Controlling polymer-surface interactions with random copolymer brushes," *Science*, vol. 275, no. 5305, pp. 1458–1460, 1997.
- [21] O. Prucker and J. Rühle, "Synthesis of poly(styrene) monolayers attached to high surface area silica gels through self-assembled monolayers of azo initiators," *Macromolecules*, vol. 31, no. 3, pp. 592–601, 1998.
- [22] O. Prucker and J. Rühle, "Mechanism of radical chain polymerizations initiated by azo compounds covalently bound to the surface of spherical particles," *Macromolecules*, vol. 31, no. 3, pp. 602–613, 1998.
- [23] E. Bourgeat-Lami and J. Lang, "Encapsulation of inorganic particles by dispersion polymerization in polar media 1. Silica nanoparticles encapsulated by polystyrene," *Journal of Colloid and Interface Science*, vol. 197, no. 2, pp. 293–308, 1998.
- [24] P. L. Kuo, N. J. Turro, C. M. Tseng, M. S. El-Aasser, and J. W. Vanderhoff, "Photoinitiated polymerization of styrene in microemulsions," *Macromolecules*, vol. 20, no. 6, pp. 1216–1221, 1987.
- [25] S. Atik and J. K. Thomas, "Photoinduced reactions in polymerized microemulsions," *Journal of the American Chemical Society*, vol. 105, no. 14, pp. 4515–4519, 1983.
- [26] N. J. Turro, M. F. Chow, C. J. Chung, and C. H. Tung, "Magnetic field and magnetic isotope effects on photoinduced emulsion polymerization," *Journal of the American Chemical Society*, vol. 105, no. 6, pp. 1572–1577, 1983.
- [27] N. J. Turro and K. S. Arora, "Magnetic effects on photoinduced emulsion polymerization. Effects of lanthanide ion addition," *Macromolecules*, vol. 19, no. 1, pp. 42–46, 1986.
- [28] M. G. Evans, M. Santappa, and N. Uri, "Photoinitiated free radical polymerization of vinyl compounds in aqueous solution," *Journal of Polymer Science*, vol. 7, no. 23, pp. 243–260, 1951.

- [29] H. Zhang, J. Wang, L. Li, Y. Song, M. Zhao, and X. Jian, "Synthesis of liquid polysilsequioxane resins and properties of cured films," *Thin Solid Films*, vol. 517, no. 2, pp. 857–862, 2008.
- [30] Z. X. Guo and J. Yu, "Grafting of dendritic polyethers onto nanometre silica surface," *Journal of Materials Chemistry*, vol. 12, no. 3, pp. 468–472, 2002.
- [31] A. Hartwig, M. Sebal, and M. Kleemeier, "Cross-linking of cationically polymerised epoxides by nanoparticles," *Polymer*, vol. 46, no. 7, pp. 2029–2039, 2005.

Research Article

Reinforcement of Natural Rubber with Core-Shell Structure Silica-Poly(Methyl Methacrylate) Nanoparticles

Qinghuang Wang,¹ Yongyue Luo,² Chunfang Feng,^{2,3} Zhifeng Yi,^{2,3}
Quanfang Qiu,² L. X. Kong,³ and Zheng Peng²

¹ State Engineering and Technology Research Center for Key Tropical Crops, Haikou 571101, China

² Chinese Agricultural Ministry Key Laboratory of Tropical Crop Product Processing, Agricultural Product Processing Research Institute, Chinese Academy of Tropical Agricultural Sciences, Zhanjiang 524001, China

³ Centre for Material and Fiber Innovation, Institute for Technology Research Innovation, Deakin University, Geelong, VIC 3217, Australia

Correspondence should be addressed to L. X. Kong, lingxue.kong@deakin.edu.au and Zheng Peng, zhengpeng8@yahoo.com

Received 18 March 2011; Revised 10 June 2011; Accepted 18 June 2011

Academic Editor: Aruna Ar Nanda

Copyright © 2012 Qinghuang Wang et al. This is an open access article distributed under the Creative Commons Attribution License, which permits unrestricted use, distribution, and reproduction in any medium, provided the original work is properly cited.

A highly performing natural rubber/silica (NR/SiO₂) nanocomposite with a SiO₂ loading of 2 wt% was prepared by combining similar dissolve mutually theory with latex compounding techniques. Before polymerization, double bonds were introduced onto the surface of the SiO₂ particles with the silane-coupling agent. The core-shell structure silica-poly(methyl methacrylate), SiO₂-PMMA, nanoparticles were formed by grafting polymerization of MMA on the surface of the modified SiO₂ particles via in situ emulsion, and then NR/SiO₂ nanocomposite was prepared by blending SiO₂-PMMA and PMMA-modified NR (NR-PMMA). The Fourier transform infrared spectroscopy results show that PMMA has been successfully introduced onto the surface of SiO₂, which can be well dispersed in NR matrix and present good interfacial adhesion with NR phase. Compared with those of pure NR, the thermal resistance and tensile properties of NR/SiO₂ nanocomposite are significantly improved.

1. Introduction

Recently, considerable efforts have been expended on the preparation of organic/inorganic nanocomposite materials [1, 2]. Inorganic nanoparticles possess small particle size, high surface area, as well as the quantum and surface effect, which make it possible for nanocomposites to perform more excellent physical and mechanical properties than conventional composites [3, 4]. Multifarious nanoscale fillers, including calcium carbonate [5], montmorillonite [6], carbon black [7], and aluminum oxide [8], have been reported in academic journals. Among them, nanosilica (SiO₂), an important member of inorganic nanofiller in composites preparation, is widely used in the field of organic/inorganic hybrid composites. Zhu et al. [9] prepared well-dispersed silica-poly(methyl methacrylate) (SiO₂-PMMA) nanoparticles by a suspension-dispersion-polymerization technique in

an aqueous system. Subsequently, SiO₂-PMMA nanoparticles were induced into PVC matrix, and results showed that the heat resistance, elongation at break, and tensile strength of PVC/SiO₂ composites were significantly improved. Also, Peng et al. prepared natural rubber/silica nanocomposites (NR/SiO₂) [10] and natural rubber/multiwalled carbon nanotubes composite [11] combining self-assembly and latex-compounding techniques. Obtained nanocomposites were perfectly strengthened, with increased thermal resistance and mechanical properties.

But on the other hand, as nanoscaled particles, nanosilica tend to the lowest energy state of bulk aggregation in polymer matrix because of large surface area and high surface energy, which in turn leads to structure flaws in the polymer matrix and interfere with the property of the whole product [12, 13]. In order to enhance interfacial adhesion between nanosilica and NR matrix and improve the dispersion of nanoparticles

in NR matrix, it is necessary to reinforce the compatibility between the organic matrix and the inorganic surface of nano-silica. Due to large numbers of hydroxy group on the surface of raw nanosilica [14, 15], its surface is easily compatible with polar polymers, such as PVA and PVC compared to the apolar matrix, natural rubber. According to traditional method, the most commonly used method to disperse nanosilica was the mixing process conducted in two-roll mill [16, 17]. Despite well-distributed polymer composite can be finally obtained, the contamination of fly ash and the side effect on the lung of individuals are difficult to be avoided during the preparation of composite in either the laboratory or factory. Also, this method possesses some other advantages, such as low energy cost and homogeneous dispersion of silica in NR matrix. Latex compounding, therefore, can reduce harmful situation mentioned above, and be more eco-friendly and low-polluted processing. However, in order to obtain homogeneous dispersion of polar nanosilica in apolar natural rubber latex, surface modification of nanoparticles is required. There has been numerous numbers of publications reported in this field, such as chemical coating using coupling agents [18–21] and physical coating using detergents [22] whereas rare researches are referred to the surface functionalization of nanosilica and dispersing process in natural rubber latex. In this paper, a novel method to prepare NR/SiO₂ nanocomposite will be reported. Well-dispersed core-shell SiO₂-PMMA nanoparticles were prepared by using MPS as bridge in aqueous solution. In addition, NR latex was modified by PMMA in emulsion system before mixing with core-shell nanoparticles via combining similar dissolve mutually theory and latex-compounding techniques. It is proved that this method is useful and core-shell SiO₂-PMMA nanoparticles are rarely reported in NR latex application, and we will systematically discuss the synthesizing process and also investigate the relationship between microstructure and macroproperties.

2. Experimental

2.1. Materials. Natural rubber latex (NRL) with a total solid content of 60% was obtained from Qianjin state farm (Guangdong, China). Silica nanoparticles (average diameter: 7 nm) were purchased from Sigma-Aldrich (Sigma-Aldrich, St. Louis, MO). Methyl methacrylate (MMA) and tert-butyl hydroperoxide were purchased from Sinopharm, Ltd. (Shanghai, China). 3-(trimethoxysilyl) propyl methacrylate (MPS) was brought from Guangzhou Chemical Reagent Co. (Guangdong, China). Potassium persulfate (KPS) and Tetraethylenepentamine were offered by Xilong Chemical Co. (Guangdong, China). All experiments were carried out with distilled water.

2.2. Preparation of the NR/SiO₂ Nanocomposite

2.2.1. Coupling Modification of Nanosilica. We modified the surface of SiO₂ particles with MPS. Firstly, MPS was hydrolyzed in 95% ethanol solution for 2 hours. Then a fixed amount of SiO₂ with 95% ethanol as solvent was treated with

an ultrasonic vibrator for 15 min. Finally, SiO₂ dispersion was dropped into hydrolyzed MPS with mechanical stir at 25°C for 5 hours, and its pH was adjusted to 10 with triethylamine [23]. The SiO₂/MPS dispersion was centrifuged followed by rinsing with ethanol for 3 times and then with distilled water for 2 times.

2.2.2. Copolymerization of MMA on the Surface of Nanosilica.

The surface-functionalized SiO₂ was dispersed in an aqueous system with MMA and sodium dodecyl sulfate (SDS) in order to obtain nano-silica colloid [24] which was mixed with an aqueous solution of initiator potassium persulfate (KPS), and then charged into a flask with mechanical stirring at 55°C for 5 hours. PMMA, as the shell, was grafted onto the surface of SiO₂/MPS due to the reaction of the vinyl groups between SiO₂/MPS and MMA.

2.2.3. Modification of NRL.

NRL was treated in an aqueous solution where MMA, oleic acid, and tert-butyl hydroperoxide were mixed accompanying gentle mechanical stir at room temperature for 2 hours. The colloid system was heated to 60°C, before dropping an aqueous solution of activating agent (tetraethylenepentamine), and then cooled to room temperature, finally NR-PMMA latex was obtained [25].

2.2.4. Synthesis of Nanocomposite.

The SiO₂-PMMA aqueous dispersion was dropped into a certain amount of NR-PMMA latex with a total solid content of 30% and the mixture was stirred for 24 hours, which was then dried to obtain NR/SiO₂ nanocomposite films. The loading of silica is 2 wt% in NR matrix.

2.3. Characterization.

A Perkin-Elmer Spectra GX-I FTIR spectroscopy (Perkin-Elmer, Fremont, CA) was used to investigate surface chemistry of SiO₂ after modification with a resolution of 4 cm⁻¹ in the transmission mode. The liquid SiO₂ were dragged up by copper network for transmission electron microscopy (TEM), and then were observed on a JEM-100CXII instrument (JEOL, Peabody, MA) with an accelerating voltage of 100 kV. The morphology of the nanocomposites was taken with a scanning electron micrographs (SEM), Philips XL30-EDAX instrument (Philips, Eindhoven, Netherlands), at an acceleration voltage of 10 kV. The cross-section of the samples was obtained by splitting bulk sample with liquid nitrogen treatment.

The dynamic-mechanical thermal analysis (DMTA) spectra were taken on rectangular specimens (20 × 4 × 0.1 mm) in tensile mode at a frequency of 5 Hz using a NETZSCH DMA 242C instrument (Germany), ranged from the temperature of -120°C to 50°C. Thermal decomposition of samples was performed with a Perkin-Elmer TGA-7 thermogravimetric analyzer (TGA); (Perkin-Elmer, Fremont, CA). The measurement of the samples (ca. 10 mg) was carried out in nitrogen from 50°C to 600°C at a heating rate of 10°C/min. Tensile test experiments were conducted on the instrument in compression model with a cross-head speed of 500 mm/min, and the sample length was 75 mm, the minimum width was 4 mm, and the thickness was 2 mm.

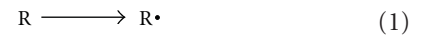
3. Results and Discussion

3.1. Mechanism of Preparing NR/SiO₂ Nanocomposite Process.

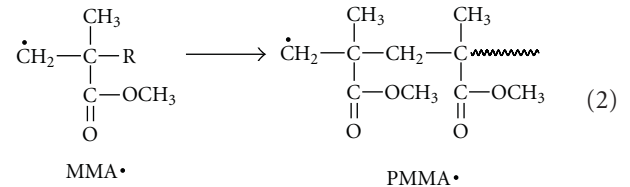
Figure 1 describes the scheme of the manufacturing process of NR/SiO₂ nanocomposite. There are three main steps in this process. The first step is to form core-shell SiO₂-PMMA nanoparticles. The silane-coupling agent MPS are hydrolyzed to form silanol groups which condense with hydroxyl groups on the surface of silica to form a covalent bond. Because of the grafted MPS, unsaturated double bond (C=C) is introduced onto the surface of silica nanoparticles [26]. When the silane-coupling agent grafted on the surface of SiO₂ counters an unsaturated functional group in MMA, the copolymerization between SiO₂/MPS and the copolymer PMMA will take place if there is an appropriate initiator. Eventually the core-shell SiO₂-PMMA nanoparticles are successfully obtained.

The second process is to prepare NR-PMMA latex. The modification mechanism is as follows [27].

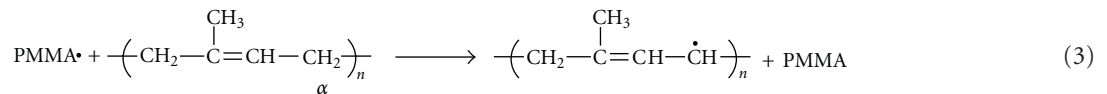
(1) The initiators decompose to generate free radical:



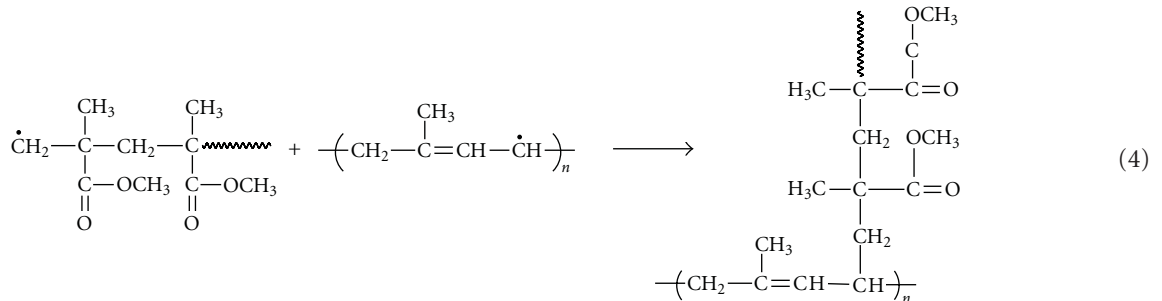
(2) MMA monomers are initiated to polymerize by free radical R•.



(3) PMMA chain growth process is accompanied with the radical transferring to NR macromolecule.



(4) The combination of two radicals terminates the entire reaction.



The last stage is to blend core-shell SiO₂-PMMA nanoparticles and NR-PMMA via similar dissolve mutually theory. Compared with the other techniques [28, 29], the above-mentioned process is more convenient and effective in preparing NR/SiO₂ nanocomposite.

3.2. Characterization of Core-Shell

SiO₂-PMMA Nanoparticles

3.2.1. FTIR Study. After the formation of core-shell SiO₂-PMMA nanoparticles, either chemical reaction or physical adsorption would be characterized in the FTIR spectra. Therefore, before the measurement of FTIR, all the SiO₂

nanoparticles modified with MMA have been extracted in acetone solution for 72 hours in order to eliminate ungrafted PMMA.

Figure 2 displays the infrared spectra of the eluate and pure acetone solution. It can be seen that the peak at 1730 cm⁻¹ (Figure 2(A)) is assigned to C=O stretching vibration of PMMA while after 72 hours extracting, this peak disappears and only C=O stretching vibration of acetone at 1715 cm⁻¹ could be seen (Figure 2(B)). It can be proved that after 72 hours extracting, there is no redundant PMMA absorbed physically on SiO₂-PMMA nanoparticles. Subsequently, rinsed solid SiO₂-PMMA and unmodified SiO₂ were measured through FTIR. It can be seen from

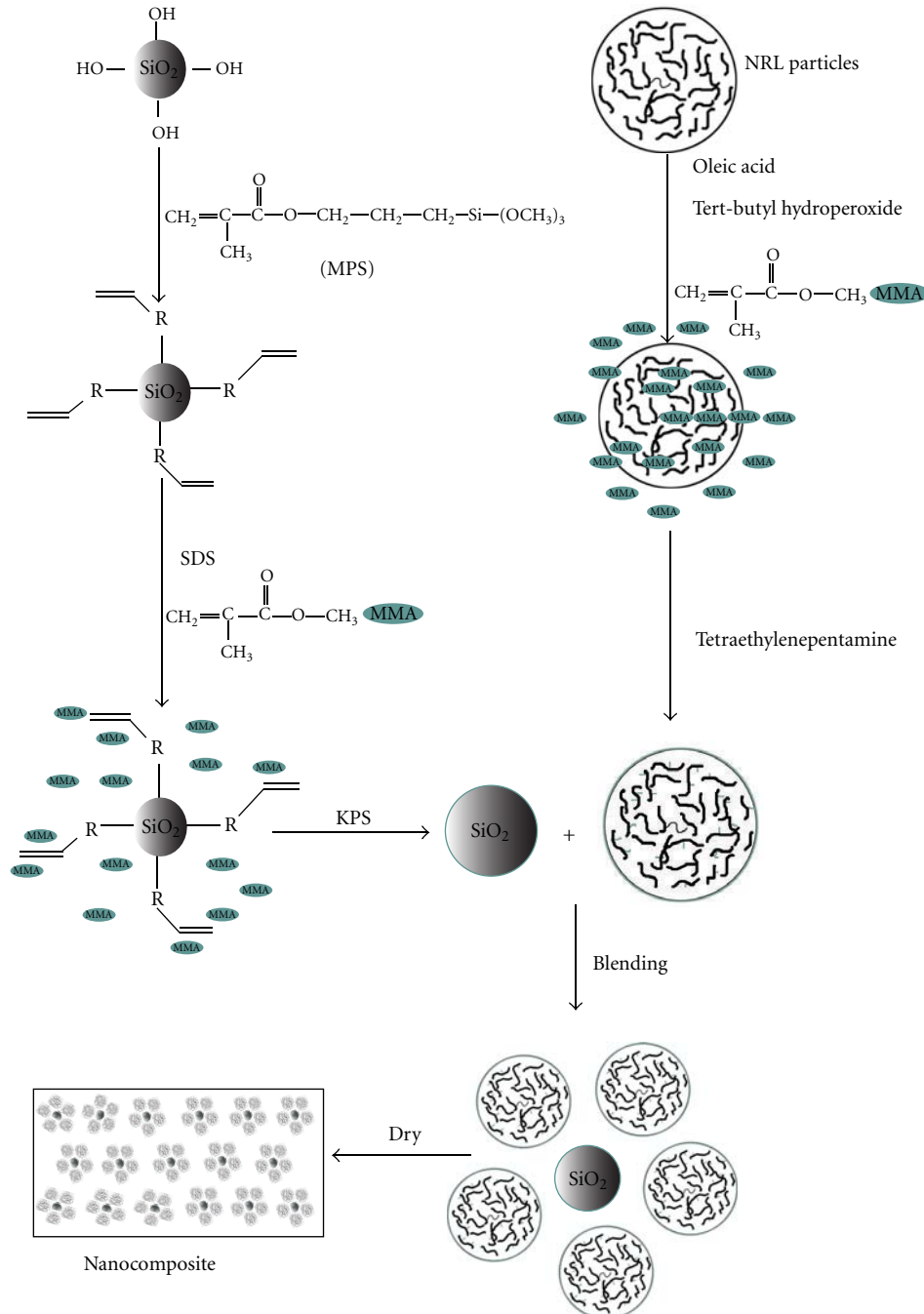


FIGURE 1: Manufacturing process of NR/SiO₂ nanocomposite.

Figure 3 that the adsorption peak at 1697 cm^{-1} assigned to the C=O functional groups (Figure 3(B)) does not appear in Figure 3(A), which indicates that MPS has been successfully grafted on the surface of SiO₂ [30] and SiO₂ and MPS are linked with covalent bonds. Therefore, it is possible for MMA to graft onto the modified SiO₂ nanoparticles. As can be seen from Figure 3(C) that the absorption peak at 1730 cm^{-1} assigned to the vibration absorption of C=O is obvious, accompanying with one less pronounced peak at 2975 cm^{-1} corresponding to CH₃ groups of PMMA. All the results obtained from FTIR spectra confirm that PMMA successfully

grafted onto the SiO₂ modified by MPS through chemical bonds rather than simply physical adsorption.

3.2.2. TEM Observation. It is obvious that unmodified SiO₂ nanoparticles are aggregated together and the diameter ranges from 10 nm to 30 nm (Figure 4(a)) whilst because of the introduction of PMMA, nanoparticles (SiO₂/MMA = 1:0.3) indicate well-dispersed morphology (Figure 4(b)). However, after being grafted by PMMA, dispersibility of SiO₂ is improved (Figure 4(b)). It can be also seen from Figure 4(b) that single nanoparticle with a diameter around

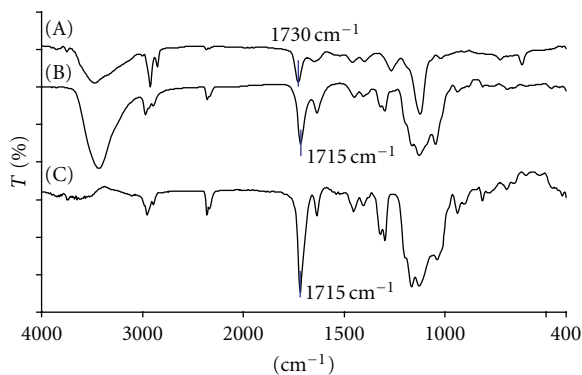


FIGURE 2: Infrared spectra of SiO_2 -PMMA soxhlet extraction solution. (A) The first eluate; (B) the second eluate; (C) pure acetone solution.

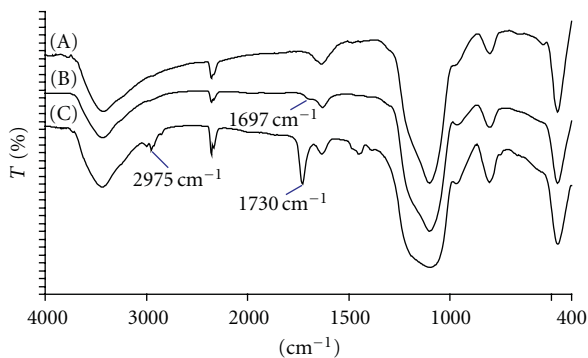


FIGURE 3: Infrared spectra of nanosilica, (A) unmodified SiO_2 ; (B) SiO_2 -MPS; (C) SiO_2 -PMMA.

40–60 nm can be clearly observed, which is 30 nm thicker than unmodified SiO_2 particles. This illuminates that the core, SiO_2 nanoparticles, is successfully coated by the shell, PMMA, and the thickness of PMMA shell is about 25–35 nm. It can also be observed in the SEM images (Figure 5) where the core-shell SiO_2 -PMMA nanoparticles are evenly dispersed throughout NR matrix. However, when the ratio of SiO_2 /MMA reaches to 1:3, the sphere morphology is out of order (Figure 4(c)) due to the increasing prevalence of PMMA homopolymerization, and PMMA will physically be absorbed on the surface of nanosilica. Meanwhile, the aggregation of nano- SiO_2 deteriorates, and the diameter of the SiO_2 clusters becomes much bigger compared with Figure 4(b). Therefore, from the results above the suitable SiO_2 /MMA ratio is 1:0.3, which is proved to be the proper grafting rate through large amounts of experimental work.

3.3. Characterization of NR/ SiO_2 Nanocomposites

3.3.1. SEM Observation. In recent work, NR/ SiO_2 nanocomposite was prepared with a constant mixture rate (NR/ SiO_2 = 98/2). Because SiO_2 has been surface-functionalized with MPS and MMA, the compatibility is improved between SiO_2 nanoparticles and NR matrix, and, moreover, SiO_2 -PMMA nanoparticles with an average size ranged from 60 nm to

100 nm are uniformly dispersed in the matrix as individual spherical core-shell structure (Figure 5(c)). Whereas unmodified SiO_2 in NR matrix (Figures 5(a) and 5(b)) aggregate significantly and the size of the SiO_2 clusters reaches to more than 200 nm. These results illustrate that the excellent compatibility between the SiO_2 -PMMA and NR-PMMA enhances the interaction between SiO_2 and NR, and thus improves the adhesion and morphological structure of NR/ SiO_2 nanocomposites. The preparation method of polymer/ SiO_2 composites has been widely reported, such as melt compounding [31] and other physical blending [32], however, the process presented in this paper possesses significant advantages, for instance, the compatibility with NR is excellent and the size of SiO_2 is approximately 80 nm.

3.3.2. Dynamic Thermal Mechanical Analysis. Dynamic thermal mechanical analysis (DTMA) can characterize the reaction between polymer molecular chains and inorganic particles and the transformation from glass state to viscoelastic state. It can be seen from Figure 6 that peaks of curves move to the direction of high temperature with the enhancement of compatibility which can be seen from SEM images (Figure 5). The glass-transition temperature (T_g) can be calculated from the peak of $\tan\delta$ -T curve. T_g of NR-PMMA/ SiO_2 -PMMA is obviously higher than that of the others (Figure 6), which reaches to -48°C . It could be attributed to the well-dispersed core-shell SiO_2 -PMMA nanoparticles in NR-PMMA matrix. PMMA play an important role in the molecular interaction between SiO_2 and NR chains, declining the thermal motion of the NR molecule [33]. Therefore, the adapting temperature range of rubber products has been expanded with the loading of 2 wt% core-shell SiO_2 -PMMA nanoparticles.

In addition, NR-PMMA composite filled with core-shell SiO_2 -PMMA nanoparticles has a higher storage modulus than the others at the temperature ranged from -100°C to -50°C (Figure 7). When the temperature is below T_g , the core-shell SiO_2 -PMMA nanocomposites possess a high storage modulus, which is caused by introducing rigid nanosilica particles [34]. The increasing storage modulus attributes to the friction between the core-shell SiO_2 -PMMA nanoparticles and the NR-PMMA molecules when the nanosilica particles are thoroughly dispersed in the NR matrix.

3.3.3. The Thermal Gravimetric Analysis. All samples are measured in nitrogen environment, which means no oxygenolysis of polymer molecules and that it well proves the effect of the bridge molecule, PMMA. Adding SiO_2 -PMMA nanoparticles can enhance the thermal stability of composites. The main thermal decomposition of NR matrix is at about 360°C (Figure 8) where C–C chain bonds ruptured and hydrogen transferred [35]. The degradation curve of NR-PMMA/ SiO_2 -PMMA is slightly shifted to a higher temperature, compared with the other samples, due to the intertwining between one PMMA chain on the surface of nanosilica and another PMMA chain grafted on NR molecules.

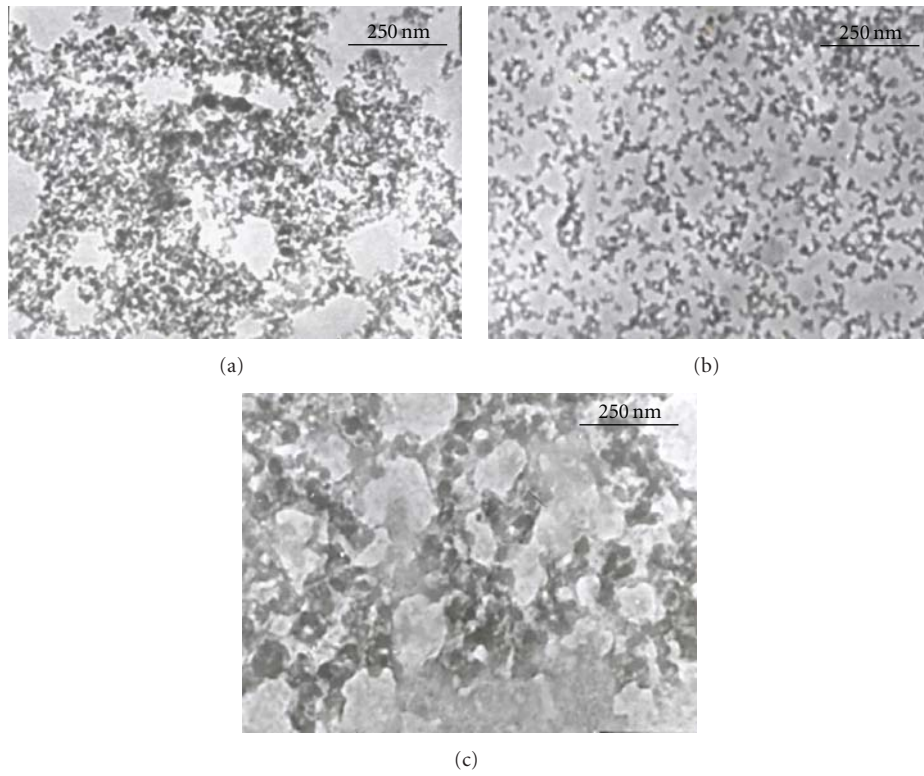


FIGURE 4: TEM micrographs of SiO₂ nanoparticles in water. (a) Unmodified SiO₂; (b) SiO₂-PMMA(SiO₂: MMA = 1 : 0.3); (c) SiO₂-PMMA (SiO₂: MMA = 1 : 3).

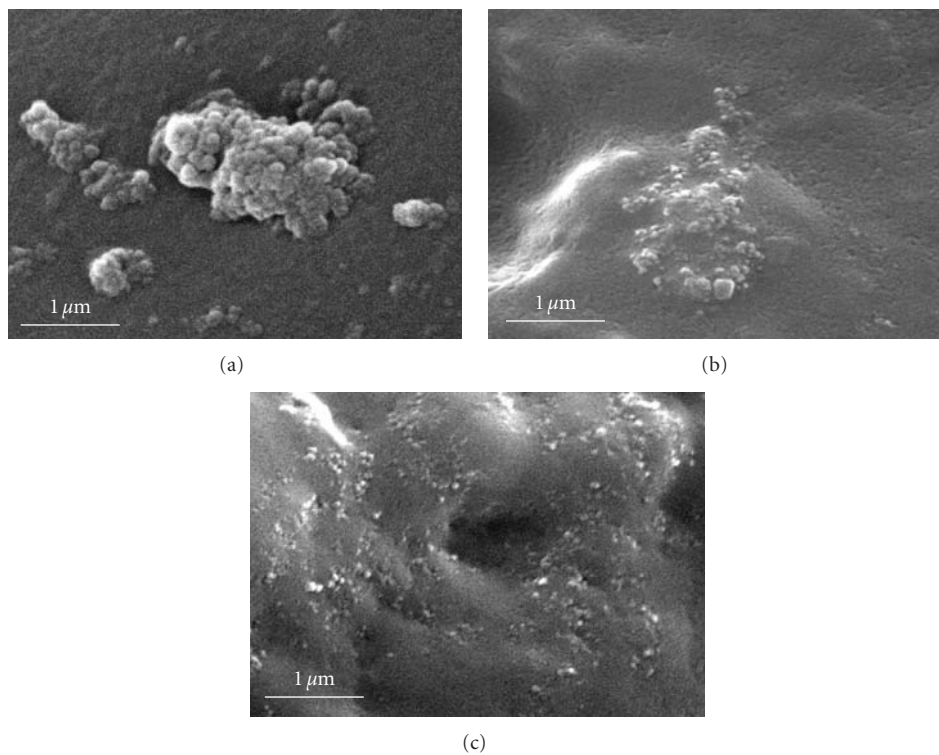


FIGURE 5: SEM micrographs of nanocomposites. (a) NR/SiO₂; (b) NR-PMMA/SiO₂; (c) NR-PMMA/SiO₂-PMMA.

TABLE 1: Tensile properties of pure NR and its nanocomposites ($\text{SiO}_2/\text{NR} = 2/100$ w/w).

Samples	NR	NR-PMMA	NR-PMMA/SiO ₂	NR-PMMA/SiO ₂ -PMMA
Tensile strength/MPa	6.99	7.23	8.95	10.65
Elongation at break/%	835	823	772	773
Tensile modulus/MPa				
300% elongation	0.92	0.82	1.22	1.95
500% elongation	1.00	0.94	1.46	2.32
700% elongation	1.58	2.06	2.96	3.37

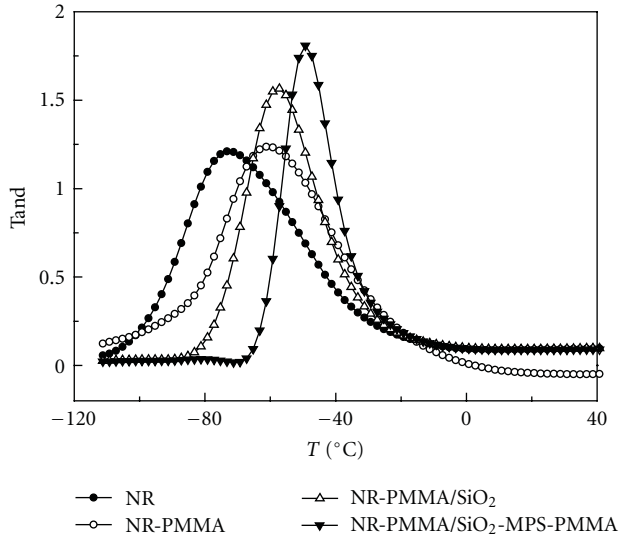


FIGURE 6: The loss factor as a function of temperature for pure NR and its nanocomposites.

During thermal decomposition, there are three main degraded temperatures, onset temperature (T_o), peak temperature (T_p), and flow temperature (T_f). Those of the NR-PMMA/SiO₂-PMMA nanocomposites increase by 5.4°C, 4.9°C and 5.7°C, respectively, in comparison with those of the pure NR. Incorporating with the distribution observed from SEM, the thermal stability depends on the distribution of SiO₂ nanoparticles. The more homogeneously the SiO₂ nanoparticles disperse in NR matrix, the stronger the reaction between the molecules is [36]. Because the decomposition has been slowed down, the ageing resistance of nanocomposite is improved compared to the pure NR. This from another aspect supports the feasibility and efficiency of similar dissolve mutually theory in the preparation of NR/silica composite.

3.3.4. Tensile Property. The tensile performance has been investigated in detail among different samples, namely, NR, NR/PMMA, NR-PMMA/SiO₂, and NR-PMMA/SiO₂-PMMA. Obviously, with the improvement of modification and the introduction of nanosilica, the tensile strength as well as tensile modulus at different elongations is increasingly high. It can be seen from Table 1 that the tensile strength increases by 3.66 MPa from 6.99 MPa (NR) to 10.65 MPa (NR-PMMA/SiO₂-PMMA). Since PMMA is grafted both on

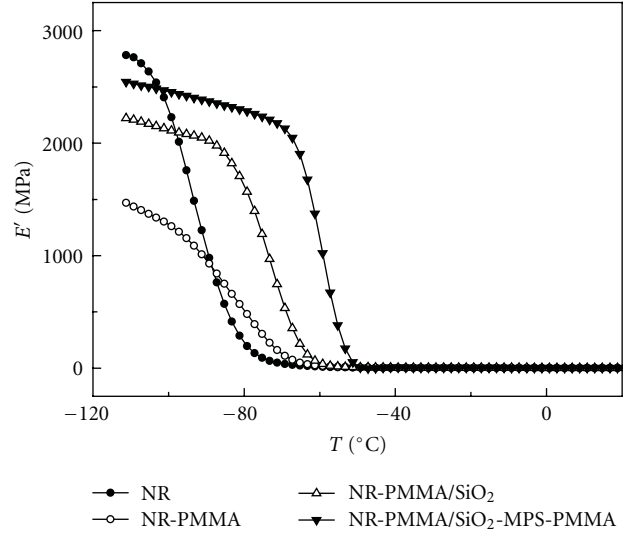


FIGURE 7: The storage modulus as a function of temperature for pure NR and its nanocomposites.

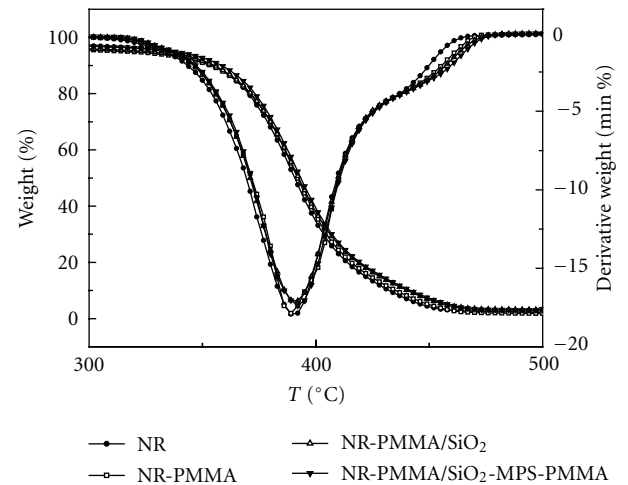


FIGURE 8: TG/DTG curves of pure NR and its nanocomposites in nitrogen.

SiO₂ and NR, its molecule chains twist together via similar dissolve mutually theory, reinforcing the interaction between nano-SiO₂ and NR matrix and hindering the movement of NR macromolecule chains [37]. That is to say that PMMA as a bridge between the inorganic nanoparticles and

polymer matrix improve the mutual compatibility which in turn results in excellent mechanical property. In addition, comparing the tensile strength between NR-PMMA and NR-PMMA/SiO₂, nanosilica without grafting PMMA on its surface can also reinforce the tensile property, from 7.23 to 8.95 MPa.

4. Conclusion

A novel methodology, similar dissolve mutually theory, is introduced to prepare NR/SiO₂ nanocomposite in this paper. The core-shell SiO₂-PMMA particles ranged from 60 nm to 100 nm are well dispersed in latex at a suitable SiO₂/MMA ratio of 1 : 0.3, and the thickness of PMMA shell is about 25–35 nm. Moreover, the dispersion of core-shell SiO₂-PMMA nanoparticles has been improved by grafting PMMA on both nano-SiO₂ and NR molecule chains. Based on the excellent dispersion of SiO₂-PMMA nanoparticles, T_g and thermal ageing resistances of nanocomposite are considerably enhanced. Meanwhile, the tensile strength increases by 3.66 MPa compared with the pure NR. The recent research is merely focusing on 2 wt% loading of nanosilica, and further work will be extended into different addition of nanosilica.

Acknowledgments

The financial support from the Natural Science Foundation of China (Contract Grant no. 50763006), Ministry of Science and Technology R & D research institutes special fund (Contract Grant no. 2008EG134285) and 973 Program special fund (Contract Grant no. 2010CB635109) are gratefully acknowledged.

References

- [1] L. Qi and S. J. Dong, "Organic/inorganic nanocomposite polymer electrolyte," *Chinese Chemical Letters*, vol. 18, no. 2, pp. 185–188, 2007.
- [2] W. E. Mahmoud, "A novel photodiode made of hybrid organic/inorganic nanocomposite," *Journal of Physics D*, vol. 42, no. 15, Article ID 155502, 2009.
- [3] J. P. Salvetat, S. Bhattacharyya, and R. B. Pipes, "Progress on mechanics of carbon nanotubes and derived materials," *Journal of Nanoscience and Nanotechnology*, vol. 6, no. 7, pp. 1857–1882, 2006.
- [4] Y. Xie, C. A. S. Hill, Z. Xiao, H. Miltitz, and C. Mai, "Silane coupling agents used for natural fiber/polymer composites: a review," *Composites Part A*, vol. 41, no. 7, pp. 806–819, 2010.
- [5] I. Kemal, A. Whittle, R. Burford, T. Vodenitcharova, and M. Hoffman, "Toughening of unmodified polyvinylchloride through the addition of nanoparticulate calcium carbonate," *Polymer*, vol. 50, no. 16, pp. 4066–4079, 2009.
- [6] S. Habibi, A. Rashidi, S. Bazgir, A. A. Katbab, and M. Montazer, "Preparation and flame retardancy of poly(ethylene terephthalate)/ montmorillonite nanocomposites," *Asian Journal of Chemistry*, vol. 21, no. 6, pp. 4881–4888, 2009.
- [7] R. Nakason, W. Pechurai, K. Sahakaro, and A. Kaesaman, "Rheological, thermal, and curing properties of natural rubber-g-poly(methyl methacrylate)," *Journal of Applied Polymer Science*, vol. 99, no. 4, pp. 1600–1614, 2006.
- [8] K. Balani, S. P. Harimkar, A. Keshri, Y. Chen, N. B. Dahotre, and A. Agarwal, "Multiscale wear of plasma-sprayed carbon-nanotube-reinforced aluminum oxide nanocomposite coating," *Acta Materialia*, vol. 56, no. 20, pp. 5984–5994, 2008.
- [9] A. Zhu, Z. Shi, A. Cai, F. Zhao, and T. Liao, "Synthesis of core-shell PMMA-SiO₂ nanoparticles with suspension-dispersion-polymerization in an aqueous system and its effect on mechanical properties of PVC composites," *Polymer Testing*, vol. 27, no. 5, pp. 540–547, 2008.
- [10] Z. Peng, L. X. Kong, S. D. Li, Y. Chen, and M. F. Huang, "Self-assembled natural rubber/silica nanocomposites: its preparation and characterization," *Composites Science and Technology*, vol. 67, no. 15–16, pp. 3130–3139, 2007.
- [11] Z. Peng, C. Feng, Y. Luo, Y. Li, and L. X. Kong, "Self-assembled natural rubber/multi-walled carbon nanotube composites using latex compounding techniques," *Carbon*, vol. 48, no. 15, pp. 4497–4503, 2010.
- [12] C. Charitidis and S. Logothetidis, "Nanoscale effects on the nanomechanical properties of multifunctional materials," *Computational Materials Science*, vol. 33, no. 1–3, pp. 296–302, 2005.
- [13] J. Oberdisse, "Aggregation of colloidal nanoparticles in polymer matrices," *Soft Matter*, vol. 2, no. 1, pp. 29–36, 2006.
- [14] Z. Y. Shen, L. Y. Li, Y. Li, and C. C. Wang, "Fabrication of hydroxyl group modified monodispersed hybrid silica particles and the h-SiO₂/TiO₂ core/shell microspheres as high performance photocatalyst for dye degradation," *Journal of Colloid and Interface Science*, vol. 354, no. 1, pp. 196–201, 2011.
- [15] W. Xueqin, Z. Chunxi, J. Jing, S. Ningfang, and X. Hongjie, "Radiation-induced attenuation effect in hydroxyl-rich pure-silica-core photonic crystal fiber," *Optik*. In press.
- [16] S. Prasertsri and N. Rattanasom, "Mechanical and damping properties of silica/natural rubber composites prepared from latex system," *Polymer Testing*, vol. 30, no. 5, pp. 515–526, 2011.
- [17] L. N. Carli, C. R. Roncato, A. Zanchet et al., "Characterization of natural rubber nanocomposites filled with organoclay as a substitute for silica obtained by the conventional two-roll mill method," *Applied Clay Science*, vol. 52, no. 1–2, pp. 56–61, 2011.
- [18] J. P. Matinlinna, L. V. J. Lassila, and P. K. Vallittu, "The effect of five silane coupling agents on the bond strength of a luting cement to a silica-coated titanium," *Dental Materials*, vol. 23, no. 9, pp. 1173–1180, 2007.
- [19] C. Cherkouk, L. Rebohle, W. Skorupa, T. Strache, H. Reuther, and M. Helm, "Spraying spin coating silanization at room temperature of a SiO₂ surface for silicon-based integrated light emitters," *Journal of Colloid and Interface Science*, vol. 337, no. 2, pp. 375–380, 2009.
- [20] X. K. Ma, N. H. Lee, H. J. Oh et al., "Surface modification and characterization of highly dispersed silica nanoparticles by a cationic surfactant," *Colloids and Surfaces A*, vol. 358, no. 1–3, pp. 172–176, 2010.
- [21] A. M. Kartal and C. Erkey, "Surface modification of silica aerogels by hexamethyldisilazane-carbon dioxide mixtures and their phase behavior," *The Journal of Supercritical Fluids*, vol. 53, no. 1–3, pp. 115–120, 2010.
- [22] F. Ebihara and S. Watano, "Development of a novel granular detergent by inorganic solution binder," *Journal of Chemical Engineering of Japan*, vol. 35, no. 12, pp. 1263–1269, 2002.
- [23] H. Yan, G. Tian, K. Sun, and Y. Zhang, "Effect of silane coupling agent on the polymer-filler interaction and mechanical properties of silica-filled NR," *Journal of Polymer Science, Part B*, vol. 43, no. 5, pp. 573–584, 2005.

- [24] N. Sombatsompop, E. Wimolmala, and T. Markpin, "Fly-ash particles and precipitated silica as fillers in rubbers. II. Effects of silica content and Si69-treatment in natural rubber/styrene-butadiene rubber vulcanizates," *Journal of Applied Polymer Science*, vol. 104, no. 5, pp. 3396–3405, 2007.
- [25] S. Ostad-Movahed, K. A. Yasin, A. Ansarifar, M. Song, and S. Hameed, "Comparing effects of silanized silica nanofiller on the crosslinking and mechanical properties of natural rubber and synthetic polyisoprene," *Journal of Applied Polymer Science*, vol. 109, no. 2, pp. 869–881, 2008.
- [26] L. Bokobza and J. P. Chauvin, "Reinforcement of natural rubber: use of in situ generated silicas and nanofibres of sepiolite," *Polymer*, vol. 46, no. 12, pp. 4144–4151, 2005.
- [27] L. Bokobza and O. Rapoport, "Silica and carbon black reinforcement of natural rubber," *Macromolecular Symposia*, vol. 194, no. 1, pp. 125–134, 2003.
- [28] S. Varghese and J. Karger-Kocsis, "Natural rubber-based nanocomposites by latex compounding with layered silicates," *Polymer*, vol. 44, no. 17, pp. 4921–4927, 2003.
- [29] R. Magaraphan, W. Thajjaroen, and R. Lim-Ochakun, "Structure and properties of natural rubber and modified montmorillonite nanocomposites," *Rubber Chemistry and Technology*, vol. 76, no. 2, pp. 406–418, 2003.
- [30] R. Y. Hong, H. P. Fu, Y. J. Zhang et al., "Surface-modified silica nanoparticles for reinforcement of PMMA," *Journal of Applied Polymer Science*, vol. 105, no. 4, pp. 2176–2184, 2007.
- [31] M. Tanahashi, M. Hirose, Y. Watanabe, J. C. Lee, and K. Takeda, "Silica/perfluoropolymer nanocomposites fabricated by direct melt-compounding: a novel method without surface modification on nano-silica," *Journal of Nanoscience and Nanotechnology*, vol. 7, no. 7, pp. 2433–2442, 2007.
- [32] J. J. Chen, C. F. Zhu, H. T. Deng, Z. N. Qin, and Y. Q. Bai, "Preparation and characterization of the waterborne polyurethane modified with nanosilica," *Journal of Polymer Research*, vol. 16, no. 4, pp. 375–380, 2009.
- [33] Z. Peng, L. X. Kong, and S. D. Li, "Dynamic mechanical analysis of polyvinylalcohol/silica nanocomposite," *Synthetic Metals*, vol. 152, no. 1–3, pp. 25–28, 2005.
- [34] G. Sui, W. H. Zhong, X. P. Yang, Y. H. Yu, and S. H. Zhao, "Preparation and properties of natural rubber composites reinforced with pretreated carbon nanotubes," *Polymers for Advanced Technologies*, vol. 19, no. 11, pp. 1543–1549, 2008.
- [35] Z. Peng and L. X. Kong, "A thermal degradation mechanism of polyvinyl alcohol/silica nanocomposites," *Polymer Degradation and Stability*, vol. 92, no. 6, pp. 1061–1071, 2007.
- [36] R. Y. Hong, J. Z. Qian, and J. X. Cao, "Synthesis and characterization of PMMA grafted ZnO nanoparticles," *Powder Technology*, vol. 163, no. 3, pp. 160–168, 2006.
- [37] R. Hong, T. Pan, and H. Fu, "On the silica/PMMA nanocomposites," *Advanced Fibers and Polymer Materials*, vol. 10, pp. 19–27, 2005.

Research Article

Improvement in Comprehensive Properties of Poly(Methyl Methacrylate)-Based Gel Polymer Electrolyte by a Core-Shell Poly(Methyl Methacrylate)-Grafted Ordered Mesoporous Silica

Lixin Xu, Feng Xu, Feng Chen, Jintao Yang, and Mingqiang Zhong

College of Chemical Engineering and Materials Science, Zhejiang University of Technology, No. 18, Chaowang Road, 6th Zone, Chaohui, Hangzhou 310014, China

Correspondence should be addressed to Mingqiang Zhong, zhongmingqiang@hotmail.com

Received 2 March 2011; Accepted 7 April 2011

Academic Editor: Sherine Obare

Copyright © 2012 Lixin Xu et al. This is an open access article distributed under the Creative Commons Attribution License, which permits unrestricted use, distribution, and reproduction in any medium, provided the original work is properly cited.

A novel strategy, herein, is demonstrated for improving comprehensive properties of poly (methyl methacrylate)(PMMA)-based gel polymer electrolyte (GPE) with a core-shell PMMA-grafted ordered mesoporous silica (OMS-g-PMMA). The OMS-g-PMMA was synthesized by surface-initiated atom transfer radical polymerization of methyl methacrylate from the exterior surface of OMS particle. A series of PMMA-based GPE membranes, filled with the OMS-g-PMMA of different contents, were further prepared by solution casting technique. The OMS-g-PMMA was confirmed to possess regular core-shell structure, in which a PMMA shell is chemically grafted to the exterior surface of silica core remaining intact mesoporous characteristics. Compared to the bare OMS, the OMS-g-PMMA is found to more effectively improve the comprehensive properties of PMMA-based GPE including ionic conductivity, thermal stability, and mechanical properties as well. For the PMMA-based GPE filled with 15 phr OMS-g-PMMA, the ionic conductivity at 25°C reaches $1.59 \times 10^{-4} \text{ S} \cdot \text{cm}^{-1}$, which is higher by nearly two orders than that of the corresponding filler-free parent GPE. Meanwhile, the tensile strength and Young's modulus increase by 2.39 and 2.41 times, respectively, with an improvement in glass-transition temperature (T_g) about 10°C. The excellent comprehensive properties make the PMMA-based GPE filled with OMS-g-PMMA as potential candidate for electrochemical devices.

1. Introduction

Polymer electrolytes with excellent comprehensive properties have been attracting considerable attention in recent years with increasing demands for safe, lightweight lithium ion batteries, and various electrochemical devices of high performance. A great number of strategies, so far, have been explored for optimizing properties of polymer electrolytes, typically such as modification by adding plasticizers [1–5], and inorganic fillers [6–10]. Among them, impregnating plasticizer into polymer matrix to form gel polymer electrolyte (GPE) is one of the widely adopted approaches, since GPE combines the advantages of liquid electrolytes with higher ionic conductivity and solid electrolytes without leakage [11]. Nevertheless, GPE usually exhibits poor mechanical properties and thermal instability owing to the existence of plasticizer, which is the major hindrance to their

various practical applications. Although many methods have been successfully demonstrated for improving certain single property of GPE, it is still a challenge to develop GPE with excellent comprehensive performance including higher ionic conductivity, better mechanical properties and improved thermal stability as well.

One of the preferable solutions to above challenge is to incorporate inorganic nanosized fillers, such as SiO_2 [3, 7, 8], Al_2O_3 [6, 12], TiO_2 [6, 13], and layered clays [11], into GPE to form nanocomposite GPE (NGPE). It has been reported that the introduction of some inorganic nanosized fillers could lead to an improvement both in ionic conductivity and in other properties including mechanical strength and thermal stability [3, 11, 12]. The role of inorganic nanosized fillers in improving ionic conductivity of GPE is usually attributed to the Lewis acid-base interaction between the polar surface of fillers and ionic species, which yields more

mobile ion species, and thus leads to an improvement in ionic conductivity [14, 15]. In addition, some surface groups of inorganic nanosized fillers may provide physical cross-linking centers [16], and thus can improve, to an extent, the mechanical properties and thermal stability of GPE. Obviously, it is of great importance for NGPE to ensure a homogeneous dispersion of inorganic nanosized fillers in matrix for the above roles depend largely on the particle size and surface status of fillers. However, aggregation is usually inevitable in polymer matrix for the bare inorganic nanosized fillers due to their higher specific surface area and poor interfacial compatibilization with polymer matrix. Although the dispersibility of inorganic nanosized fillers in polymer matrix could be improved by surface modification with organic moieties such as coupling agent or polymer, the modified surface status of fillers usually leads to the dissociation of Lewis acid-base complex between the surface of fillers and ionic species, which is unfavorable to the improvement in properties of GPE.

We herein explore a novel strategy for improving comprehensive properties of poly(methyl methacrylate) (PMMA)-based GPE by using a core-shell PMMA-grafted ordered mesoporous silica (OMS-g-PMMA) as filler. The OMS-g-PMMA possesses a PMMA shell, which is chemically grafted to the exterior surface of ordered mesoporous silica (OMS) as a core remaining intact mesoporous structure. The PMMA shell is expected to greatly improve the interfacial interaction between the OMS and PMMA matrix, and thus to impart the modified GPE with highly improved mechanical properties and thermal stability. Moreover, the silica core has ordered and tunable pore channels with larger surface area and abundant surface $-OH$, which is beneficial to the formation of Lewis acid-base interactions between fillers-ions and thus to the improvement in ionic conductivity of GPE. Although a large volume of research papers on application of OMS as fillers in composite polymer electrolyte (CPE) [10, 17–21] are available, researches related to the effect of core-shell polymer-grafted OMS hybrid particle as fillers in GPE are still scarce. In this research, the OMS-g-PMMA was synthesized by surface-initiated atom transfer radical polymerization (ATRP) of methyl methacrylate from the exterior surface of OMS particle and the PMMA-based GPE was prepared by solution casting technique using the OMS-g-PMMA as filler, $LiClO_4$ as salt and propylene carbonate (PC) as plasticizer. The structure of the OMS-g-PMMA was characterized and the role of it in improving comprehensive properties of PMMA-based GPE was assessed.

2. Experimental Section

2.1. Materials. Propylene carbonate (PC, >99.5%) and 2-bromoisobutyryl bromide (>98%) were purchased from Acros Organics. 3-Aminopropyltriethoxysilane (APTEOS, >98%) was supplied from J&K Chemical Ltd. $CuBr$ (>98%) was obtained from Strem Chemicals Inc. N,N,N',N'' -pentamethyl-diethylenetriamine (PMDETA, >98%) was from Tokyo Chemical Industry Co., Ltd. Cetyltrimethy-

lammonium bromide (CTAB, analytical grade) was purchased from Shanghai Bo'ao Biological Technology Co., Ltd. Tetraethyl orthosilicate (TEOS, analytical grade) and triethylamine (>98%) was from Shanghai Chemical Reagent Purchase and Supply Wulian Chemical Factory. $LiClO_4$ was supplied from Aladin Chemical Reagent Inc. of Shanghai, China. Poly(methyl methacrylate) (PMMA) as a matrix was obtained from Zhenjiang Qimei Chemical Industry Co., Ltd. All above reagents/materials were used as received. Methyl methacrylate (MMA, analytical grade) was purchased from Quzhou Juhua Chemical Reagents Ltd. and purified by distillation under reduced pressure prior to use.

2.2. Synthesis of Core-Shell OMS-g-PMMA Particles. The strategy for synthesizing core-shell OMS-g-PMMA is schematically illustrated in Figure 1. To synthesize the OMS containing template (*t* OMS), 1.0 g CTAB as a template was first dissolved in 500 mL deionized water, and then, 4 mL NaOH aqueous solution (2 M) was added. The solution was heated to 80°C upon stirring and subsequently 20 mL TEOS was added dropwise within 0.5 h. The reaction was further lasted at 80°C for 4 h and a white suspension was gradually formed. The suspension was filtrated and the resulting precipitate was washed thoroughly with methanol, followed by drying at ambient temperature for 8 h in vacuum to give the *t* OMS.

The resulting *t* OMS was subsequently modified with a coupling agent, APTEOS, to give the amine group-functionalized *t* OMS (*t* OMS- NH_2). 4.0 g *t* OMS was dispersed in 600 mL toluene containing 10.9 g APTEOS by sonication for 1 h in a dried 1000 mL flask. The reaction was lasted for 24 h under reflux upon stirring. The solid product was collected by centrifugation and washed with methanol (40 mL/time) for 2 times, followed by drying at 50°C for 8 h in vacuum to give the *t* OMS- NH_2 .

The ATRP initiator, 2-bromoisobutyryl bromide, was further used to react with the *t* OMS- NH_2 to give the ATRP initiator-immobilized *t* OMS (*t* OMS-Br). 2.0 g *t* OMS- NH_2 was dispersed in 300 mL anhydrous dichloromethane containing 2% triethylamine (V/V) by sonication in a dried 500 mL schlenk bottle. 20 mL 2-bromoisobutyryl bromide was subsequently added dropwise within 3 h under N_2 protection at 0°C. The reaction was lasted at r.t. for 30 h, the resulting suspension was centrifuged, and the solid product was thoroughly washed with deionized water, acetone, and toluene, in sequence, followed by drying at r.t. for 8 h in vacuum to give the *t* OMS-Br. The CTAB as a template contained in the *t* OMS-Br was further removed by an extraction procedure with acidic ethanol and the OMS-Br without containing template was finally collected.

A typical ATRP procedure was performed to prepare the OMS-g-PMMA. 0.50 g dried OMS-Br, 0.03 g $CuBr$, 1.0 mL PMDETA, 10.0 mL anhydrous toluene, and 5.0 mL MMA were added into a dried 100 mL schlenk bottle. The mixture was degassed through three freeze-pump-thaw cycles and finally filled with N_2 atmosphere. The reaction was subsequently carried out at 80°C for 24 h under N_2 protection. The solid product was obtained by centrifuging the suspension and was washed thoroughly with toluene and methanol,

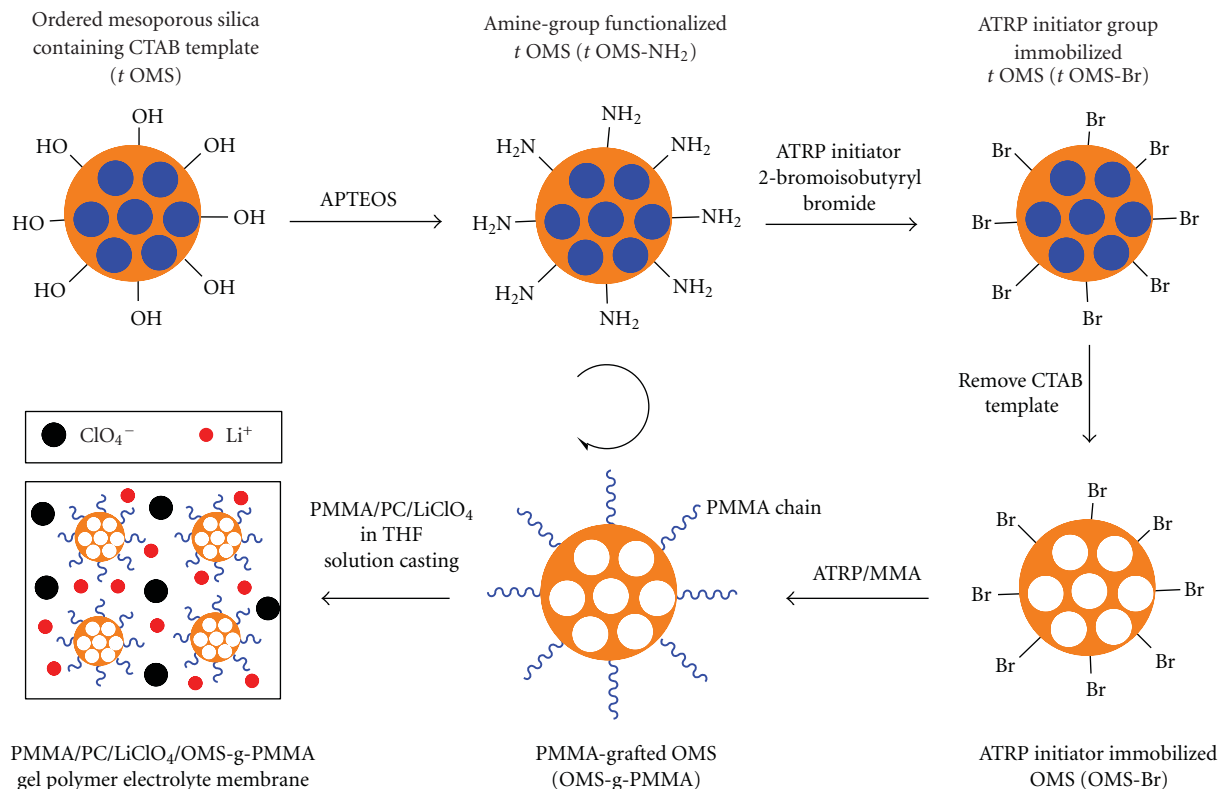


FIGURE 1: The schematic illustration for the synthesis of OMS-g-PMMA and preparation of PMMA/PC/LiClO₄/OMS-g-PMMA gel polymer electrolyte membrane.

respectively. The resulting powder was finally dried at 40°C for 24 h in vacuum, giving the OMS-g-PMMA.

2.3. Preparation of the PMMA-Based GPE Filled with the OMS-g-PMMA. The PMMA-based GPE filled with the OMS-g-PMMA was prepared by a solution casting technique. In a typical procedure, the synthesized OMS-g-PMMA (5~20 mg) was first dispersed in 20 mL THF containing 30 mg PC and 50 mg LiClO₄ by sonication for 1 h, and then, the solvent was removed in vacuo to give a powder-like mixture, OMS-g-PMMA/PC/LiClO₄ (marked as I). The matrix, PMMA, was further dissolved in THF to form a 30 wt % solution (marked as II). A series of PMMA-based GPE filled with the OMS-g-PMMA of different loading concentrations, PMMA/PC/LiClO₄/OMS-g-PMMA (100/30/50/*x*, *w/w/w/w*, *x* changes from 0 to 20), were finally obtained by mixing I and II under sonication and subsequent drying at room temperature for 48 h in a PTFE mould. The *x*, herein, represents the actual weight of OMS in the OMS-g-PMMA, which can be calculated based on thermogravimetric analysis (TGA). For comparison, a series of PMMA-based GPE filled with the bare OMS, PMMA/PC/LiClO₄/bare OMS (100/30/50/*x*, *w/w/w/w*, *x* changes from 0 to 20), were also prepared through the similar procedure mentioned as above. For all the prepared GPE membranes, the average thickness is controlled at ~0.20 cm.

2.4. Characterization. Fourier transform infrared spectroscopy (FTIR) spectra were recorded on a Nicolet 6700 FTIR spectrometer. All samples were prepared as pellets using spectroscopic grade KBr in a presser. TGA was performed on a SDT Q600 thermogravimetry analyzer. Measurements were carried out under N₂ protection from 25°C to 800°C at a heating rate of 20°C/min. High-resolution transmittance electron microscopy (HRTEM) analysis was performed on a 300 kV JEM-100 CX II transmittance electron microscope. TEM samples were prepared by dispersing little sample in ethanol and subsequent depositing onto copper grids. Small-angle X-ray diffraction (SAXRD) analysis was carried out using an XD-98 diffractometer with Cu irradiation (36 kV, 30 mA) at ambient temperature. The scanning rate is 2.0°/min for all samples with a step size of 0.02°. Differential scanning calorimetry (DSC) curves were obtained on a DSC Q100 instrument equipped with a refrigerated cooling system (RCS) under N₂ atmosphere. Samples were heated from 40°C to 200°C at 50°C/min and then cooled to 40°C at 20°C/min to eliminate heating history. Then, the data was recorded on the second heating from 40°C to 200°C at 20°C/min. For all samples, the glass transfer temperature (*T_g*) was read as the middle of the change in heat capacity. The mechanical properties of PMMA-based GPE were tested on a CMT 5104 universal materials mechanics tester at ambient temperature. The crosshead speed was controlled at 15 mm/min. The test samples were designed as rectangular

pieces with a dimension of 2.5 cm (length) \times 1.1 cm (width) \times 0.1~0.3 cm (thickness). The ionic conductivity of PMMA-based GPE was determined by alternating current (AC) impedance analysis on a CHI 650B electrochemical workstation. The measurements were carried out using an electrochemical cell consisting of polymer electrolyte membrane sandwiched between two stainless steel electrodes in a frequency range of 10 Hz to 0.1 MHz over a temperature range of 298~353 K at a relative constant humidity. The ionic conductivity was calculated by

$$\sigma = \frac{1}{R_b} \times \frac{d}{S}, \quad (1)$$

where d is the thickness of electrolyte membrane; S is the contact area between electrode and electrolyte membrane; R_b is the bulk impedance of electrolyte membrane. In this research, the R_b was fitted through a Zplot software according to the equivalent circuit of impedance data.

3. Results and Discussion

3.1. Structure Characterization of the OMS-g-PMMA. As schematically illustrated in Figure 1, the core-shell PMMA-grafted OMS hybrid particle was synthesized by surface-initiated ATRP based on a literature method [22]. The OMS remaining template (t OMS) was first synthesized by sol-gel method and then modified with a coupling agent, APTEOS, to give the amine group-functionalized t OMS (t OMS-NH₂). The ATRP initiator, 2-bromoisobutyryl bromide, was further chemically immobilized onto the exterior surface of OMS by reacting with the amine group from the t OMS-NH₂ and the ATRP initiator-immobilized OMS (OMS-Br) was obtained by removing the template contained in the t OMS-Br through an extraction procedure. The core-shell PMMA-grafted OMS was thus expected to be obtained by using the resulting OMS-Br as substrate for subsequent surface-initiated ATRP of MMA. The structure of the synthesized OMS-g-PMMA was characterized by FTIR, TGA, HRTEM, and SAXRD analysis, respectively.

Figures 2(a)–2(c) illustrates and compares the FTIR spectra of the bare OMS, OMS-Br, and OMS-g-PMMA sample. The peaks at 1087 cm⁻¹, 1637 cm⁻¹ and 3400 cm⁻¹ can be clearly observed for all the spectra. Among them, the peak at 1087 cm⁻¹ originates from the Si-O stretching vibration in the bulk silica and the peaks at 1637 cm⁻¹ and 3400 cm⁻¹ are usually attributed to the adsorbed water on the surface of silica particles. In the spectrum (Figure 2(b)) of the ATRP initiator-functionalized OMS, OMS-Br, two weak peaks at 2854 cm⁻¹ and 2928 cm⁻¹, characteristic of alky C-H stretching vibration modes, are found, while they are absent in that (Figure 2(a)) of the bare OMS, indicating that the ATRP initiator, 2-bromoisobutyryl bromide, has been covalently immobilized onto the OMS particles. The stronger peak at 1735 cm⁻¹ in the spectrum (Figure 2(c)) of the purified OMS-g-PMMA should be assigned to the C=O stretching vibration associated with the ester group from the grafted PMMA. In addition, two peaks at 2946 cm⁻¹ and 2850 cm⁻¹, characteristic of alky C-H stretching vibration, are also found

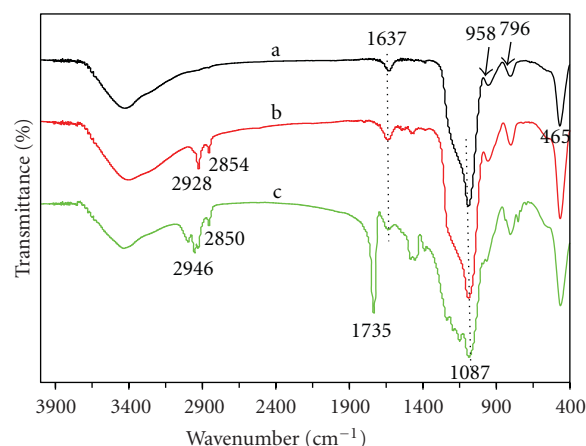


FIGURE 2: Fourier transform infrared (FTIR) spectra of the bare OMS (a), OMS-Br, (b) and OMS-g-PMMA (c).

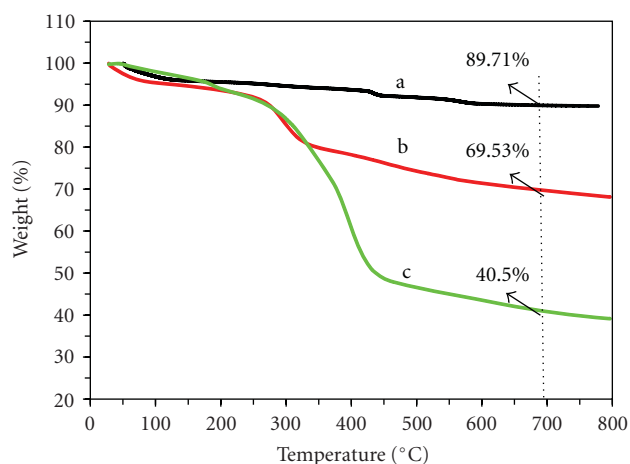


FIGURE 3: Thermogravimetry analysis (TGA) curves of the bare OMS (a), OMS-Br, (b) and OMS-g-PMMA (c).

in above spectrum, corresponding to the added alky groups from the grafted PMMA. These indicate that PMMA chains have been chemically bonded to the surface of OMS particles.

The TGA curves for the above three samples are shown in Figures 3(a)–3(c). A mass loss at 700°C about 10.29% is found for the bare OMS, which might be due to the loss of associated water and remaining CTAB template. Compared to the bare OMS, the mass loss at 700°C for the OMS-Br increases from 10.29% to 30.47%, due to the introduction of chemically bonded coupling agent and ATRP initiator groups. The mass loss at 700°C further increases to 59.50% for the OMS-g-PMMA, indicating that PMMA chains have been covalently grafted to the surface of OMS particles. Taking the mass loss at 700°C as reference, the grafting ratio of PMMA in the OMS-g-PMMA could be calculated to be 0.99 g PMMA/g OMS by assuming that all the organic moieties were lost at 700°C.

The morphology of the bare OMS and OMS-g-PMMA particles was characterized by using HRTEM technique.

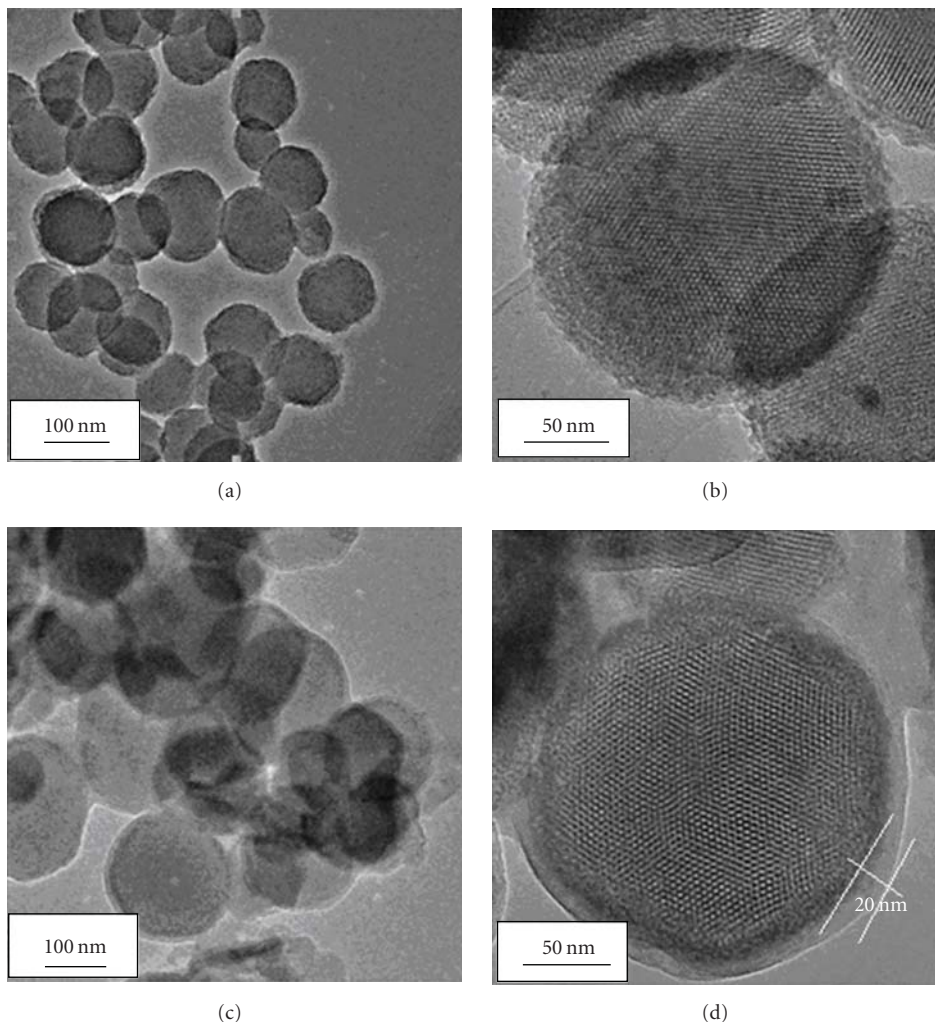


FIGURE 4: High-resolution transmittance electron microscopy (HRTEM) images of the bare OMS ((a), (b)) and OMS-g-PMMA ((c), (d)).

Figures 4(a) and 4(b) shows the HRTEM images of the bare OMS. It can be observed that the bare OMS particles exhibit a roughly spherical shape with an average diameter about 100 nm (Figure 4(a)). In addition, the hexagonally packed dots and parallel stripes are obvious for the bare OMS as shown in Figure 4(b), indicating a typical MCM-41 type mesoporous channel structure. The average pore size of the bare OMS is about 3~4 nm (Figure 4(b)), which is comparable to that (3.5 nm) determined by N_2 adsorption testing. Figures 4(c) and 4(d) shows the HRTEM images for the OMS-g-PMMA. A smooth PMMA shell around the exterior surface of OMS particle, as a core, could be clearly found with an average shell thickness about 20 nm (Figure 4(d)). Moreover, it is also clear that the ordered mesoporous structure of the OMS core is still intact after surface modification by surface-initiated ATRP of MMA.

Figures 5(a) and 5(b) shows the small-angle X-ray diffraction patterns of the bare OMS and OMS-g-PMMA. The XRD pattern for the bare OMS (Figure 5(a)) exhibits an intense peak at $2\theta = 2.148^\circ$, which is usually associated with the (100) diffraction when a hexagonal cell is assumed [23].

In addition, two weak peaks, in the region of $2\theta = 3.5\sim 4.5^\circ$, is also found in the above pattern, which can be indexed as the (110) and (200) diffractions. These confirm that the synthesized OMS has a typical MCM-41 type ordered mesoporous channel structure. As shown in Figure 5(b), the XRD pattern for the OMS-g-PMMA is similar to that of the bare OMS, indicating a remaining intact hexagonal array of the pores in the OMS core after the surface-initiated ATRP of MMA.

3.2. Ionic Conductivity Properties. To examine the effect of the resulting core-shell OMS-g-PMMA on improving the ionic conductivity of PMMA-based GPE, two types of GPE including PMMA/PC/LiClO₄/OMS-g-PMMA and PMMA/PC/LiClO₄/bare OMS were prepared, respectively, with different filler-loading contents by a solution casting technique. The ionic conductivity of the resulting GPE was subsequently determined and compared by AC impedance analysis method. Figure 6 shows the impedance plots for the GPE, PMMA/PC/LiClO₄/OMS-g-PMMA (100/30/50/15,

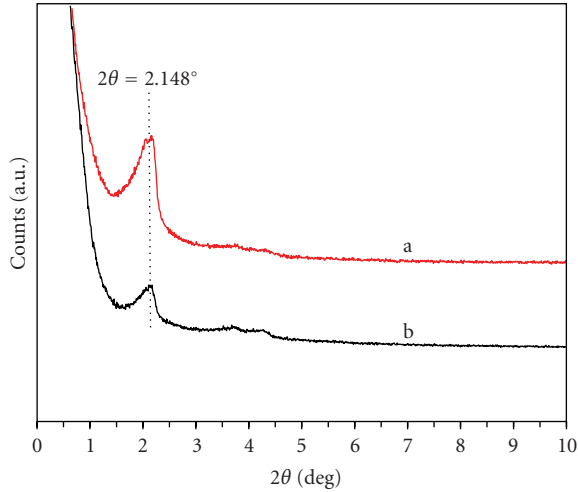


FIGURE 5: Small-angle X-ray diffraction (SAXRD) patterns of the bare OMS (a) and OMS-g-PMMA (b).

$w/w/w/w$), at different temperature. It is shown that at a lower testing temperature, such as 25°C and 30°C, the profile consists of a completely depressed semicircle in high-frequency range and a straight line inclined at a constant angle to the real axis in lower frequency range. The depressed semicircle is related to the conduction process, which corresponds to the bulk resistance, while the linear region is due to the effect of the blocking electrodes, corresponding to the interfacial impedance [6]. In addition, it is also found that the depressed semicircle disappeared gradually, in the higher temperature range (40~80°C), and only a linear region was shown in the lower frequency range, which might be due to the softening of GPE membrane at a higher temperature.

The ionic conductivity of various GPE membranes was further calculated by referring to (1), where the bulk resistance, R_b (Ω), could be determined as the abscissa of crossover of the high- and low-frequency curves in the impedance plot [1]. Figures 7(a) and 7(b) illustrates the temperature variation of the conductivity for two different types of PMMA-based GPE systems, PMMA/PC/LiClO₄/bare OMS (100/30/50/ x , $w/w/w/w$) and PMMA/PC/LiClO₄/OMS-g-PMMA (100/30/50/ x , $w/w/w/w$), under different filler-loading contents. It can be seen that the conductivity for both systems shows the same dependence on the absolute temperature, increasing with the absolute temperature in a non-linear relationship. This non-Arrhenius behavior indicates that the ion transport in above GPE systems is dependent on polymer segmental motion and thus can best be described by the Vogel-Tamman-Fulcher (VTF) equation (2) as follows:

$$\sigma = AT^{-1/2} \exp\left[-\frac{B}{(T - T_0)}\right], \quad (2)$$

where A and B are constants and T_0 is a reference temperature [2]. This equation is characteristic of amorphous polymeric electrolytes, which follows free-volume mode.

Figure 8 illustrates the variation trend of ionic conductivity as a function of filler-loading content for the PMMA-based GPE filled with the bare OMS and OMS-g-PMMA,

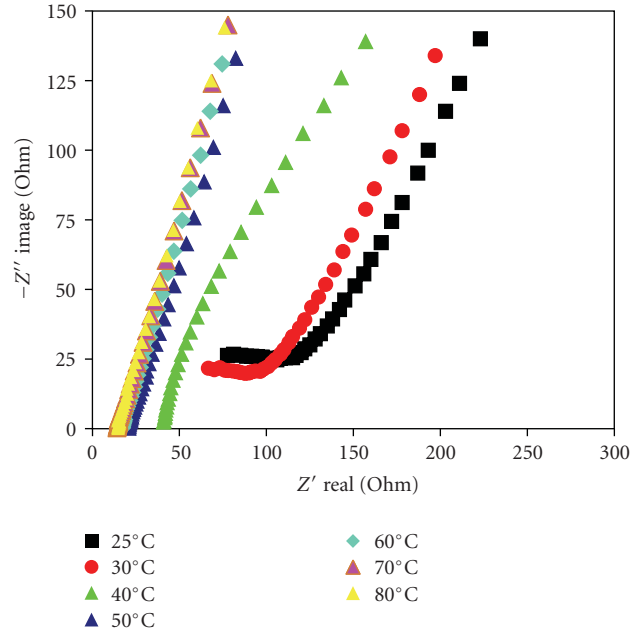


FIGURE 6: AC impedance spectra under different temperature of the PMMA-based GPE, PMMA/PC/LiClO₄/OMS-g-PMMA (100/30/50/15, $w/w/w/w$).

respectively, in a temperature range of 25°C to 80°C. The detailed conductivity data at 25°C are also listed in Table 1 for comparison. As can be seen the conductivity for the filler-filled PMMA-based GPE demonstrates a general increasing trend compared to the parent GPE without doping with filler. The conductivity at 25°C is $1.17 \times 10^{-4} \text{ S}\cdot\text{cm}^{-1}$ and $1.59 \times 10^{-4} \text{ S}\cdot\text{cm}^{-1}$ for the PMMA/PC/LiClO₄/bare OMS (100/30/50/15, $w/w/w/w$) and PMMA/PC/LiClO₄/OMS-g-PMMA (100/30/50/15, $w/w/w/w$) membrane, respectively, which are remarkably higher than that of their parent GPE ($4.76 \times 10^{-6} \text{ S}\cdot\text{cm}^{-1}$) by nearly two order of magnitude. Such an increase in conductivity is maybe due to an additional ion-conducting pathway besides the cooperation interaction between PMMA segment and Li⁺ cations. The additional ion-conducting pathways may be ascribed to the cooperation interaction between the silicon O atoms of OMS and Li⁺ cations, as well as the characteristic orderly packed channels of OMS, which is maybe helpful for transmitting Li⁺ cations by imbedding PMMA and PC into pores. In addition, it is obvious as shown in Figure 8(a) that the conductivity, for the bare OMS filled system, increases with increasing the OMS filler-loading content and reaches a maximum value when the filler-loading content is 15 phr and then begins to decrease. This trend is especially obvious at a lower temperature such as 25°C, 30°C, and 40°C. This trend is likely due to the poor interfacial compatibilization between the bare OMS and PMMA matrix, which results in marked aggregation under a higher OMS filler-loading content. As a result, the conductivity of system decreases with further increasing filler-loading content due to the agglomeration of OMS into larger particles, by which the Li⁺ transferring will be obstructed.

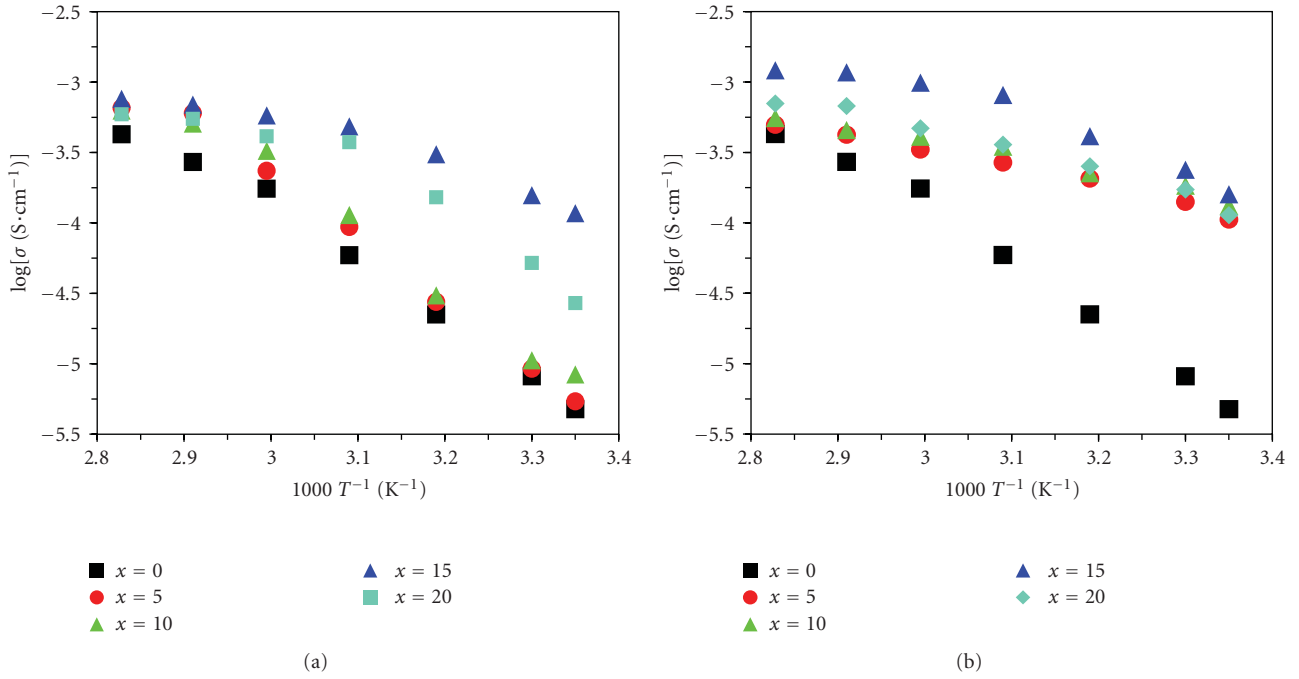


FIGURE 7: Temperature dependence of ionic conductivity of PMMA-based GPE with different filler-loading contents. (a) PMMA/PC/LiClO₄/bare OMS (100/30/50/ x , w/w/w/w); (b) PMMA/PC/LiClO₄/OMS-g-PMMA (100/30/50/ x , w/w/w/w).

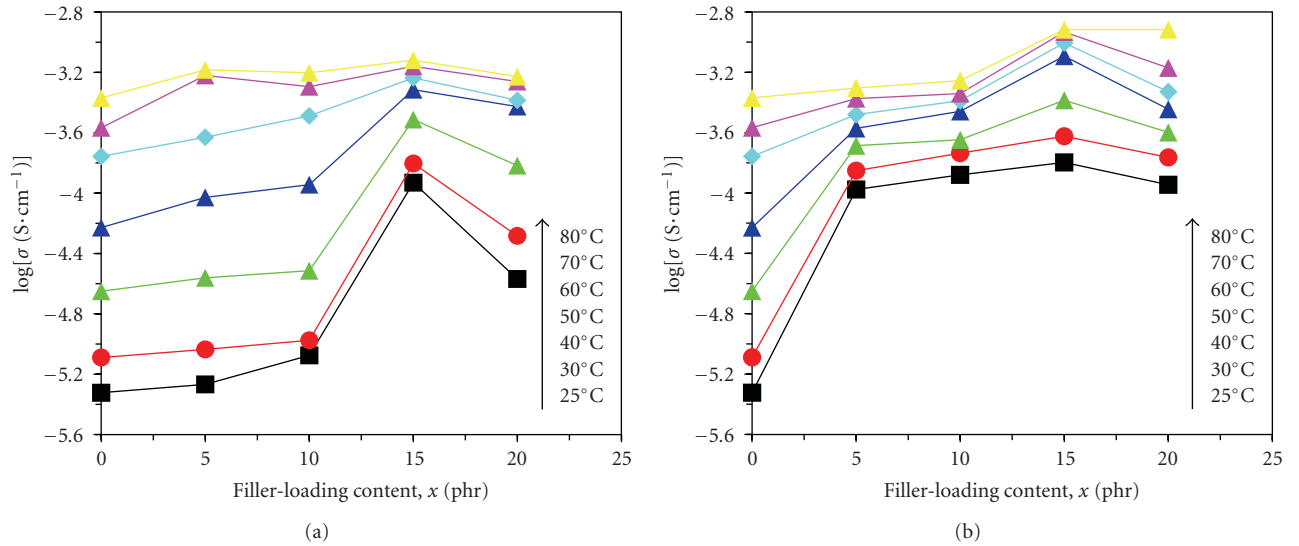


FIGURE 8: Ionic conductivity of PMMA-based GPE as a function of filler-loading content. (a) PMMA/PC/LiClO₄/OMS (100/30/50/ x , w/w/w/w); (b) PMMA/PC/LiClO₄/OMS-g-PMMA (100/30/50/ x , w/w/w/w). For (b), the x is the actual mass of OMS contained in the OMS-g-PMMA.

TABLE 1: Ionic conductivity of PMMA-based GPE with different filler-loading content at 25°C.

Sample	$\sigma \text{ (}\times 10^{-6} \text{ S}\cdot\text{cm}^{-1}\text{)}$				
	$x=0$	$x=5$	$x=10$	$x=15$	$x=20$
PMMA/PC/LiClO ₄ /bare OMS (100/30/50/ x , w/w/w/w)	4.76	5.41	8.41	117.26	26.99
PMMA/PC/LiClO ₄ /OMS-g-PMMA (100/30/50/ x , w/w/w/w)	4.76	105.61	132.01	159.41	113.40

TABLE 2: Ionic conductivity of PMMA-based GPE under different temperature at a filler-loading content of 15 phr.

Sample	σ ($\times 10^{-4}$ S·cm $^{-1}$)						
	25°C	30°C	40°C	50°C	60°C	70°C	80°C
PMMA/PC/LiClO $_4$ /OMS (100/30/50/15, w/w/w/w)	1.17	1.57	3.07	4.85	5.80	6.92	7.60
PMMA/PC/LiClO $_4$ /OMS-g-PMMA (100/30/50/15, w/w/w/w)	1.59	2.38	4.12	8.08	9.88	11.70	12.10

TABLE 3: Mechanical properties of PMMA-based GPE membranes.

Sample	Tensile strength (MPa)	Modulus (MPa)	Elongation (%)
PMMA/PC/LiClO $_4$ (100/30/50, w/w/w)	0.59	0.22	75.19
PMMA/PC/LiClO $_4$ /bare OMS (100/30/50/15, w/w/w/w)	0.96	0.49	60.65
PMMA/PC/LiClO $_4$ / OMS-g-PMMA (100/30/50/15, w/w/w/w)	2.01	0.75	86.52

As shown in Figure 8(b), the conductivity of the OMS-g-PMMA filled system increases with filler-loading content and a highest conductivity was gained at 15 phr OMS-g-PMMA loading content followed by decrease in conductivity with further increase in filler-loading content, which is totally similar to the bare OMS filled system. However, it is noteworthy that at 25°C the conductivity for the OMS-g-PMMA filled system is always higher than that of the bare OMS filled system corresponding to the whole filler-loading content range as shown in Table 1. Moreover, the conductivity for the OMS-g-PMMA filled system gained a higher value (1.06×10^{-4} S·cm $^{-1}$) only when 5 phr OMS-g-PMMA was added, which is comparable to that (1.17×10^{-4} S·cm $^{-1}$) for the bare OMS-filled system corresponding to 15 phr filler-loading content. This indicates that it is easier, for the OMS-g-PMMA filled system, to form an ions transferring network at a lower filler-loading content compared to the bare OMS filled system, which might be due to the highly improved interfacial compatibilization between the OMS and PMMA matrix resulting from surface-modification of OMS through surface-initiated ATRP of MMA. Similarly, it is also found from Table 2 that the conductivity for the OMS-g-PMMA filled system is always higher than that for the bare OMS filled system at the same filler-loading content (15 phr) corresponding to the whole temperature range from 25°C to 80°C.

3.3. Thermal Properties. The thermal properties of the PMMA-based GPE filled with the bare OMS and OMS-g-PMMA, respectively, were characterized by DSC. The effect of fillers on improving the thermal properties of both systems was evaluated. Figures 9(a) and 9(b) illustrates and compares the DSC curves for both systems under different filler-loading content. For the purpose of comparison, the DSC curve for the pure PMMA as GPE matrix is also represented in above figure. As shown in Figure 9(a), the pure PMMA exhibits a higher glass-transition temperature (T_g , 106.3°C) due to the higher stiffness of chains. With the addition of LiClO $_4$ and plasticizer, PC, the T_g for the filler-free sample ($x = 0$) is decreased to 103.4°C with a slight drop about 3°C compared to the pure PMMA. However, a gradual improvement in T_g is observed when the bare OMS of different loading contents was added, showing the effect of

OMS filler. The T_g for the sample ($x = 10$) containing 10 phr bare OMS increases to 110.1°C, which is higher than that of the filler-free sample (103.4°C) and even the pure PMMA (106.3°C). Such an improvement in T_g might be attributed to the characteristic nanoporous structure of OMS particles, which is expected to reduce the mobility of PMMA chains by imbedding the PMMA chains into pore channel under sonication condition. Similarly, a greater improvement in T_g was detected, for the OMS-g-PMMA filled GPE system, with the introduction of the OMS-g-PMMA core-shell particles as shown in Figure 9(b). A maximum (118.9°C) in T_g was gained corresponding to 15 phr filler-loading content ($x = 15$), which is considerably higher, by 15.5°C and 12.6°C, than that of the free-filler sample and pure PMMA, respectively. The explanation for this is maybe due to the characteristic core-shell hybrid structure of the OMS-g-PMMA, in which the PMMA shell grafted onto the exterior surface of OMS core may entangle with the PMMA matrix and thus can highly improve the interfacial compatibilization between the OMS particles with PMMA matrix. As a result, the T_g of system will be considerably improved due to the reduction in mobility of PMMA chains resulting from the entangled structure mentioned as above.

3.4. Mechanical Properties. One of the major drawbacks associated with GPE is the poor mechanical properties due to the addition of excess plasticizer into polymer matrix. Incorporating various types of inorganic nanofillers into polymer matrix to prepare the composite GPE (NGPE) is one of the effective approaches for improving the mechanical properties of GPE. The effect of the OMS-g-PMMA on the mechanical properties of the PMMA-based GPE is examined by tensile testing. The stress-strain curves for the PMMA-based GPE filled with 15 phr of OMS-g-PMMA is shown in Figure 10 and the tensile properties are given in Table 3. The mechanical properties of the GPE filled with 15 phr of bare OMS and the filler-free GPE sample are also given in Figure 10 and Table 3 for comparison. As can be seen the introduction of the bare OMS (15 phr) improves, to an extent, the tensile strength and Young's modulus of the PMMA-based GPE while decreasing slightly the elongation at break. Compared to the filler-free GPE sample, the tensile strength increases by

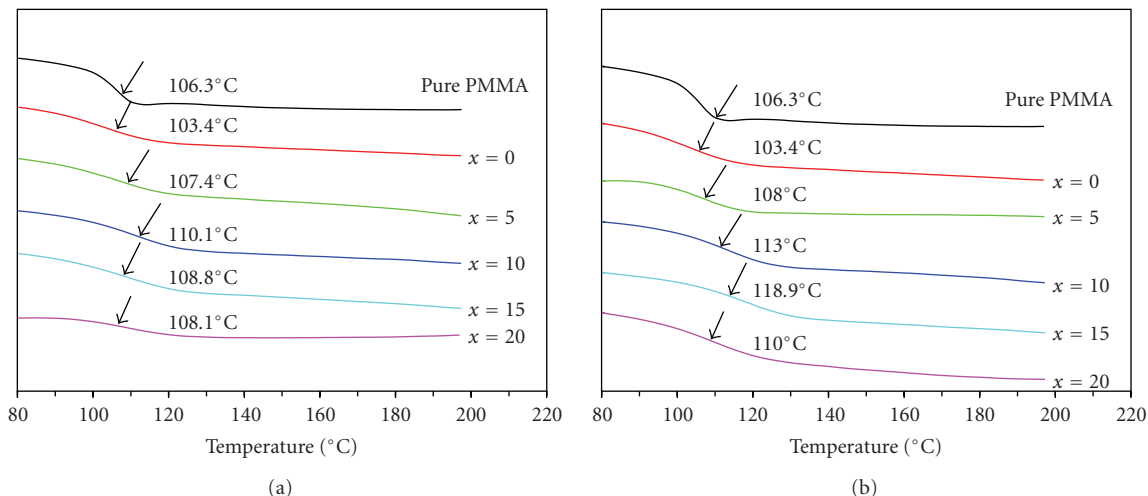


FIGURE 9: Differential scanning calorimetry (DSC) curves of (a) PMMA/PC/LiClO₄/bare OMS (100/30/50/*x*, w/w/w/w) and (b) PMMA/PC/LiClO₄/OMS-g-PMMA (100/30/50/*x*, w/w/w/w). Here, *x* changed from 0 to 20. For (b), the *x* is the actual mass of OMS contained in the OMS-g-PMMA.

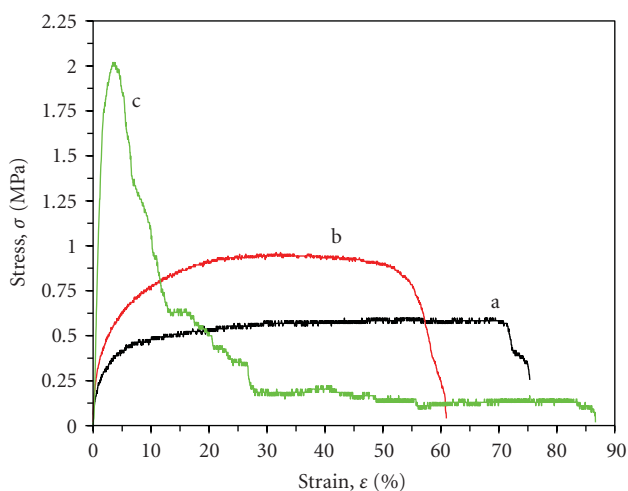


FIGURE 10: Stress-strain curves of PMMA-based GPE. (a) PMMA/PC/LiClO₄ (100/30/50, w/w/w); (b) PMMA/PC/LiClO₄/bare OMS (100/30/50/15, w/w/w/w); (c) PMMA/PC/LiClO₄/OMS-g-PMMA (100/30/50/15, w/w/w/w).

62.7% and the modulus by 123.0%. In the case of the OMS-g-PMMA-filled GPE sample, a more significant enhancement in mechanical properties was observed compared to the bare OMS filled GPE sample. The tensile strength and modulus reach 2.01 MPa and 0.75 MPa, respectively, which is higher by 2.39 times and 2.41 times, respectively, compared to that of the filler-free sample. This indicates that the mechanical properties of the PMMA-based GPE could be effectively improved by adding the core-shell PMMA-grafted OMS into PMMA matrix, which is consistent with the results on DSC analysis that introducing OMS-g-PMMA into PMMA matrix considerably increases the T_g of GPE. The characteristic core-shell structure of the OMS-g-PMMA particles should be responsible for above improvement both in T_g and in mechanical properties of PMMA-based GPE.

4. Conclusion

The core-shell PMMA-grafted OMS hybrid particle has been successfully synthesized by surface-initiated ATRP of MMA. FTIR, TGA, SAXRD, and HRTEM analysis confirm that the resulting OMS-g-PMMA possesses typical core-shell structure, in which a homogeneous PMMA shell is chemically bonded to the exterior surface of the OMS as a core retaining intact MCM-41 type mesoporous structure. The characteristic core-shell OMS-g-PMMA is found, as a filler, to more effectively improve the ionic conductivity of the PMMA-based GPE compared to the bare OMS. AC impedance measurements show that the temperature dependence of ionic conductivity for the PMMA-based GPE filled with OMS-g-PMMA exhibits VTF behavior, and a maximum in conductivity ($1.59 \times 10^{-4} \text{ S} \cdot \text{cm}^{-1}$, 25°C) could be gained at 15 phr filler-loading content, which is higher by nearly two orders than that of the filler-free PMMA-based GPE. Moreover, the results on DSC and tensile testing indicate that the mechanical properties of the PMMA-based GPE could be greatly improved by adding the OMS-g-PMMA to matrix, with a considerable enhancement in T_g ($\sim 15.5^\circ\text{C}$). The tensile strength increased by 2.39 times and Young's modulus by 2.41 times, compared to the filler-free PMMA-based GPE, at 15 phr filler-loading content. The excellent comprehensive properties make the PMMA-based GPE filled with OMS-g-PMMA prospective for lithium batteries and other electrochemical devices.

Acknowledgments

The authors would like to acknowledge the financial support from the National Nature Science Fund of China (21074117) and appreciate the support of the Key Research Project (no. 2008C01021-2) from Science and Technology Department of Zhejiang Province.

References

- [1] Y. Wang, X. Ma, Q. Zhang, and N. Tian, "Synthesis and properties of gel polymer electrolyte membranes based on novel comb-like methyl methacrylate copolymers," *Journal of Membrane Science*, vol. 349, no. 1-2, pp. 279–286, 2010.
- [2] S. Rajendran, V. S. Bama, and M. R. Prabhu, "Effect of lithium salt concentration in PVAc/PMMA-based gel polymer electrolytes," *Ionics*, vol. 16, no. 1, pp. 27–32, 2010.
- [3] Y. Liao, M. Rao, W. Li, C. Tan, J. Yi, and L. Chen, "Improvement in ionic conductivity of self-supported P(MMA-AN-VAc) gel electrolyte by fumed silica for lithium ion batteries," *Electrochimica Acta*, vol. 54, no. 26, pp. 6396–6402, 2009.
- [4] Q. Xiao, Z. Li, D. Gao, T. He, and H. Zhang, "Preparation and electrochemical performance of gel polymer electrolytes with a novel star network," *Journal of Applied Electrochemistry*, vol. 39, no. 2, pp. 247–251, 2009.
- [5] L. Othman, K. W. Chew, and Z. Osman, "Impedance spectroscopy studies of poly (methyl methacrylate)-lithium salts polymer electrolyte systems," *Ionics*, vol. 13, no. 5, pp. 337–342, 2007.
- [6] D. Shanmukaraj, G. X. Wang, R. Murugan, and H. K. Liu, "Ionic conductivity and electrochemical stability of poly(methylmethacrylate)-poly(ethylene oxide) blend-ceramic fillers composites," *Journal of Physics and Chemistry of Solids*, vol. 69, no. 1, pp. 243–248, 2008.
- [7] J. P. Sharma and S. S. Sekhon, "Nanodispersed polymer gel electrolytes: conductivity modification with the addition of PMMA and fumed silica," *Solid State Ionics*, vol. 178, no. 5-6, pp. 439–445, 2007.
- [8] S. Ahmad, S. Ahmad, and S. A. Agnihotry, "Nanocomposite electrolytes with fumed silica in poly(methyl methacrylate): thermal, rheological and conductivity studies," *Journal of Power Sources*, vol. 140, no. 1, pp. 151–156, 2005.
- [9] Y. X. Jiang, Z. F. Chen, Q. C. Zhuang et al., "A novel composite microporous polymer electrolyte prepared with molecule sieves for Li-ion batteries," *Journal of Power Sources*, vol. 160, no. 2, pp. 1320–1328, 2006.
- [10] J. Xi, X. Qiu, M. Cui, X. Tang, W. Zhu, and L. Chen, "Enhanced electrochemical properties of PEO-based composite polymer electrolyte with shape-selective molecular sieves," *Journal of Power Sources*, vol. 156, no. 2, pp. 581–588, 2006.
- [11] F. Chen, X. Ma, X. Qu, and H. Yan, "Structure and properties of an organic rectorite/poly(methyl methacrylate) nanocomposite gel polymer electrolyte by in situ synthesis," *Journal of Applied Polymer Science*, vol. 114, no. 5, pp. 2632–2638, 2009.
- [12] O. Krejza, J. Velická, M. Sedlářiková, and J. Vondrák, "The presence of nanostructured Al₂O₃ in PMMA-based gel electrolytes," *Journal of Power Sources*, vol. 178, no. 2, pp. 774–778, 2008.
- [13] S. Ahmad, T. K. Saxena, S. Ahmad, and S. A. Agnihotry, "The effect of nanosized TiO₂ addition on poly(methylmethacrylate) based polymer electrolytes," *Journal of Power Sources*, vol. 159, no. 1, pp. 205–209, 2006.
- [14] S. H. Chung, L. Persi, F. Croce, S. G. Greenbaum, B. Scrosati, and E. Plichta, "Enhancement of ion transport in polymer electrolytes by addition of nanoscale inorganic oxides," *Journal of Power Sources*, vol. 97-98, pp. 644–648, 2001.
- [15] F. Croce, L. L. Persi, B. Scrosati, F. Serraino-Fiory, E. Plichta, and M. A. Hendrickson, "Role of the ceramic fillers in enhancing the transport properties of composite polymer electrolytes," *Electrochimica Acta*, vol. 46, no. 16, pp. 2457–2461, 2001.
- [16] M. J. Reddy and P. P. Chu, "⁷Li NMR spectroscopy and ion conduction mechanism in mesoporous silica (SBA-15) composite poly(ethylene oxide) electrolyte," *Journal of Power Sources*, vol. 135, no. 1-2, pp. 1–8, 2004.
- [17] S. Kim, E. J. Hwang, and S. J. Park, "An experimental study on the effect of mesoporous silica addition on ion conductivity of poly(ethylene oxide) electrolytes," *Current Applied Physics*, vol. 8, no. 6, pp. 729–731, 2008.
- [18] J. Xi, S. Miao, and X. Tang, "Selective transporting of lithium ion by shape selective molecular sieves ZSM-5 in PEO-based composite polymer electrolyte," *Macromolecules*, vol. 37, no. 23, pp. 8592–8598, 2004.
- [19] Ch. V. Subba Reddy, G. P. Wu, C. X. Zhao, Q. Y. Zhu, W. Chen, and R. R. Kalluru, "Characterization of SBA-15 doped (PEO + LiClO) polymer electrolytes for electrochemical applications," *Journal of Non-Crystalline Solids*, vol. 353, no. 4, pp. 440–445, 2007.
- [20] J. Xi, X. Qiu, X. Ma et al., "Composite polymer electrolyte doped with mesoporous silica SBA-15 for lithium polymer battery," *Solid State Ionics*, vol. 176, no. 13-14, pp. 1249–1260, 2005.
- [21] X. L. Wang, A. Mei, M. Li, Y. Lin, and C. W. Nan, "Effect of silane-functionalized mesoporous silica SBA-15 on performance of PEO-based composite polymer electrolytes," *Solid State Ionics*, vol. 177, no. 15-16, pp. 1287–1291, 2006.
- [22] Y. Yang, X. Yan, Y. Cui et al., "Preparation of polymer-coated mesoporous silica nanoparticles used for cellular imaging by a "graft-from" method," *Journal of Materials Chemistry*, vol. 18, no. 47, pp. 5731–5737, 2008.
- [23] C. F. Cheng, H. H. Cheng, P. O. W. Cheng, and Y. J. Lee, "Effect of reactive channel functional groups and nanoporosity of nanoscale mesoporous silica on properties of polyimide composite," *Macromolecules*, vol. 39, no. 22, pp. 7583–7590, 2006.

Research Article

Comparative Study of the Photocatalytic Activity of Semiconductor Nanostructures and Their Hybrid Metal Nanocomposites on the Photodegradation of Malathion

Dina Mamdouh Fouad¹ and Mona Bakr Mohamed^{2,3}

¹Chemistry Department, Faculty of Science, Assiut University, Assiut 71516, Egypt

²National Institute of Laser Enhanced Science, Cairo University, Giza, Egypt

³NanoTech Egypt for Photoelectronic, Dreamland, October City, Egypt

Correspondence should be addressed to Dina Mamdouh Fouad, dinafouad93@hotmail.com

Received 3 March 2011; Accepted 31 March 2011

Academic Editor: Linbao Luo

Copyright © 2012 D. M. Fouad and M. B. Mohamed. This is an open access article distributed under the Creative Commons Attribution License, which permits unrestricted use, distribution, and reproduction in any medium, provided the original work is properly cited.

This work is devoted to synthesize different semiconductor nanoparticles and their metal-hybrid nanocomposites such as TiO₂, Au/TiO₂, ZnO, and Au/ZnO. The morphology and crystal structure of the prepared nanomaterials are characterized by the TEM and XRD, respectively. These materials are used as catalysts for the photodegradation of Malathion which is one of the most commonly used pesticides in the developing countries. The degradation of 10 ppm Malathion under ultraviolet (UV) and visible light in the presence of the different synthesized nanocomposites was analyzed with high-performance liquid chromatography (HPLC) and UV-Visible Spectra. A comprehensive study is carried out for the catalytic efficiency of the prepared nanoparticles. Different factors influencing the catalytic photodegradation are investigated, as different light source, surface coverage, and nature of the organic contaminants. The results indicate that hybrid nanocomposite of the semiconductor-metal hybrid serves as a better catalytic system compared with semiconductor nanoparticles themselves.

1. Introduction

Malathion, an organophosphorous pesticide with a broad range of target pests, has been widely used in agriculture. Malathion is suspected to cause child leukemia, anemia, and kidney failure and is widely used in developing countries [1, 2]; it can persist in the human body for at least two generations [3, 4]. However, due to its chemical stability and high toxicity, Malathion resists biodegradation [5]. Therefore, it was important to explore a new methodology for reducing the contamination of water with Malathion. Photocatalysis is considered to be one of the most potential pollution remediation technologies in recent decades [6, 7]. In recent years, semiconductor photocatalysis has become more and more attractive and important since it has a great potential to contribute to such environmental problems. One of the most important aspects of environmental photocatalysis is the selection of the semiconductor material. Semiconductor

photocatalyst generates electron and hole pair (e^- - h^+) upon irradiation of light energy that could be utilized in initiating oxidation and reduction reactions of the pesticide, respectively. Guillard et al. [8] reported that the number of photons striking the photocatalyst actually controls the rate of the reaction which is an indication that the reaction takes place only on the adsorbed phase of the semiconductor particle. Surface morphology, namely, the particle size and shape is a very important parameter influencing the performance of photocatalyst in photocatalytic oxidation [9]. TiO₂ is one of the most commonly studied photocatalysts for it is easily available, relatively inexpensive, and chemically stable [10, 11]. However, TiO₂ is incompetent due to the wide band gap, it can only be triggered by near UV radiation, the photo-generated electron and hole pairs are liable to recombination, leading to low quantum yields [12, 13]. ZnO has received much attention in the degradation of environmental pollutants since it has almost the same band

gap energy (3.2 eV) as TiO_2 . However, photo-corrosion frequently occurs with illumination of UV light and is considered as one of the main reasons for the decrease of ZnO photocatalytic activity.

Nanosized Gold particle possesses many excellent properties, such as easy reductive preparation, water solubility, high chemical stability, and significant biocompatibility and affinity [14]. Surface plasmon resonance absorption is a unique property of gold which is the ability of showing a strong absorption band in the visible region when the frequency of the electromagnetic field is resonant with the coherent electron motion [15]. Combining the semiconductor and metallic character in the same nanomaterial could enhance the catalytic activity due to the increase of the photo-absorption resulting from the plasmonic effect and also increases the rate of charge separation at the interface.

The prospect of developing new multifunctional nanocomposites of metal gold hybridized with inorganic components has become of great importance [16–18]. Bimetallic colloids are interesting from a number of perspectives, such as their unique electronic, catalytic, and optical properties [19–21]; photodegradation of Malathion has been studied in aqueous solution using an Au-Pd- TiO_2 nanotubes film [22].

In the present work, we tested the suitability of using semiconductor nanocomposites (TiO_2 , ZnO) and metal semiconductors nanocomposite (Au/ TiO_2 , Au/ZnO) for the photodegradation of Malathion. The photocatalytic activities of the different synthesized nanoparticles are compared, and the influence of different parameters is studied, such as surface coverage and light source irradiation. The efficiency of the catalytic activity showed dependence on source of light irradiation, particle size, crystalline, surface coverage of the nanocomposite, and nature of the organic contaminate.

2. Materials and Methods

2.1. Chemicals. Malathion (99% HPLC grade) was purchased from Fluka and used as received. Hydrogen tetrachloroaurate trihydrate ($\text{HAuCl}_4 \cdot 3\text{H}_2\text{O}$) (99.9%) was purchased from Sigma-Aldrich, and Polyvinyl pyrrolidone PVP-K30 (Av. Wt. 22000) was purchased from Fluka. Tri-sodium citrate (99%) was purchased from (Sigma-Aldrich), sterile sodium chloride physiological saline (0.9%) (ADWIC). TiO_2 , ZnO and HPLC grade solvents (purity 99%) such as methanol and ethanol were purchased from Aldrich. High purity water used in the experiments was purified with the milli-Q system. All chemicals were used without any further purification.

2.2. Synthesis of Semiconductor Nanoparticles

2.2.1. Synthesis of TiO_2 Nanoparticles. The precursor of 5 mL Titanium isopropoxide is added to a mixture of 5 mL of isopropyl alcohol and 3 mL glacial acetic acid dropwise with constant stirring. The prepared particles are separated with centrifuge and dried for further characterization. The particle size and shape is determined using TEM and the crystal

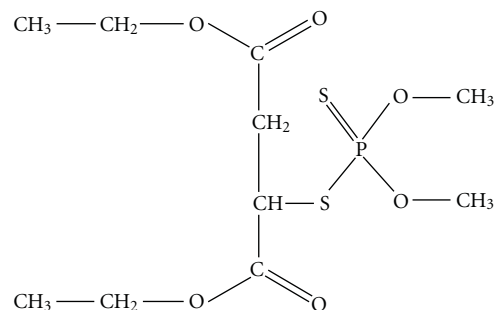


FIGURE 1: Chemical structure of Malathion.

structure is determined using XRD. The optical absorption is measured using UV-Visible PerkinElmer Lambda 40 double beam spectrophotometer.

2.2.2. Synthesis of ZnO Nanoparticles. 1.48 g (10 mmol) of $\text{Zn}(\text{CH}_3\text{COO})_2 \cdot 2\text{H}_2\text{O}$ and 1.38 g (23.8 mmol) of NaHCO_3 are mixed at room temperature. The mixture is ignited at 300°C for 3 hours. The $\text{Zn}(\text{CH}_3\text{COO})_2 \cdot 2\text{H}_2\text{O}$ is converted to ZnO nanoparticles, while the NaHCO_3 is converted to CH_3COONa and eventually washed away with deionized water until the formation of white ZnO nanoparticles. The particle size and shape is determined using TEM, and the crystal structure is determined using XRD.

2.2.3. Synthesis of Gold Nanoparticles by Citrate Method. Spherical gold nanoparticles (GNPs) were prepared in aqueous solution according to a method described by Turkevich. Simply, the method is a chemical reduction of gold ions by sodium citrate in aqueous solution. Sodium citrate serves also as a capping material which prevents aggregation and further growth of the particles. 5 mL of 1% sodium citrate solution was added to 40 mL chloroauric acid (HAuCl_4) boiling solution containing 5 mg of gold ions. The solution was boiled for 30 minutes and was then left to cool down to room temperature. The particle size and shape is determined using TEM, and the crystal structure is determined using XRD.

2.2.4. Synthesis Au/ TiO_2 and Au/ZnO Nanoparticles. Gold nanoparticles are prepared by citrate method as shown above, and the obtained particles are used as a seed to grow TiO_2 or ZnO nanoshell. The reaction mixture is microwaved for 12 minutes. The particle size and shape is determined using TEM, and the crystal structure is determined using XRD.

2.3. Photodegradation of Malathion. Photodegradation radiation rate of Malathion was carried out using Bischof HPLC system (Mainz, Germany), C18, reversed Colum (250×4.6 mm), and UV-detector with variable wave length 250 nm was used. Methanol/water (70/30) was used as an eluent at flow rate of 1 mL/min at retention times 12 min. $20 \mu\text{L}$ was injected to the HPLC at periodic interval 20 minutes. The adsorption of the pesticides on the nanoparticles resulted

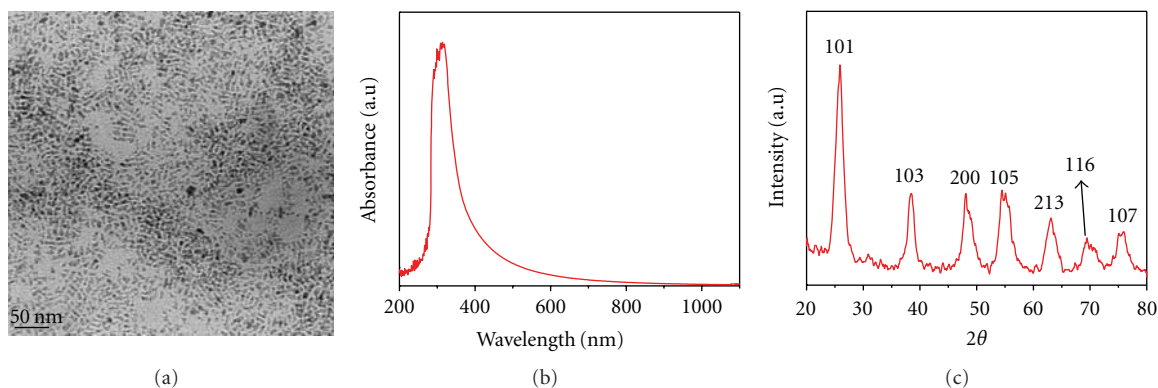


FIGURE 2: Shows TEM image (a), UV-Vis absorption spectrum (b), and XRD patterns (c) of prepared TiO₂ nanoparticles.

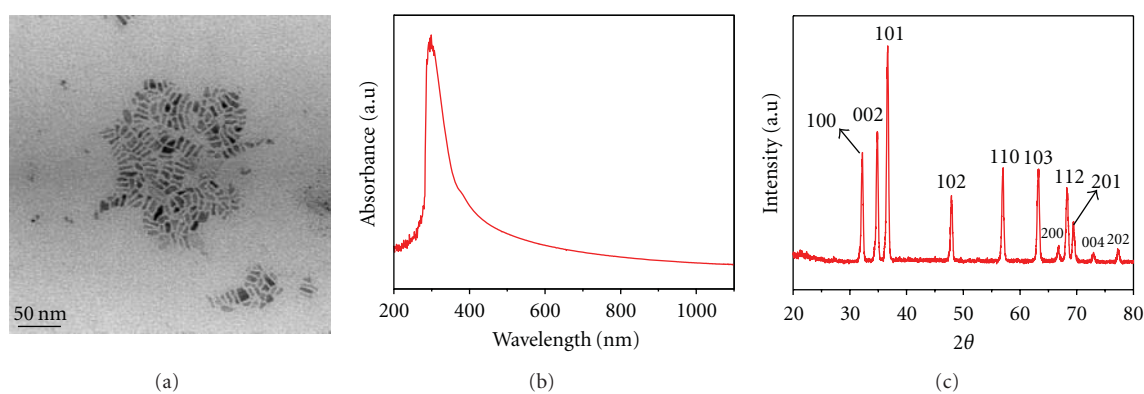


FIGURE 3: Shows TEM image (a), UV-Vis absorption spectrum (b), and XRD patterns (c) of prepared ZnO nanoparticles.

in the gradual decrease in the peak area and area percent in comparison to the peak area and area percent of the standard solution of the Malathion. An interaction was carried out between 10 ppm of Malathion (Figure 1) with the different synthesised nanoparticles (TiO₂, ZnO, Au/ZnO, and Au/TiO₂) of three different concentrations (10^{-4} , 3×10^{-5} , 10^{-5} M); the different aliquots were subjected to UV lamp, natural sunlight and investigated at equal time intervals 30 min and analyzed by using Perkin Elemer 240 spectrophotometer. Data acquisition and manipulation were performed using computer-based program.

3. Results and Discussion

3.1. Characterization of the Synthesized Nanocomposites. Different metal oxide nanoparticles such as TiO₂, ZnO, and their core-shell gold nanocomposites has been synthesized chemically as shown in the experimental part and characterized using absorption spectra, TEM and XRD. Figures 2, 3, 4, and 5 show the absorption spectra associated with TEM images for all the particles prepared. As shown in Figures 2–5, the prepared nanoparticles have monodispersed size and shapes and their size is less than 100 nm and a band gap absorption in the UV region; accordingly irradiation with UV light only creates (e^- - h^+) pair and activates the material

to be a photocatalyst. Presence of gold with the nanocomposite enhances its absorption coefficient and increases the photocatalytic activity due to the increase in the charge separation rate. Also the gold-semiconductor composite has absorption at visible region due to the surface plasmon of the gold particle; this means that the photocatalytic activity of gold could be initiated by irradiation with both UV and visible lights.

3.2. Effect of Different Light Sources. Malathion has a characteristic absorption band at 260 nm; however, the rate of photodegradation is followed using the decay of this band. The degradation of Malathion was carried out under the irradiation of light from two different sources, sun light (which is mainly visible light) and UV lamp which emits light around 254 nm (Table 1). It has been reported that the photodegradation rate increases as increasing the light intensity during photocatalytic degradation reaction [22–25]. Our results clearly indicate that UV irradiation causes higher rate of degradation for Malathion than with sun light, due to high intensity of light which is suitable for the excitation of many electrons from the valence band of the metal oxide semiconductor as illustrated in Figure 6. The band gap for TiO₂ and ZnO lies in the UV region, thus, using UV light initiates the excitation of electrons from the conduction band into the valence band due to the

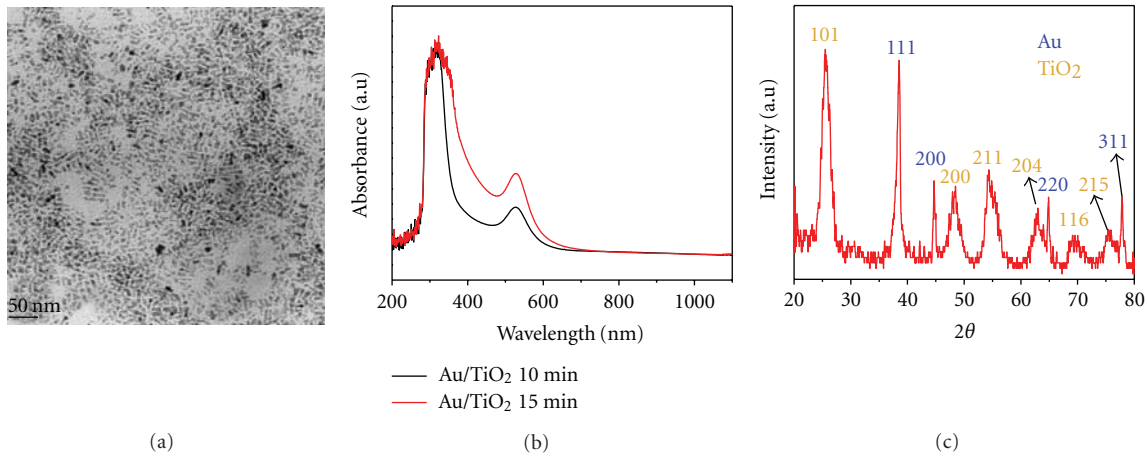


FIGURE 4: Shows TEM image (a), UV-Vis absorption spectrum (b), and XRD patterns (c) of prepared Au/TiO₂ nanoparticles.

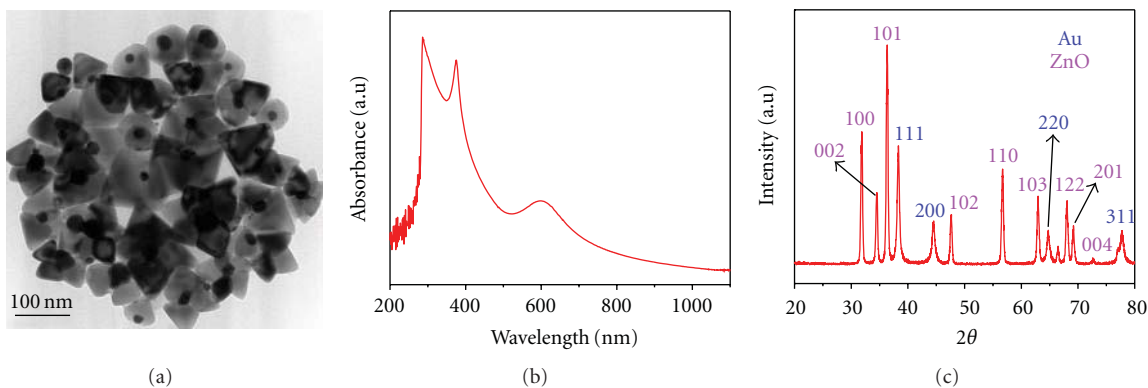


FIGURE 5: Shows TEM image (a), UV-Vis absorption spectrum (b), and XRD patterns (c) of prepared Au/ZnO nanoparticles.

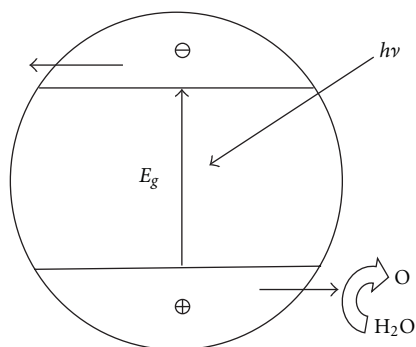


FIGURE 6: Scheme shows the roles of the Semiconductor metal oxide in photodegradation which creates active oxygen causing decomposition of water pollutants.

formed electron or active oxygen which are responsible for the degradation of the Malathion. Presence of the gold in the photocatalyst permits the photodegradation of Malathion in natural sun light since it is a visible light responsive catalyst having an absorption band around 520 nm; this explains the marked increase in photodegradation of Malathion with Au/ZnO and Au/TiO₂. The catalytic activity is markedly

TABLE 1: Degradation of Malathion after 1 hour on irradiation to UV-lamp and natural sun light.

Photocatalysts	Degradation rate %	
	Irradiation to sun light	Irradiation to UV-C lamp
TiO ₂	6	68
ZnO	5	60
Au/ZnO	62	79
Au/TiO ₂	67	81

enhanced by doping small amounts of metals such as Au which prevents the electron hole recombination and accelerates the photocatalytic degradation with UV light to a greater extent as shown in (Table 1). Figure 7 presents the HPLC chromatograms for Malathion alone, and after the addition of the different nanoparticles, Malathion showed a marked decrease in the peak height and the integration area percentage in addition to the Au/TiO₂ and Au/ZnO nanoparticles to Malathion in comparison to the photodegradation using TiO₂ and ZnO as presented in (Table 2), which adopts the idea that the presence of gold effectively scavenged the holes, thus competing with the charge recombination which in terms accelerates the photodegradation.

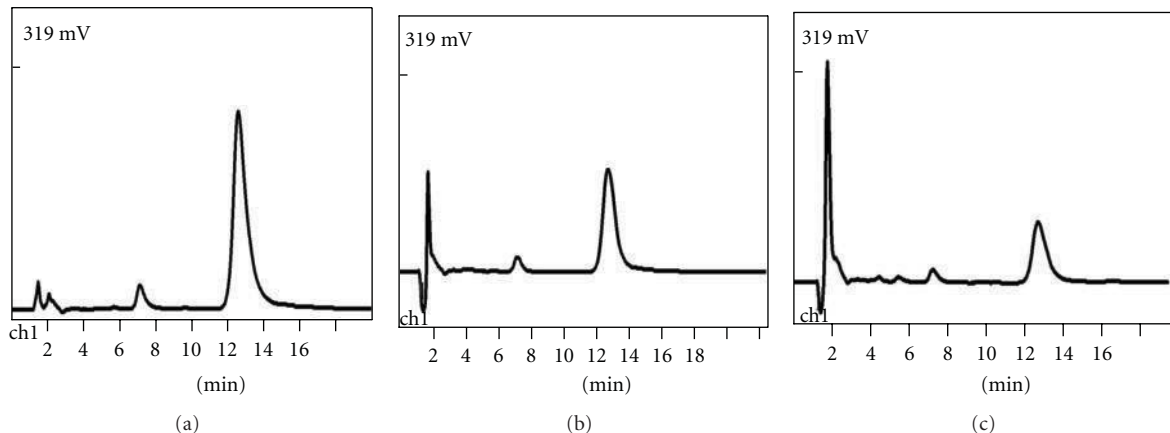


FIGURE 7: Shows HPLC chromatogram for Malathion (a), Malathion + Au/ZnO (b), and Malathion Au/TiO₂ (c).

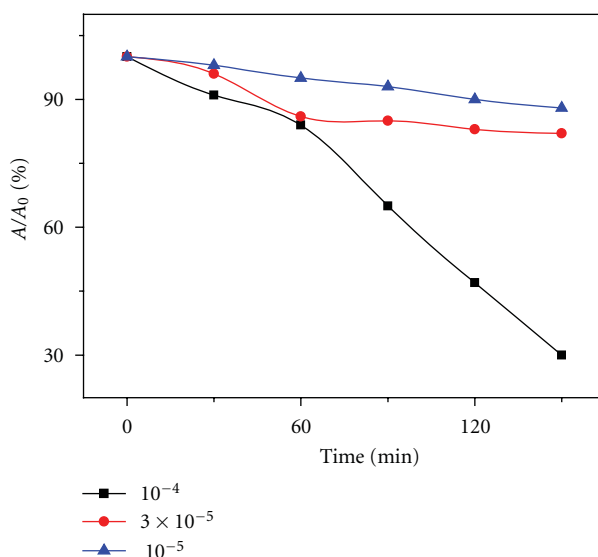


FIGURE 8: Shows the effect of different concentrations of TiO₂ nanoparticle on the degradation of Malathion.

TABLE 2: HPLC integration area for Malathion on irradiation to UV.

Photocatalyst	Integration area (%)	
	At once	After an hour
TiO ₂	83	40
Au/TiO ₂	75	19
Au/ZnO	85	27

3.3. Effect of the Nature of Photocatalyst. A direct correlation exists between the removal of the organic pollutant and the surface coverage of TiO₂ photocatalyst [26]. Heterogeneous photocatalytic reactions are known to show a proportional increase in the photodegradation with catalyst loading [27]. Generally, in any given photocatalytic application, the optimum catalyst concentration must be determined, in order to avoid the excess catalyst and ensure the total absorption of the efficient photons [28]. This is because the scattering of an unfavorable light and reduction of

light penetration into the solution is observed with excess photocatalyst loading [29]. During photocatalytic oxidation process, the concentration of organic substrate over time is dependent upon photonic efficiency [30]. At high-substrate concentrations, however, the photonic efficiency diminishes and the titanium dioxide surface becomes saturated leading to catalyst deactivation [31]. Different concentrations of the nanoparticles were investigated to select the optimal concentration for efficient photodegradation. As presented in Figure 8, it is concluded that 10⁻⁴ M is the optimum concentration for efficient degradation of Malathion using the different nanoparticles; about 69% was achieved in 1 hour using TiO₂; at lower concentrations (3 × 10⁻⁵, 10⁻⁴) free radical production rate is limited which suppresses the rate of the degradation reaction to (10–20%). The same trend was obtained for the prepared nanoparticles as presented in Figures 9–10; an increase of the degradation percentage was observed on using Au/ZnO and Au/TiO₂ and also a reduction of the radiation rate time, which is due to the presence of

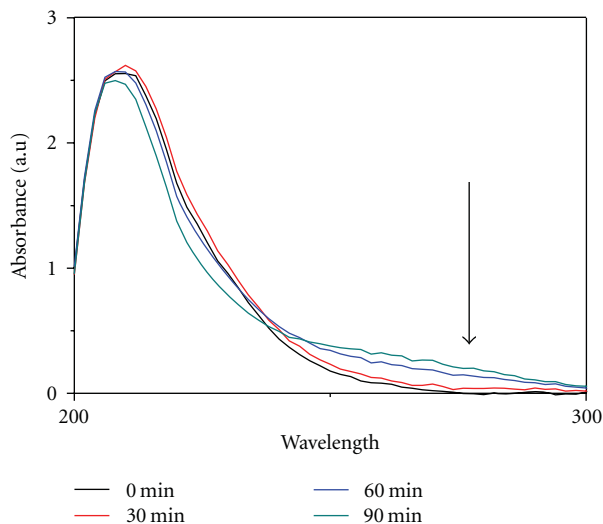


FIGURE 9: Shows time-dependent degradation of Malathion using TiO_2 in UV lamp.

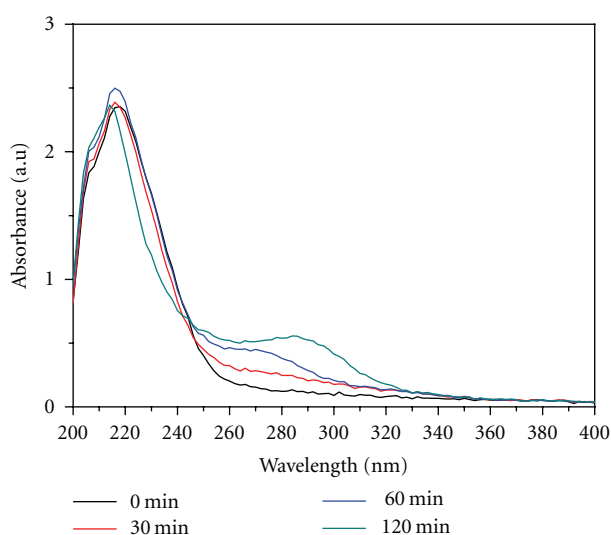


FIGURE 10: Shows time-dependent degradation of Malathion using Au/ZnO in UV lamp.

the gold which prevents the electron hole recombination and accelerates the photodegradation.

3.4. Effect of the Nature of the Contaminant. Organic molecules which adhere effectively to the surface of the photocatalyst are more susceptible to direct oxidation [32]. Thus the photocatalytic degradation of aromatics depends on the substituent group. It is reported that nitro-phenol is much stronger adsorbing substrate than phenol and therefore degrades faster [33]. In the degradation of chloroaromatics, Bhatkhande et al. [34] pointed out that monochlorinated phenol degrades faster than di- or tri-chlorinated member. In general, molecules with electron withdrawing groups such as nitrobenzene and benzoic acid were found to adsorb significantly in the dark compared to those with electron

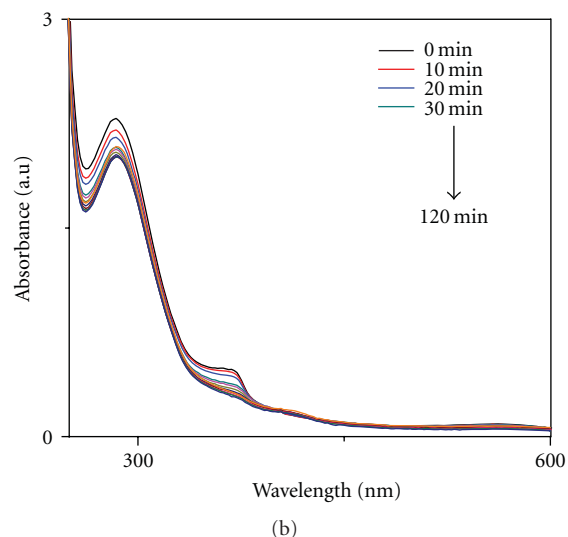
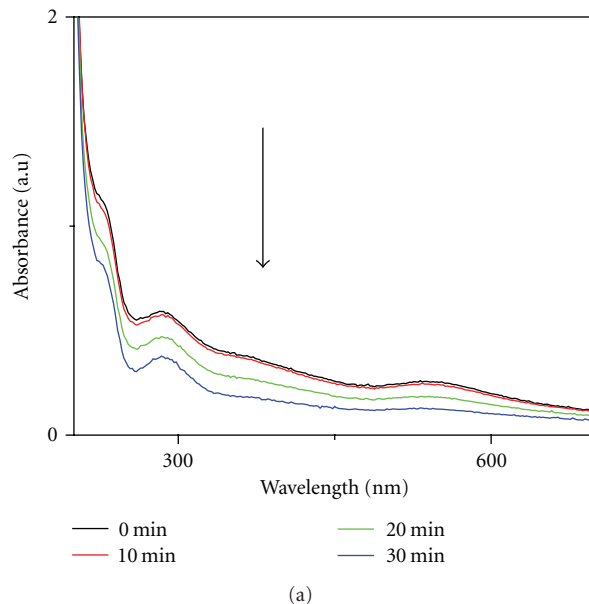


FIGURE 11: Shows time-dependent photodegradation of chloridazone in UV lamp after addition of 10^{-4} TiO_2/Au (a) and ZnO/Au (b).

donating groups [35]. During photocatalytic oxidation process, the concentration of organic substrate over time is dependent upon photonic efficiency [36]. At high-substrate concentrations, however, the photonic efficiency diminishes and the titanium dioxide surface becomes saturated leading to catalyst deactivation [37]. In the present work, we compared the degradation of two different pesticides as a model for aliphatic (Malathion) and chloroaromatic (chloridazone) by subjecting them to the same concentration of different categories of nanoparticle Au/ TiO_2 and Au/ZnO and for same period of time, about 1 hour. As indicated in Figure 11, it is clearly shown that the degradation of chloridazone is faster in comparison to Malathion; a similar trend of degradation was obtained for the both types of nanoparticles since after irradiation to UV lamp for 30 min the degradation

of Malathion was about 30%, while in case of chloridazone it was about 50%; this could be explained in terms of the presence of aromatic rings as well as the number and nature of substituent on the ring (like electron donating or electron withdrawing groups) which are known to affect the adsorption and consequently the degradation rate [38].

4. Conclusion

The ability to synthesize multicomponent nanocomposites is important to improve the electronic, optical, and magnetic functionality. According to our study, gold hybrid semiconductor-noble metal nanocrystals not only combine the unique properties of the metal and semiconductors but also generate collective new phenomena based on the intraparticles interaction between the metal and the semiconductor at their interface. The presence of metal-semiconductor interface promotes effective charge separation carrier transfers which subsequently enhance photocatalytic effect. Photodegradation of 10 ppm Malathion was enhanced in the presence of gold-semiconductor nanoparticle; other factors also influenced the degradation rate such as different light sources and nature of the catalyst.

References

- [1] J. L. Adgate, D. B. Barr, C. A. Clayton et al., "Measurement of children's exposure to pesticides: analysis of urinary metabolite levels in a probability-based sample," *Environmental Health Perspectives*, vol. 109, no. 6, pp. 583–590, 2001.
- [2] D. Zeljezic and V. Garaj-Vrhovac, "Evaluation of genetic damage in workers employed in pesticide production utilizing the comet assay," *Chemosphere*, vol. 46, pp. 295–303, 2002.
- [3] T. Vial, B. Nicolas, and J. Descotes, "Clinical immunotoxicity of pesticides," *Journal of Toxicology and Environmental Health*, vol. 48, no. 3, pp. 215–229, 1996.
- [4] A. S. Nair, C. Subramaniam, M. J. Rosemary et al., "Nanoparticles-chemistry, new synthetic approaches, gas phase clustering and novel applications," *Pramana Journal of Physics*, vol. 65, no. 4, pp. 631–640, 2005.
- [5] B. Kumari, A. Guha, M. G. Pathak, T. C. Bora, and M. K. Roy, "Experimental biofilm and Its application in malathion degradation," *Folia Microbiologica*, vol. 43, no. 1, pp. 27–30, 1998.
- [6] I. Oller, W. Gernjak, M. I. Maldonado, L. A. Pérez-Estrada, J. A. Sánchez-Pérez, and S. Malato, "Solar photocatalytic degradation of some hazardous water-soluble pesticides at pilot-plant scale," *Journal of Hazardous Materials*, vol. 138, no. 3, pp. 507–517, 2006.
- [7] A. Corma and H. Garcia, "Zeolite-based photocatalysts," *Chemical Communications*, vol. 10, no. 13, pp. 1443–1459, 2004.
- [8] C. Guillard, H. Lachheb, A. Houas, M. Ksibi, E. Elaloui, and J. M. Herrmann, "Influence of chemical structure of dyes, of pH and of inorganic salts on their photocatalytic degradation by TiO₂ comparison of the efficiency of powder and supported TiO₂," *Journal of Photochemistry and Photobiology A*, vol. 158, no. 1, pp. 27–36, 2003.
- [9] K. Kogo, H. Yoneyama, and H. Tamura, "Photocatalytic oxidation of cyanide on platinumized TiO₂," *Journal of Physical Chemistry*, vol. 84, no. 13, pp. 1705–1710, 1980.
- [10] J. Zhao and X. Yang, "Photocatalytic oxidation for indoor air purification: a literature review," *Building and Environment*, vol. 38, no. 5, pp. 645–654, 2003.
- [11] F. Zang, J. Zhao, T. Shen et al., "TiO₂-assisted photodegradation of dye pollutants. II. Adsorption and degradation kinetics of eosin in TiO₂ dispersions under visible light irradiation," *Applied Catalysis B*, vol. 5, pp. 147–156, 1998.
- [12] G. Rothenberger, J. Moser, M. Grätzel, N. Serpone, and D. K. Sharma, "Charge carrier trapping and recombination dynamics in small semiconductor particles," *Journal of the American Chemical Society*, vol. 107, no. 26, pp. 8054–8059, 1985.
- [13] H. Tributsch, N. Serpone, and E. Pelizzetti, *Photocatalysis: Fundamentals and Applications*, Wiley, New York, NY, USA, 1989.
- [14] M. C. Daniel and D. Astruc, "Gold nanoparticles: assembly, supramolecular chemistry, quantum-size-related properties, and applications toward biology, catalysis, and nanotechnology," *Chemical Reviews*, vol. 104, no. 1, pp. 293–346, 2004.
- [15] C. F. Bohren and D. R. Huffman, *Absorption and Scattering of Light by Small Particles*, Wiley, New York, NY, USA, 1983.
- [16] J. L. Lyon, D. A. Fleming, M. B. Stone, P. Schiffer, and M. E. Williams, "Synthesis of Fe oxide core/Au shell nanoparticles by iterative hydroxylamine seeding," *Nano Letters*, vol. 4, no. 4, pp. 719–723, 2004.
- [17] S. J. Cho, J. C. Idrobo, J. Olamit, K. Liu, N. D. Browning, and S. M. Kauzlarich, "Growth mechanisms and oxidation resistance of gold-coated iron nanoparticles," *Chemistry of Materials*, vol. 17, no. 12, pp. 3181–3186, 2005.
- [18] D. Caruntu, B. L. Cushing, G. Caruntu, and C. J. O'Connor, "Attachment of gold nanograins onto colloidal magnetite nanocrystals," *Chemistry of Materials*, vol. 17, no. 13, pp. 3398–3402, 2005.
- [19] Y. H. Chen and U. Nickel, "Superadditive catalysis of homogeneous redox reactions with mixed silver-gold colloids," *Journal of the Chemical Society, Faraday Transactions*, vol. 89, no. 14, pp. 2479–2485, 1993.
- [20] N. Aihara, K. Torigoe, and K. Esumi, "Preparation and characterization of gold and silver nanoparticles in layered laponite suspensions," *Langmuir*, vol. 14, no. 17, pp. 4945–4949, 1998.
- [21] M. Michaelis, A. Henglein, and P. Mulvaney, "Composite Pd-Ag particles in aqueous solution," *Journal of Physical Chemistry*, vol. 98, no. 24, pp. 6212–6215, 1994.
- [22] M. Muneer, M. Qamar, and D. Bahnemann, "Heterogeneous photocatalysed reaction of two selected pesticide derivatives trichlopyr and daminozid in aqueous suspension of titanium dioxide," *Journal of Environmental Management*, vol. 80, pp. 99–106, 2006.
- [23] C. Karunakaran and S. Senthilvelan, "Photocatalysis with ZrO₂: oxidation of aniline," *Journal of Molecular Catalysis A: Chemical*, vol. 233, no. 1–2, pp. 1–8, 2005.
- [24] M. Styliadi, D. I. Kondarides, and X. E. Verykios, "Visible light-induced photocatalytic degradation of acid orange 7 in aqueous TiO₂ suspensions," *Applied Catalysis B*, vol. 47, no. 3, pp. 189–201, 2004.
- [25] K. Wilke and H. D. Breuer, "The influence of transition metal doping on the physical and photocatalytic properties of titania," *Journal of Photochemistry and Photobiology A*, vol. 121, no. 1, pp. 49–53, 1999.
- [26] J. Araña, J. L. Martínez Nieto, J. A. H. Melián et al., "Photocatalytic degradation of formaldehyde containing wastewater from veterinarian laboratories," *Chemosphere*, vol. 55, no. 6, pp. 893–904, 2004.

- [27] A. J. Maira, K. L. Yeung, J. Soria et al., "Gas-phase photo-oxidation of toluene using nanometer-size TiO_2 catalysts," *Applied Catalysis B*, vol. 29, no. 4, pp. 327–336, 2001.
- [28] J. Krýsa, M. Keppert, J. Jirkovský, V. Štengl, and J. Šubrt, "The effect of thermal treatment on the properties of TiO_2 photocatalyst," *Materials Chemistry and Physics*, vol. 86, no. 2-3, pp. 333–339, 2004.
- [29] M. Saquib and M. Muneer, " TiO_2 -mediated photocatalytic degradation of a triphenylmethane dye (gentian violet), in aqueous suspensions," *Dyes and Pigments*, vol. 56, no. 1, pp. 37–49, 2003.
- [30] G. Palmisano, M. Addamo, V. Augugliaro et al., "Selectivity of hydroxyl radical in the partial oxidation of aromatic compounds in heterogeneous photocatalysis," *Catalysis Today*, vol. 122, no. 1-2, pp. 118–127, 2007.
- [31] D. A. Friesen, L. Morello, J. V. Headley, and C. H. Langford, "Factors influencing relative efficiency in photo-oxidations of organic molecules by Cs3PWO and TiO_2 colloidal photocatalysts," *Journal of Photochemistry and Photobiology A*, vol. 133, no. 3, pp. 213–220, 2000.
- [32] N. Serpone, "Relative photonic efficiencies and quantum yields in heterogeneous photocatalysis," *Journal of Photochemistry and Photobiology A*, vol. 104, no. 1-3, pp. 1–12, 1997.
- [33] U. I. Gaya and A. H. Abdullah, "Heterogeneous photocatalytic degradation of organic contaminants over titanium dioxide: a review of fundamentals, progress and problems," *Journal of Photochemistry and Photobiology C: Photochemistry Reviews*, vol. 9, no. 1, pp. 1–12, 2008.
- [34] D. S. Bhatkhande, S. P. Kamble, S. B. Sawant, and V. G. Pangarkar, "Photocatalytic and photochemical degradation of nitrobenzene using artificial ultraviolet light," *Chemical Engineering Journal*, vol. 102, no. 3, pp. 283–290, 2004.
- [35] M. Hügül, E. Erçağ, and R. Apak, "Kinetic studies on UV-photodegradation of some chlorophenols using TiO_2 catalyst," *Journal of Environmental Science and Health A*, vol. 37, no. 3, pp. 365–383, 2002.
- [36] G. Palmisano, M. Addamo, V. Augugliaro et al., "Selectivity of hydroxyl radical in the partial oxidation of aromatic compounds in heterogeneous photocatalysis," *Catalysis Today*, vol. 122, no. 1-2, pp. 118–127, 2007.
- [37] D. A. Friesen, L. Morello, J. V. Headley, and C. H. Langford, "Factors influencing relative efficiency in photo-oxidations of organic molecules by Cs3PWO and TiO_2 colloidal photocatalysts," *Journal of Photochemistry and Photobiology A*, vol. 133, no. 3, pp. 213–220, 2000.
- [38] P. V. Kamat, R. Huehn, and R. Nicolaescu, "A "sense and shoot" approach for photocatalytic degradation of organic contaminants in water," *Journal of Physical Chemistry B*, vol. 96, no. 4, pp. 788–794, 2007.